

Diese Dissertation haben begutachtet:

.....



DISSERTATION

Silicon sensor prototypes and module concepts for the CMS tracker for the High Luminosity Large Hadron Collider

ausgeführt zum Zwecke der Erlangung des akademischen Grades eines
Doktors der technischen Wissenschaften unter der Leitung von

Univ.Doz. Dipl.-Ing. Dr.techn. Manfred Krammer

Institut für Hochenergiephysik

der Österreichischen Akademie der Wissenschaften

und

Atominstitut der Österreichischen Universitäten

eingereicht an der Technischen Universität Wien

Fakultät für Physik

von

Johannes Großmann

Matrikelnummer: 1429258

Baumgartenstr 17/10, 1140 Wien

Wien, am 30. April 2018

Kurzfassung

Der Large Hadron Collider wird im Zuge des HL-LHC Projekts die Luminosität des Beschleunigers stark erhöhen. Das CMS Experiment, als eines der vier großen Experimente am LHC, muss deshalb Upgrades vornehmen, um in der High-Luminosity Ära in der Lage zu sein Daten zu nehmen. Fast alle Subsysteme des Detektors müssen an die anspruchsvollen Konditionen in dieser Phase angepasst werden.

Diese Arbeit steht im Kontext der vorgesehenen Upgrades für den CMS-Spurdetektor. Insbesondere muss ein komplett neuer Detektor entwickelt werden, da der jetzige Detektor auf Grund von Strahlenschädigung nicht mehr effizient funktionieren würde, und da die Anforderungen an den Detektor durch die höhere Luminosität nicht mit der aktuellen Technologie zu erfüllen sind. Mit einer aktiven Fläche von 200 m^2 Silizium Sensoren wird der Detektor in der Lage sein alle 25 ns im Mittel 6000 Spuren von geladenen Teilchen mit Energien über 300 MeV bei 200 harten Teilchenkollisionen zu detektieren. Außerdem muss der Spurdetektor in Echtzeit Information über den transversalen Impuls der Teilchen an das L1-Trigger System liefern und gleichzeitig bei erhöhter Triggerrate von 750 kHz funktionieren. Um diese Fähigkeiten zu gewährleisten, wurden deshalb zwei spezielle Module entwickelt, welche Datenreduktion und p_T - Diskriminierung vereinen. Eines dieser p_T Module ist das PS-Modul. Diese Arbeit beinhaltet die Charakterisierung und Qualifizierung der Prototypen der Makro-Pixel Sensoren für das PS-Modul, so wie der ersten Prototypenmodule. Im Zuge dessen wird die Funktion des intelligenten Auslesechips überprüft. Außerdem wird ein neues invertiertes Modulkonzept untersucht, welches bestimmte Nachteile von aktuellen hybriden Pixel Detektoren kompensiert und eine Alternative zum Standarddesign darstellt. Die Arbeit beinhaltet elektrische Messungen an den Sensoren, Messungen der Detektorantwort mit einem gepulstem Infrarot-Laser sowie mit einem 5.6 GeV Elektronenstrahl. Auf Grund der Analyse der gewonnenen Resultate wird eine Empfehlung für ein zukünftiges Sensordesign gegeben und die Perspektiven des invertierten Konzepts abgeschätzt.

Abstract

The Large Hadron Collider will highly increase the luminosity of the accelerator in the course of the HL-LHC project. The CMS experiment, as one of the four major experiments at the LHC, must consequently receive an upgrade, to be able to record data in the high-luminosity era. Almost all subsystems of the detector must be adapted to the demanding conditions in this phase. This work is related to the planned upgrades for the CMS tracker detector. In particular, a completely new detector must be developed, since the current detector would no longer work efficiently, due to radiation damage, and since the requirements for the detector cannot be met with the current technology, due to the higher luminosity. With an active area of 200 m^2 silicon sensors, the detector will be able to detect every 25 ns on average 6000 tracks of charged particles with energies above 300 MeV at 200 hard particle collisions. In addition, the tracker detector must provide real-time information about the transverse momentum of the particles to the L1-trigger system and simultaneously function at an increased trigger rate of 750 kHz. Therefore two dedicated types of modules were developed, which combine data reduction and p_T -discrimination. One of these p_T -modules is the PS module. This work includes the characterization and qualification of the prototypes of macro-pixel sensors for the PS module, as well as the first prototype modules. In the course of this thesis, the function of the intelligent readout chip is validated. In addition, a new inverted module concept is investigated, which compensates for certain disadvantages of current hybrid-pixel detectors and represents an alternative to the standard module design. The work includes electrical measurements on the sensors, measurements of the detector response with a pulsed infrared laser, as well as with a 5.6 GeV electron beam. Based on the analysis of the results obtained, a recommendation for a future sensor design is given and the perspectives of the inverted concept are explored.

Contents

| | | |
|----------|--|-----------|
| 1 | Introduction | 1 |
| 2 | The CMS experiment and the Large Hadron Collider | 3 |
| 2.1 | The Compact Muon Solenoid | 3 |
| 2.2 | The High-Luminosity LHC | 6 |
| 2.3 | Physics motivation and goals for CMS in the HL-LHC era | 9 |
| 2.4 | Higgs production and decay channels | 10 |
| 2.5 | Requirements for tracking in HL-LHC era | 13 |
| 3 | Interactions of particles with matter | 15 |
| 3.1 | Energy loss of charged particles | 15 |
| 3.2 | Bremsstrahlung energy loss and radiation length | 19 |
| 3.3 | Interactions of photons | 20 |
| 3.4 | Low energy photon absorption in semiconductors | 21 |
| 3.5 | Laser light and beam quality measures | 23 |
| 3.6 | Gaussian beams | 24 |
| 4 | Semiconductor physics | 29 |
| 4.1 | Intrinsic silicon | 29 |

| | | |
|----------|---|-----------|
| 4.2 | Charge carrier transport in semiconductors | 33 |
| 4.3 | Continuity equation | 35 |
| 4.4 | The p-n junction | 36 |
| 4.4.1 | Capacitance of a p-n junction | 38 |
| 4.4.2 | Characteristics of segmented diodes | 38 |
| 4.4.3 | Junction Breakdown | 38 |
| 5 | Silicon sensors | 41 |
| 5.1 | Sensor material | 41 |
| 5.2 | Cell geometry | 42 |
| 5.3 | Sensor periphery and sensor protection | 44 |
| 5.4 | Biasing circuit via Punch-Through Protection | 46 |
| 5.5 | Design parameters PTP | 46 |
| 6 | CMS Tracker Detector phase II upgrade | 51 |
| 6.1 | Module Design | 53 |
| 6.1.1 | The PS Module | 54 |
| 6.1.2 | The Macro-Pixel-Sub-Assembly Block | 55 |
| 6.2 | Readout Electronics | 59 |
| 6.2.1 | Noise in silicon detectors | 59 |
| 6.2.2 | Multichannel readout and threshold dispersion | 61 |
| 6.2.3 | MPA and SSA | 62 |
| 6.3 | Prototypes | 65 |
| 7 | Characterization of PS-p-light sensor prototypes | 69 |

| | | |
|-----------|--|------------|
| 7.1 | Static global characterization | 70 |
| 7.1.1 | Results of p-spray and p-stop strip isolation techniques | 74 |
| 7.1.2 | Edge implant geometry studies | 76 |
| 7.2 | Measurement of effective energy | 78 |
| 7.3 | Measurements on test structures | 81 |
| 7.4 | Characterization of the PTP-structure | 83 |
| 7.5 | TCAD Simulation of the PTP-structure and macro-pixel cell . | 84 |
| 7.6 | Homogeneity of strip parameters | 93 |
| 7.6.1 | Optical inspection | 98 |
| 7.6.2 | Interpixel measurements | 98 |
| 7.7 | Summary | 102 |
| 8 | Module pretest, calibration and analog performance | 104 |
| 9 | Measurement of detector response with IR-laser system | 108 |
| 9.1 | Laser system specifications and setup | 108 |
| 9.2 | Tests with constant laser repetition rate | 110 |
| 9.3 | Tests with synchronized laser pulses | 116 |
| 9.4 | Summary | 121 |
| 10 | Test Beams at the DESY-II Synchrotron | 122 |
| 10.1 | Test Beam Setup, Trigger and DAQ | 123 |
| 10.2 | Offline data analysis | 128 |
| 10.2.1 | Clustering and hit generation | 129 |
| 10.2.2 | Pattern recognition and tracking | 134 |

| | |
|--|------------|
| 10.2.3 Alignment | 136 |
| 10.2.4 Iterative pull analysis | 138 |
| 10.2.5 Measurement of DUT efficiency and noise occupancy | 138 |
| 10.3 Results and conclusion | 139 |
| 11 Summary and conclusion | 146 |
| A Acknowledgements | 149 |
| List of Tables | 150 |
| List of Figures | 153 |
| Acronyms | 177 |

Chapter 1

Introduction

In the past century modern particle physics has developed a very precise description of nature – the so called standard model of particle physics. These achievements were made with the help of particle accelerators and high precision particle detectors. The measurement of collisions of high energetic particles in a collider experiment allows the discovery of new elementary particles and probes the theory of the fundamental forces of nature. It is known that the **standard model (SM)** has several shortcomings concerning the problem of strong CP-violation in the QCD-sector, unification of fundamental forces, mass hierarchy of fermions, hierarchy of **Cabibbo-Kobayashi-Maskawa Matrix (CKM-Matrix)**, matter antimatter asymmetry, nature of dark matter and gravitation. Theorists have developed extensions to the **SM**, which could solve problems like the hierarchy problem, the baryon asymmetry problem, dark matter and inflation. Up to now experiments at particle accelerators are consistent with the **SM** and the most recently discovered particle predicted by the standard model, namely the Higgs Boson, was discovered by **ATLAS** and **CMS** in 2012. However the uncertainties about the true nature of the Higgs Boson remain and further studies could discover properties, which are not predicted by the **SM**. This motivates precision studies of the Higgs Boson and the accelerator to produce Higgs bosons in abundance will be the **High-Luminosity LHC (HL-LHC)**.

In order to cope with the harsh conditions in the **HL-LHC** era, the **CMS** experiment will undergo upgrades for a variety of the subsystems. This thesis is dedicated to the outer silicon-strip tracker and the technological challenges for the upgrade. The thesis covers in detail the foreseen technology of the sensors for one type of the silicon-detector modules and two different types of module concepts, which were considered to cover the inner region of the outer tracker.

This work is divided in four parts. The first part is a general introduction about **HL-LHC**, the current status of the **Compact Muon Solenoid (CMS)** experiment, followed by a chapter about theory of silicon sensor technology and the necessary measures for the **CMS** tracker detector for the upgrade. The second part comprises electrical characterization of prototype sensors and **Technology Computer Aided Design (TCAD)** simulations of dedicated structures. In the third part measurements on prototype modules with a focused, pulsed laser system are presented and the analog performance of the binary readout electronic is characterized. In the fourth part the performance of a new type of detector module in a lepton beam is shown.

Chapter 2

The CMS experiment and the Large Hadron Collider

2.1 The Compact Muon Solenoid

The CMS experiment [1] is one of the four detectors at **Large Hadron Collider (LHC)** and is designed as a 4π apparatus¹. The experiment is built of different subdetectors in a nested cylindrical arrangement with endcaps. A slice of the apparatus from the interaction point to the outer perimeter is shown in figure 2.1. Each of the subdetectors has specific tasks, which are introduced in the following. A 4T superconducting solenoid provides sufficient bending power for the measurement of the momentum of muons. Numbers for the expected detector performance of the subdetectors presented in this section are taken from [1].

The design of the detector has to ensure [1, chap. 1]

- Excellent muon identification and momentum resolution, good dimuon mass resolution and charge measurement for muons with $p < 1$ TeV;
- High reconstruction efficiency and momentum resolution for charged particles in the inner tracker.

¹This section describes the current pre-**HL-LHC** status of the experiment.

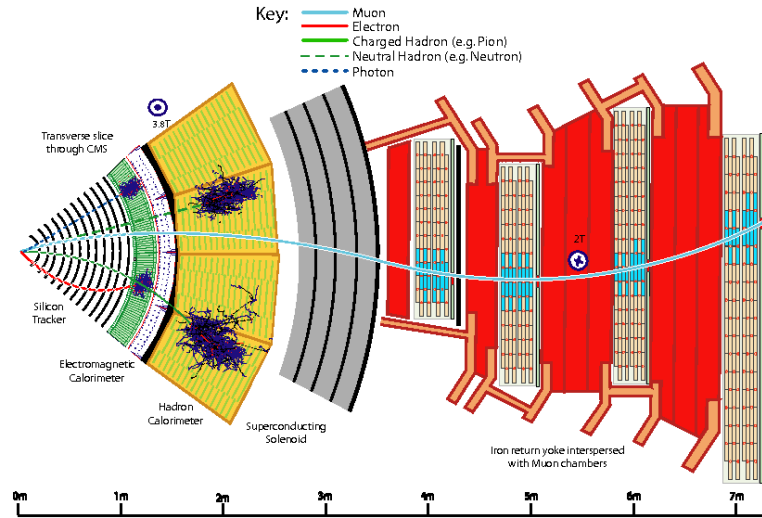


Figure 2.1: A slice of the **CMS** experiment from the interaction point to the outer perimeter taken from [2].

- Excellent energy resolution in the electromagnetic calorimeter, good diphoton and dielectron mass resolution, photon and lepton isolation at high luminosity.
- Good dijet and missing-transverse-energy resolution, achieved with large hermetic coverage by the highly segmented hadronic calorimeters.

The inner part of the **CMS** is the tracking system with an active area of 200 m^2 . The main task of the system is to record the trajectories of charged particles, which allows measurement of the momentum and particle identification via the mean energy loss dE/dx for the particles d, p, K, π, μ^- and e . Another important aspect of the tracking system is the precise reconstruction of the primary vertices, with the help of the inner tracker pixel detector. For the tracking system the ambiguities in the track reconstruction are kept at acceptable level with a highly granular detector. This also allows to attribute the tracks to the correct bunch crossing. However, high granularity comes with a high number of electronic readout channels, which in turn requires efficient cooling, resulting in additional mass. This is a conflicting aim, because a higher amount of mass deteriorates the measurement

precision, due to **Multiple Coulomb Scattering (MCS)**. For the current tracker the cooling system must be able to dissipate 150 kW in a total cylindrical volume of 5.8 m length and 2.5 m diameter.

For a tracking detector always a trade-off between cooling, minimization of material budget and number of readout channels is chosen, which depends on the currently available technologies and cost.

The inner tracking volume comprises a pixel detector, which was completely exchanged during the phase-1 upgrade in the extended end of the year stop 2016/2017 (see figure 2.3) [3]. The phase-1 pixel detector has 1184 modules in the barrel region and 672 modules in the disk region, resulting in a total pixel count of 124×10^6 . The pixel modules cover in four layers the radius up to 16 cm in the barrel volume. Three disk endcaps at 29.1 cm, 39.6 cm and 51.6 cm from the interaction point along the beam line complete the pixel subsystem. The pixel cell size of $100 \mu\text{m} \times 150 \mu\text{m}$ of the phase-1 detector is the same as in the previous pixel detector. The phase-1 upgrade mainly addressed the limitations due to expected data loss of the previous readout chips and detector degradation due to radiation damage.

In the current silicon strip tracker (**Outer Tracker (OT)**) in total 15 148 strip detector modules with silicon micro-strip detectors are used. The strip detector has ten layers in the barrel region and extends to a radius of 1.1 m. In the endcaps 3 + 9 disks extend the sensitive volume to a pseudorapidity of $|\eta| = 2.5$ in the strip region. High granularity results in a cell size of $10 \text{ cm} \times 80 \mu\text{m}$ at intermediate radii. With increasing distance to the interaction point the cell size increases to $25 \text{ cm} \times 180 \mu\text{m}$. Special modules with two micro-strip detectors in back-to-back configuration with the strip directions in a stereo angle of 100 mrad provide a measurement in the second coordinate and achieve single-point resolution of $230 \mu\text{m}$ and $530 \mu\text{m}$ depending on the tracker region. Sensors of thickness $350 \mu\text{m}$ and $500 \mu\text{m}$ are used.

Further details of the future requirements of the tracking system for **HL-LHC** are presented in section 2.5.

Lead-tungstate crystals with **Avalanche Photo Diode (APD)** and **Vacuum Photo Triodes (VPT)** readout are used in the **Electromagnetic**

Calorimeter (ECAL), which allows to determine the energy of electromagnetic showers, produced by incoming e . The **ECAL** thickness is larger than $25 X_0$ and has a preshower system for the π^0 rejection.

A brass scintillator sampling **Hadronic Calorimeter (HCAL)** with 7 to 11 λ_I interaction length surrounds the **ECAL**. Wavelength shifting fibers and clear fibers guide the scintillation light to the hybrid photo-diode detectors. Additionally calorimetry is complemented by a tail-catcher, iron/quartz-fiber calorimeters, CASTOR and ZDC.

In 2017 a mean of 50 simultaneous collisions occur at a bunch-crossing frequency of 25 ns. It is impossible to store every single collision event and therefore **CMS** uses a sophisticated two stage trigger system to keep the data rate at the achievable target level and to select the events containing possibly new physics [1, chap. 8],[4]. The **Level-1 Trigger (L1)** is realized in highly programmable electronics as a real-time filter, using coarsely segmented data from the calorimeters and the muon system and acts as a first-stage preselection system. Currently the maximum **L1** rate is limited to 100 kHz. The detector front-end electronics is capable of storing the raw data in pipelined memories until the **L1** decision is taken, which takes up to 3.2 μ s. The **High-Level Trigger (HLT)** is a software filter realized in a filter farm of $\mathcal{O}(1 \times 10^5)$ processors further reducing the rate of accepted events to $\mathcal{O}(100 \text{ Hz})$, which is limited by the data recording technology. The **HLT** selection ensures to fulfill the physics program, by including all data containing possible new physics. The applied selection thresholds should be robust and not depending on knowledge of the detector calibration constants or other changing run conditions. Data samples include events to be able to obtain trigger efficiencies and reconstruction efficiencies offline.

2.2 The High-Luminosity LHC

Currently the most powerful accelerator is the **LHC** at **CERN** (see figure 2.2). The LHC has a circumference of 26.7 km and uses 3.8 T superconducting dipole magnets to keep the particle beams on a circular path. Key

performance measures of a high energy physics collision experiment at a particle accelerator are the energy of the colliding particle in the center-of-mass frame \sqrt{s} and the luminosity. The instantaneous luminosity is given by

$$L = \gamma \frac{n_b N^2 f_{\text{rev}}}{4\pi \beta^* \epsilon_n} R, \text{ where} \quad (2.1)$$

$$R = 1/\sqrt{1 + \frac{\theta_c \sigma_z}{2\sigma}}, \quad (2.2)$$

with symbols and constants from table 2.1 [5, chap. 1.2.1].

Table 2.1: Symbols and constants for the instantaneous luminosity with numbers for the **HL-LHC** from equation (2.1)

| Symbol | Definition | Nominal Value |
|------------------|---|------------------------------|
| γ | Proton beam energy | $\gamma = \frac{E}{m_0} c^2$ |
| n_b | Number of bunches per beam | 2808 |
| N | Bunch population | 1.15×10^{11} |
| f_{rev} | Bunch revolution frequency | 11.2 kHz |
| β^* | Beam beta function | 0.55 m |
| ϵ_n | Transverse normalized emittance | 3.75 μm |
| R | Luminosity geometrical reduction factor | 0.85 to 0.55 |
| θ_c | Full crossing angle between beams | 285 μrad |
| σ | Transverse beam size (r.m.s) | 16.7 μm |
| σ_z | Longitudinal beam size (r.m.s) | 7.55 cm |

The **LHC** will receive a major upgrade during **LS3** (see 2.3), which is called the **HL-LHC**[5]. The current specifications for the operating conditions of **HL-LHC** are

- a peak instantaneous luminosity of $L_{\text{peak}} = 5 \times 10^{34} \text{ cm}^{-2}\text{s}^{-1}$ and
- an integrated luminosity of 250 fb^{-1} per year [5, 7].

in the so-called ultimate parameter concept $L_{\text{peak}} = 7 \times 10^{34} \text{ cm}^{-2}\text{s}^{-1}$ to $L_{\text{peak}} = 7.5 \times 10^{34} \text{ cm}^{-2}\text{s}^{-1}$, a pile up of 200 hard collisions every 25 ns and a integrated luminosity of 300 fb^{-1} to 350 fb^{-1} per year could be reached. The collider is capable to produce pp, PbPb and pPb collisions. During **HL-LHC** new techniques such as luminosity levelling and longitudinal bunch

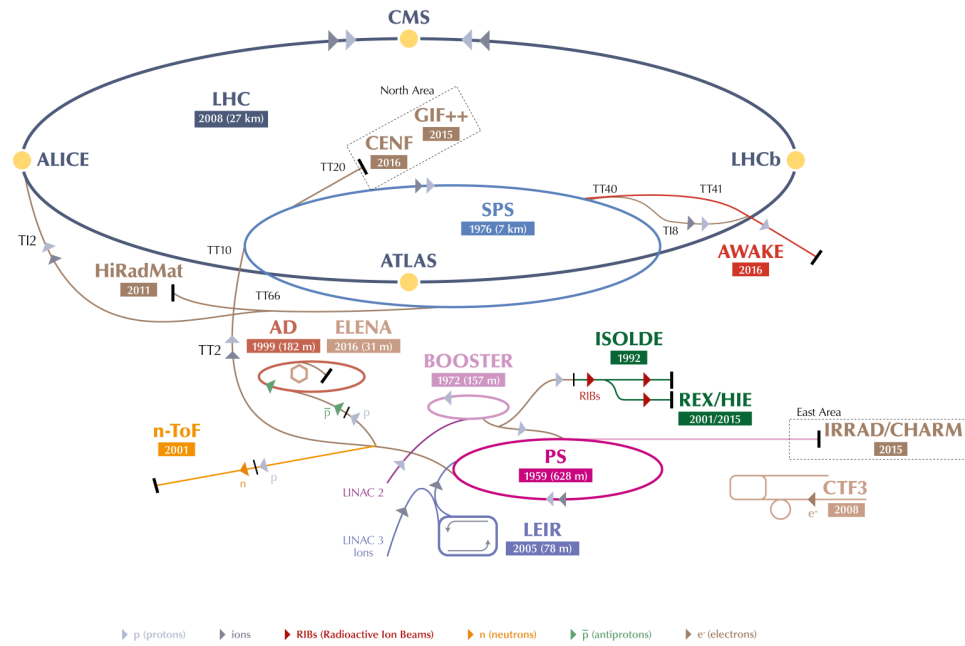


Figure 2.2: The **LHC** accelerator complex from [6] with the major four experiments **CMS**, **A Toroidal LHC ApparatuS (ATLAS)**, **ALICE** and **LHCb** and the preaccelerators.

rotation via crab-cavities will be implemented [5, chap. 1.2.4]. A part from the increase in luminosity, the new collider also will improve the availability for better physics efficiency.

In the **HL-LHC** era the luminosity will increase to unprecedented values for a hadron collider with this energy. With this machine a large number of measurements will improve their uncertainties and new physics could be discovered in measurements, which profit from high statistics.

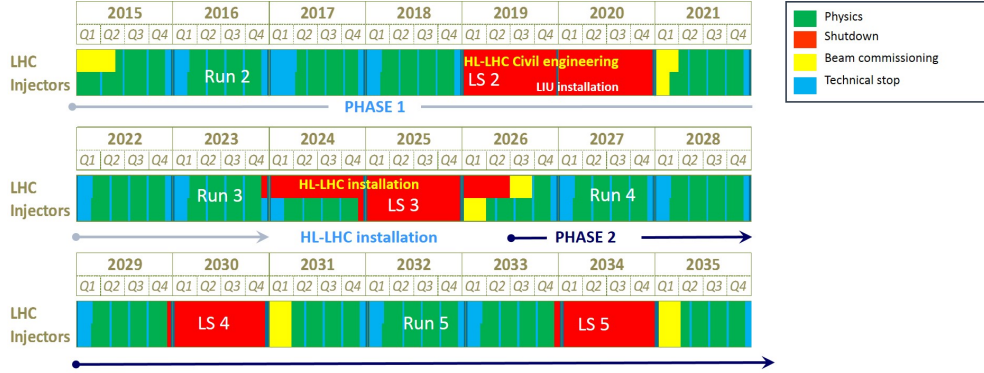


Figure 2.3: The schedule for the upgrade of **LHC** to **HL-LHC** from [7, chap. 1]. Data taking periods are indicated in green. The **CMS Tracker** (**CMS Tracker Detector**) will be replaced during **Long Shutdown 3** (**LS3**).

2.3 Physics motivation and goals for CMS in the HL-LHC era

After the discovery of a standard model like Higgs Boson with a mass of 125 GeV at the **ATLAS** and **CMS** experiment, further studies of the nature of the Higgs Boson are motivated. Precision measurements of the **SM** Higgs Boson Yukawa couplings may show, whether the fine-tuning mechanism is realized in nature, and test for high scale **Supersymmetry (SUSY)**. **SUSY** is a beyond **SM** theory, which may provide **Dark Matter (DM)** candidates in the lightest neutralino. The searches for theories beyond the standard model profit from an increased luminosity during **HL-LHC**, because the sensitivity to low production cross-sections is increased.

In the high luminosity era **CMS** will achieve percent level precision for the Higgs couplings and great improvement in the measurement of the coupling to muons with branching ratio of 1×10^{-4} is possible. The measurement of Higgs boson self coupling and Higgs boson pair production, which have 1000 times smaller production cross section, than for single Higgs production is feasible.

2.4 Higgs production and decay channels

For the minimal standard model there are several important Higgs production channels for a hadron collider, which are discussed in the following beginning with the most dominant processes (see 2.4a, [8]).

- **Gluon-Gluon Fusion ($gg \rightarrow H$):** In this process two gluons from the colliding protons interact. A Higgs particle is produced through the formation of an virtual heavy-quark loop. Top quarks, and to some extent bottom quarks, dominate the virtual particles in the loop, due to their greater mass and consequently better coupling to the Higgs. The gluon-gluon fusion is by far the most important production process (see 2.5a).
- **Vector-Boson-Fusion ($qq \rightarrow qqH$):** Two quarks, or a quark and anti-quark interact via a virtual vector boson, which emits a Higgs. The quarks do not necessarily need to be from the same type (see 2.5b).
- **Associated with a W/Z boson ($qq \rightarrow WH, pp \rightarrow ZH$):** A fermion collides with the corresponding anti-fermion and produces a vector boson W^\pm of sufficient energy, which subsequently emits a Higgs boson. For the **LHC** quark-anti-quarks are the dominant fermions (see 2.5c).
- **Associated with a Z boson ($gg \rightarrow ZH$):** Two gluons interact via an virtual Z boson, which radiates a Higgs boson. In an alternative process a fermion runs in a loop and radiates a Higgs and a Z boson (see 2.5d).
- **Associated with a pair of top quarks ($qq, gg \rightarrow ttH$):** Two gluons interact via an virtual Z boson, which radiates a Higgs boson. In an alternative process a fermion runs in a loop and radiates a Higgs and a Z boson (see 2.5e).

For the Higgs decay different processes are possible, which are introduced beginning with the most important ones for the discovery [11]. The branching ratio of the individual processes is found in figure 2.4b.

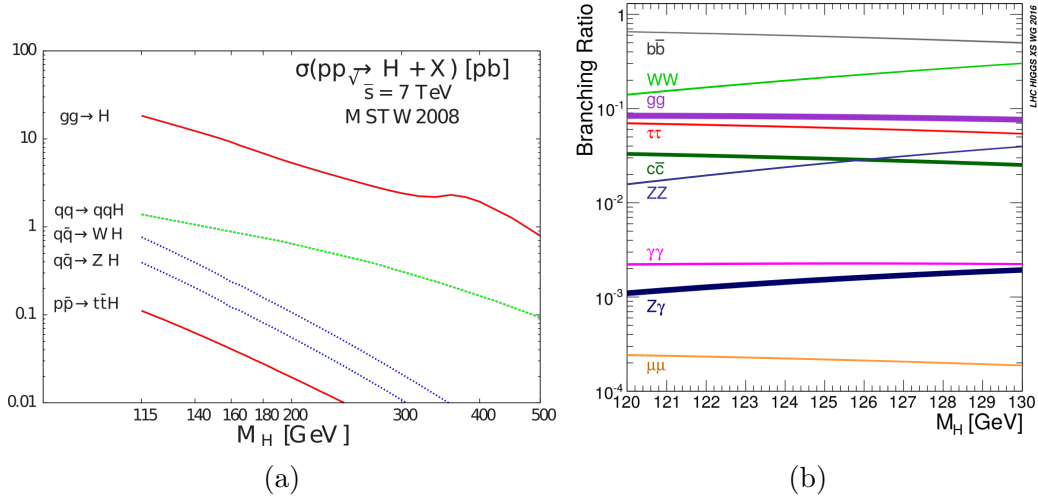


Figure 2.4: (a) The Higgs production cross sections for the different production channels from [9]. For increased centre of mass energy only small changes are expected. (b) The branching ratios of the Higgs decay channels as function of the Higgs mass from [10].

- $H \rightarrow \gamma\gamma$: Although this channel has a very low branching ratio and despite the large combinatorial background, this channel is very sensitive. The Higgs causes a narrow peak in the di-photon invariant mass distribution.
- $H \rightarrow ZZ \rightarrow 4\ell$: In this decay channel a narrow peak in the four lepton invariant mass is observed. Different analysis techniques are used for the sub-channels $4e, 4\mu, 2e\mu$. The main backgrounds originate from $ZZ, Z + b\bar{b}$ and $t\bar{t}$ production. This decay mode and the $H \rightarrow \gamma\gamma$ mode were important for the discovery of the Higgs and have good mass resolution.
- $H \rightarrow WW \rightarrow 2\ell + E_T^{\text{miss}}$: The decay mode is analyzed by selection of events, where both W decay leptonically. These events have two isolated, oppositely charged leptons and large E_T^{miss} , due to the undetected neutrinos in the final state. Only a low mass resolution is obtained in this decay mode.
- $H \rightarrow \tau\tau$: The decay of a Higgs in $\tau^- \tau^+$ leptons splits into four different sub-channels, which originate in the branching of the τ decay,

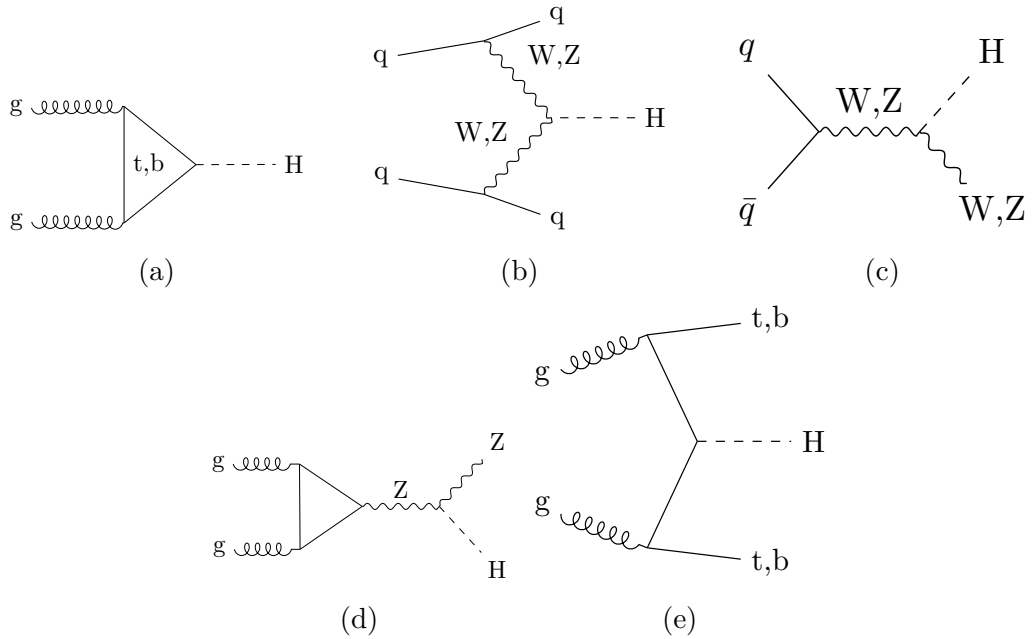


Figure 2.5: (a-e) Different Feynman diagrams for the Higgs production channels.

namely $\tau\tau \rightarrow e\mu$, $\tau\tau \rightarrow \mu\mu$, $\tau\tau \rightarrow e\tau_h$, $\tau\tau \rightarrow \mu\tau_h$, where τ_h refers to leptons reconstructed in their hadronic decays. The neutrinos leave not signature in the detector and therefore in the analysis one challenge is the search for missing transverse energy. This decay is more likely to be observed for Higgs production in association with W or Z and was established by **CMS** with a significance of 4.9 standard deviations in 2017. [12]. The analysis especially profits from an increase in luminosity.

- **H** \rightarrow **b** $\bar{\text{b}}$: Although this process is the most likely one with a probability of more than 50 %, the analysis is difficult due the QCD multi-jet background. The decay products of this channels manifest as hadronic jets in the calorimeter system, which results in a low mass resolution.

2.5 Requirements for tracking in HL-LHC era

The current tracker detector will degrade due to increasing radiation damage². In addition the demanding pileup conditions of 140 hard collisions per bunch crossing during the high-luminosity era would have negative impact on the performance of the current tracker [13]. Radiation damage leads to reduction in the **charge collection efficiency (CCE)** and Lorentz angle, which results in deterioration of spatial resolution and reduced hit efficiency. Due to irradiation the sensor depletion voltage and leakage current increases. Limitation in the cooling system, as well as in the high voltage rating of the current modules, limit the operation of the current double-sided strip modules to a maximum of 1000 fb^{-1} . Therefore a complete replacement of the current system is necessary.

The requirements for the upgraded detector are shortly summarized in the following:

- Radiation tolerance up to 3000 fb^{-1} integrated luminosity. For the **OT** maintenance intervention is strictly limited. In the inner region of the **OT** a total 1 MeV neutron equivalent fluence of $9.6 \times 10^{14} \text{ n}_{\text{eq}}\text{cm}^{-2}$ is expected.
- Increased granularity is necessary to cope with the high pileup conditions.
- Improved two-track separation to reduce the hit merging in the pixel detector, which is important for highly-energetic jets.
- The material budget of the tracker has impact on the performance of the calorimeter and the overall performance of the event reconstruction, e.g. the accuracy of the p_{T} measurement. Therefore the material in the tracking volume should be kept at the minimum.

² This section is a short revision of the requirements for the upgrade as in [7]. All numbers and figures shown in this section are taken from [7]

- Due to the high pileup and high luminosity, the upgraded tracker should contribute to the **L1** decision. The tracking information facilitates the event selection.
- Extended tracking acceptance up to pseudorapidity $\eta = 4$ improves e.g. the $H \rightarrow \tau\tau$ analysis [13, chap. 10.1.3].

Chapter 3

Interactions of particles with matter

The interaction of particles with matter depends on a variety of parameters like charge and spin of the interacting particle, as well as on material parameters. In theory different interaction mechanisms are described for charged particles and for photons. Energy transfer to the material is possible via excitation of bound electrons or ionization.

3.1 Energy loss of charged particles

For fast charged heavy particles the electronic interactions at intermediate energies are well described by the Bethe-Bloch theory [14, pp. 441 sqq.]. It is useful to define the mass stopping power, which describes the mean rate of energy loss of particles in matter,

$$\left\langle -\frac{dE}{dx} \right\rangle = K \frac{Z}{A} \frac{z^2}{\beta^2} \left[\frac{1}{2} \ln \frac{2m_e c^2 \beta^2 \gamma^2 W_{\max}}{I^2} - \beta^2 - \frac{\delta(\beta\gamma)}{2} \right], \quad (3.1)$$

with the symbols and constants from table table 3.1.

At high energies there is a significant contribution from the polarization of the medium, which results in radiative corrections $\delta(\beta\gamma)$. For low energies

Table 3.1: Symbols and constants for the Bethe-Bloch energy loss from [14, p. 441]

| Symbol | Definition | Value/Unit |
|-----------------------|---|--|
| $m_e c^2$ | electron mass in natural units | 0.511 MeV |
| r_e | classical electron radius | 2.82 fm |
| α | fine structure constant | 1/137 |
| N_A | Avogadro number | $6.02 \times 10^{23} \text{ mol}^{-1}$ |
| ρ | density | g cm^{-3} |
| x | mass per unit area | g cm^{-2} |
| E | incident particle energy | MeV |
| K | $4\pi N_A r_e^2 m_e^2 c^2$ | $0.307 \text{ MeV mol}^{-1} \text{ cm}^{-2}$ |
| z | charge of the incident particle | MeV |
| Z | atomic number of absorber | |
| A | atomic mass number of absorber | |
| W | energy transfer to electron in single collision | MeV |
| I | mean excitation energy | eV |
| $\delta(\beta\gamma)$ | density effect correction | |

nuclear losses and on-shell corrections are important, which account for the non negligible atomic binding energy. The minimum of mass stopping power is at $\beta\gamma$ from 3 to 3.5 [14, p. 442]. Relativistic particles in this range of $\beta\gamma$ are defined as **Minimum Ionizing Particle (MIP)**. The charge collected for a **MIP** is therefore a quality parameter of a particle detector. For silicon the minimum is at $\left. \frac{dE}{dx} \right|_{min} = 1.66 \text{ MeV cm}^2 \text{ g}^{-1}$, which is equivalent to $387.7 \text{ eV } \mu\text{m}^{-1}$ [15, p. 37],[16, p. 6]. The mean energy for the creation of an **Electron-Hole Pair (EHP)** in silicon at room temperature is $\delta E = 3.65 \text{ eV}$ [15, p. 45],[17], which corresponds to approximately 106 **EHPs** per μm for a **MIP**.

For electrons the equation (3.1) must be modified, in order to account for different kinematics, spin and the fact that interacting electrons and shell electrons are indistinguishable particles [15, p. 40]. For silicon a 10% smaller value for $\left. \frac{dE}{dx} \right|_{min}$ (see figure 3.1) is found.

In a detector $\left\langle -\frac{dE}{dx} \right\rangle$ is not directly measurable, due to the long tail of the $\frac{dE}{dx}$ distribution, which is mainly caused by knock-on electrons, which

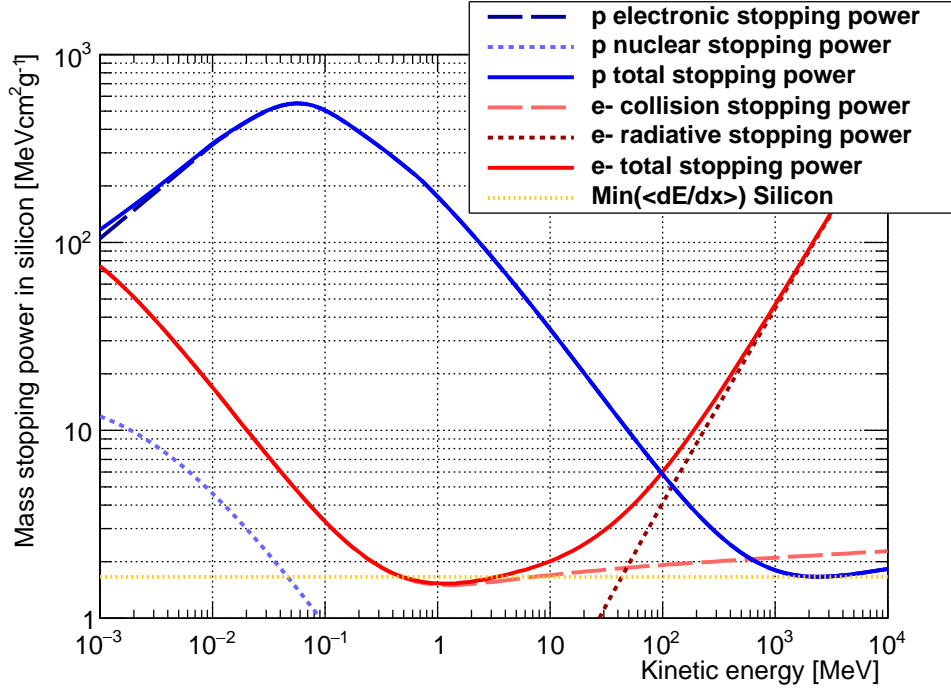


Figure 3.1: The stopping power in silicon for electrons in red with radiative corrections (dotted) and collision contribution (dashed). The stopping power in silicon for protons in blue with nuclear (dotted) and electronic contribution (dashed), with data from [18]. The orange line indicates $\left. \frac{dE}{dx} \right|_{min}$ for a **MIP**. For electrons the minimum is slightly lower than the minimum for other heavy particles.

cause δ -rays. This process is characterized by a high momentum transfer of the incoming particle to a shell electron of an atom. The energy of this electron is sufficient to cause further ionization in the detector material. High angles between incoming particle and δ electron are dominant [15, p. 40]. For tracking these seldom processes deteriorate the resolution, spacially smearing the charge cloud, which is created by the incoming particle. For realistic thin detectors the number of δ -electrons n_δ is $\mathcal{O}(10)$ small.

In the following the Landau-Vavilov theory as presented in [15, pp. 46 sqq.] is introduced. The energy loss ΔE for a path Δx follows a probability density distribution $f(\Delta E; \Delta x)$. δE denotes the infinitesimal contribution to ΔE . In case δE is independent, then the central limit theorem yields a normal distribution for $N \rightarrow \infty$ processes with energy transfer δE . For relativistic

particles this is never the case and therefore an asymmetric distribution is obtained. The characteristics depend mainly on the ratio of the mean energy loss to the maximum energy loss. A measure is given by

$$\kappa = \frac{\xi}{T_{max}}, \quad (3.2)$$

where

$$\xi = \frac{1}{2} K \frac{Z}{A} \rho \frac{z^2}{\beta^2} \Delta x \quad (3.3)$$

and T_{max} is the maximum energy transfer in a single collision. Values of $\kappa \geq 1$ result in a Gaussian distribution, and for small κ an asymmetric distribution is found. Further simplifications yield an expression for the probability density function:

$$f_L(\lambda) = \frac{1}{\pi} \int_0^\infty e^{-t \ln t - \lambda t} \sin \pi t \quad (3.4)$$

The **Probability Density Function (PDF)** from equation (3.4) is characterized by the maximum at the **Most Probable Value (MPV)** $\lambda \approx -0.223$. λ is defined as

$$\lambda = \lambda(\Delta E_w, \xi) = \frac{\Delta E - \Delta E_w}{\xi} - 0.223, \quad (3.5)$$

where E_w denotes the **MPV**. Landau theory is a good approximation for $\kappa \leq 0.01$, otherwise a generalization of the maximum energy transferred was found by Vavilov. However there are situations where a more elaborate theory by Bichsel [19] is more accurate.

δ -electrons may leave the active detector material, which motivates the definition of a restricted energy loss $\frac{dE}{dx}$, which is characterized by a cutoff value for the maximum energy transferred to the electron. A comparison of the restricted $\left\langle \frac{dE}{dx} \right\rangle$ to the **MPV** of the Landau theory and the mean energy loss is found in figure 3.2.

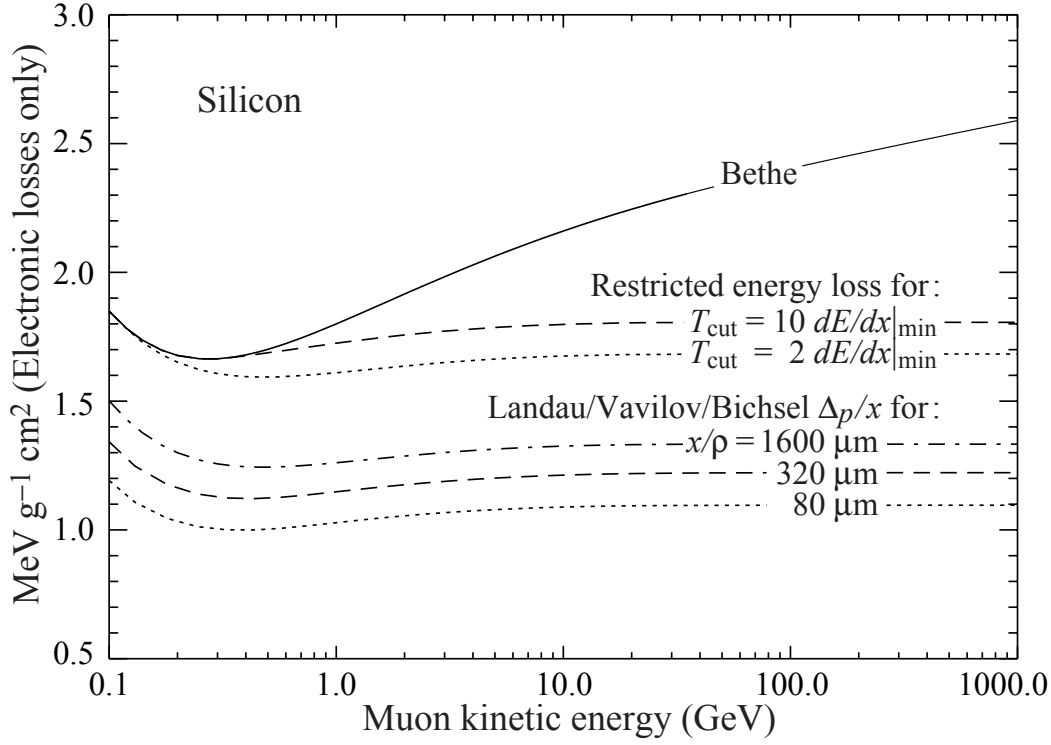


Figure 3.2: Comparison of Bethe theory, with restricted energy loss and Landau MPV of different thickness for muons in silicon from [14, p. 445].

3.2 Bremsstrahlung energy loss and radiation length

Incoming particles may radiate Bremsstrahlung, when they interact with the Coulomb field of the nucleus. Due to the mass of the nucleus the change in the direction of the particle is not negligible. The radiated energy (see figure 3.1) is proportional to

$$\frac{E}{m^2}, \quad (3.6)$$

where E is the relativistic energy of the incoming particle and m is the mass of the incoming particle at rest [15, p. 64]. A more accurate calculation of Bremsstrahlung energy loss yields:

$$\left. \frac{dE}{dx} \right|_{rad} = \frac{E}{X_0}, \quad (3.7)$$

where

$$X_0 \approx \frac{716.408 \text{ g cm}^{-2} A}{Z(Z+1) \ln \frac{287}{\sqrt{Z}}}. \quad (3.8)$$

This formula is a data driven approximation and a more detailed calculation is found in [15, p. 65]. For the energy of an electron in the high energy regime it holds $E(x) = E_0 e^{\frac{x}{X_0}}$. The material budget of a tracker detector is given in units of X_0 and has influence on the spatial resolution and multiple scattering of particles. For mixtures and compounds the radiation length is given by

$$\frac{1}{\rho X_0} = \sum_i \frac{g_i}{\rho X_{0i}} \quad \text{with} \quad g_i = \frac{\rho_i}{\rho}. \quad (3.9)$$

A theory exists, which connects the radiation length to the variance of the scattering angles expected due to deflection of the incoming particle due to **MCS** (see section 10.2.2).

3.3 Interactions of photons

For photons, there are mainly four contributions to the interaction cross section. The fundamental difference to interactions of heavy particles is, that photons are either absorbed via the photoelectric effect or pair-production or scattered by a large angle via a Compton process. Therefore the intensity of a photon beam in matter follows a Beer-Lambert law,

$$I = I_0 e^{-\mu x}, \quad (3.10)$$

where the mass attenuation coefficient μ , which is shown in figure 3.3, is defined as

$$\mu = \frac{N_A}{A} \sum_i \sigma_i, \quad (3.11)$$

where N_A is the Avogadro number, σ_i is the atomic cross section for process i and A is the atomic weight. For low energies the photoelectric effect is dominant, where the incoming photon is absorbed mainly by K-shell electrons. For energies $\mathcal{O}(1 \text{ MeV})$ the Compton effect has the largest cross section. In this

process the incoming photons scatter off a quasi-free electron. If the threshold energy for pair production $E_\gamma > 1.022 \text{ MeV}$ is exceeded, high energy photons can interact in the vicinity of a nucleus and produce an electron positron pair.

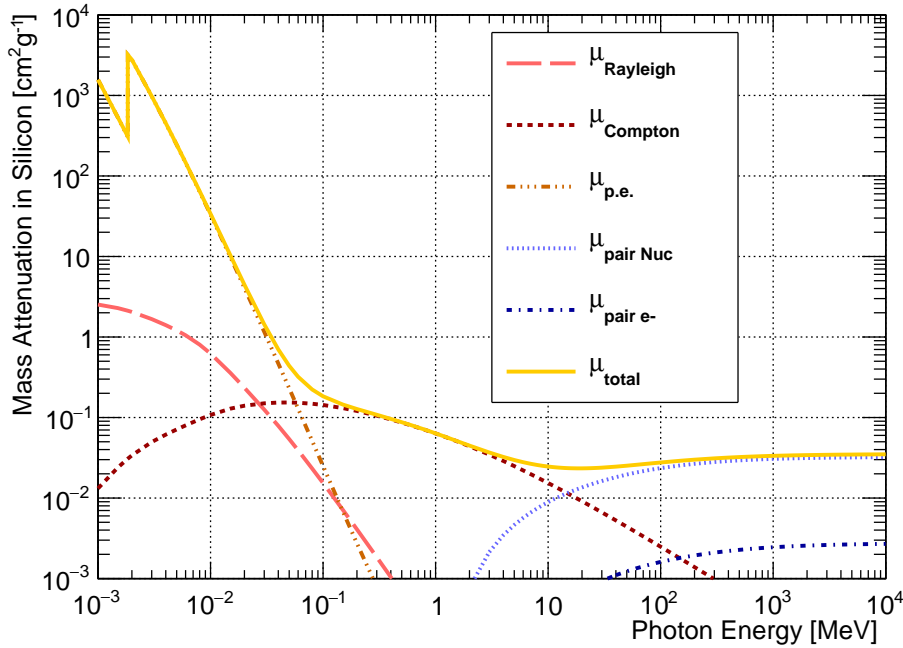


Figure 3.3: The mass attenuation coefficient in silicon with contributions from photoelectric effect (p.e.), Rayleigh scattering, Compton scattering, nuclear and electronic pair production. Data taken from [20].

3.4 Low energy photon absorption in semiconductors

For photon energies near the bandgap energy of a semiconductor, the absorption coefficient depends on the bandgap energy of the semiconductor. The following is a short revision of semiconductor optics processes as described in more detail in [21, pp. 660-672]. Different absorption and recombination processes are known:

- **Band-to-Band Transitions.** The absorption of a photon results in transition of an electron to the conduction band. The inverse process, with photon emission is called radiative recombination. This process is different for direct and indirect semiconductors. For indirect semiconductors such as silicon, radiative recombination or absorption may be assisted by absorption or emission of a phonon, which ensures momentum conservation. Therefore also the absorption coefficient depends on temperature, which is related to the number of available phonons.
- **Impurity-to-Band Transitions.** Absorption of a photon causes transition of electrons from valence band to an acceptor-level, where it becomes trapped. In this process a hole is created. The trapped electron-hole pair has a decay time. Radiative and non radiative recombination is possible. Traps in defect states may assist transitions. The non radiative decay process is also called **Shockley-Read-Hall (SRH)** recombination/generation. For indirect semiconductors the band-to-band transition is suppressed, due to momentum conservation a phonon assists the transition. In this case the second order **SRH** process is dominant.
- **Free-Carrier (Intraband) Transitions.** The absorption of a photon by an electron in the given band results in transition to a higher level inside the band. Relaxation is possible by energy release in form of phonons (thermalization). The coupling strength of this process is proportional to the carrier density. A higher photon energy leads to lower coupling strength.
- **Phonon transitions.** Direct excitation of lattice-vibrations (phonons) by low energy photons.
- **Excitonic transitions.** An exciton is found, when electron and holes are bound by coulomb interaction. Radiative recombination is possible and results in annihilation of the exciton.

Which of the aforementioned processes is dominant, depends on the wavelength, bandgap energy, doping concentration and type of semiconductor (indirect/direct). For photon energies $h\nu < E_g$ the material is relatively trans-

parent, while for greater photon energies the material is opaque and the band-to-Band transitions are the dominating effect. The region in between is called the absorption edge (see figure 3.4). For intrinsic silicon $E_g(\text{Si}) = 1.1 \text{ eV}$, which results in $\lambda_g = 1.1 \mu\text{m}$ for the absorption edge. For direct semiconductors the absorption coefficient shows a more abrupt change than for indirect semiconductors. In the test conducted during work on the thesis an infrared laser was used, with a wavelength of $(1055.6 \pm 7.8) \text{ nm}$. The corresponding absorption coefficient for intrinsic silicon at 300 K is $(780 \pm 115) \mu\text{m}$.

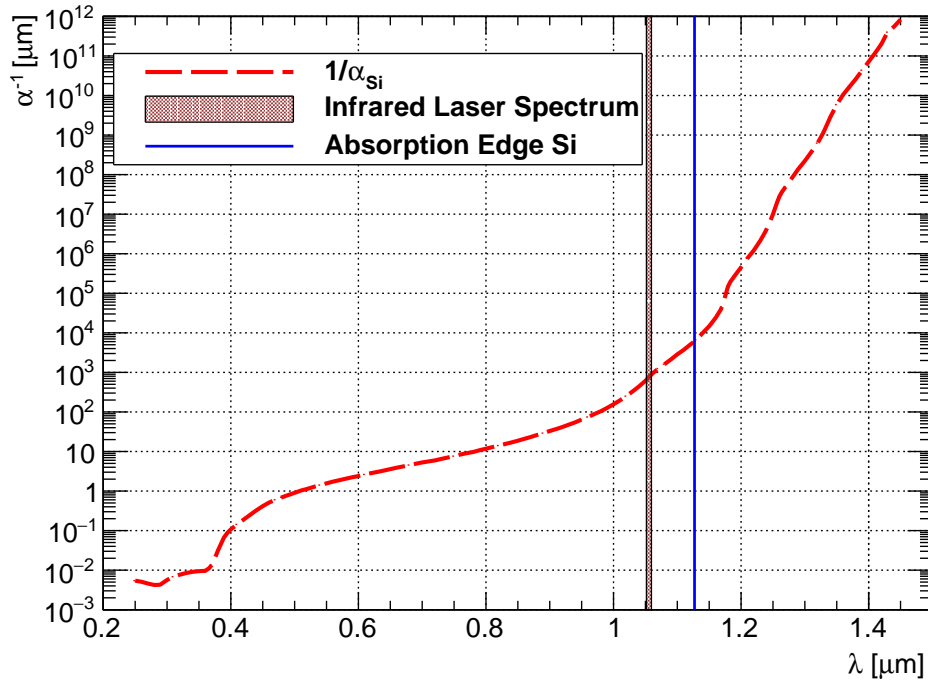


Figure 3.4: The inverse absorption coefficient for intrinsic silicon at 300 K, the wavelength of the infrared laser used and the absorption edge for silicon. Data taken from [22].

3.5 Laser light and beam quality measures

Laser beams can be used for characterization of a semiconductor detector [23, 24]. A variety of parameters can be measured, such as charge collection efficiency, position resolution, pulse shape, pixel-mapping and dead-channels

[25–27]. One measures the signal produced by processes described in section 3.4 versus the readout chip settings, position of the laser spot, bias voltage of the sensor etc.

For a semiconductor **Laser** diode the population inversion is achieved by injection of electrons in a p-n junction [28, pp. 553-562]. Most of modern semiconductor **Laser** use forward biased PIN diodes. In order to obtain information about the dynamics of the charge collection, the laser pulses must be shorter than the typical time scale of charge collection, given mainly by capacitance, resistance and electron-hole mobility of the device. Pulse durations of $\mathcal{O}(1 \text{ fs})$ are achieved with mode-locked lasers. This technique couples different oscillation modes in the laser resonator. For active mode locking a switched optical modulator in the laser resonator is used, where the refraction index is modulated via the electron density. Passive mode locking relies on a saturable absorber in the laser resonator [29]. Superposition of phase coupled laser modes in the time domain produces short, sharp laser pulses with ideal repetition frequency of $f_{\text{rep}} = 1/(\Delta t) = c/2L$, where L is the longitudinal extend of the laser resonator and c is the velocity of light in the resonator medium [30, p. 69].

The excellent timing properties of a laser system in comparison to signals from a radioactive source, make the system suitable for time resolution studies and pulse shape reconstruction of the analog signal in a detector with binary readout.

3.6 Gaussian beams

The following is a short introduction to the beam quality parameter as given in [21, chapter 3]. A gaussian laser beam is a solution for the paraxial Helmholtz equation.

The complex amplitude of the electric field at position \mathbf{r} reads

$$U(\mathbf{r}) = A_0 \frac{W_0}{W(z)} \exp\left(\frac{-\rho^2}{W^2(z)}\right) \exp\left(-jkz - jk\frac{\rho^2}{2R(z)} + j\zeta(z)\right), \quad (3.12)$$

where

$$W(z) = W_0 \left(1 + \left(\frac{z}{z_0} \right)^2 \right) \quad (3.13)$$

$$R(z) = z \left(1 + \left(\frac{z_0}{z} \right)^2 \right) \quad (3.14)$$

$$\zeta(z) = \tan^{-1} \frac{z}{z_0} \quad (3.15)$$

$$W_0 = \left(\frac{\lambda z_0}{\pi} \right)^{1/2}, \quad (3.16)$$

with symbols defined in table 3.2.

Table 3.2: Symbols and constants for gaussian beam optics energy [21, chap. 3]

| Symbol | Definition | Value/Unit |
|-----------------|---------------------------|--------------------|
| λ | Wavelength in medium | |
| k | Wavenumber in medium | $k = 2\pi/\lambda$ |
| $A(\mathbf{r})$ | Complex envelope of wave | |
| $U(\mathbf{r})$ | Complex amplitude | |
| z_0 | Rayleigh range | |
| $W(z)$ | Beam width | |
| $R(z)$ | Curvature | |
| $I(\rho, z)$ | Intensity | $ U(\rho, z) ^2$ |
| W_0 | Waist radius | |
| $2W_0$ | Waist diameter/ spot size | |
| $\zeta(z)$ | Phase retardation | |
| $2z_0$ | Depth of focus | |

With the definitions from table 3.2 the intensity

$$I(\rho, z) = I_0 \left(\frac{W_0}{W(z)} \right)^2 \exp \left(-\frac{2\rho^2}{W^2(z)} \right) \quad (3.17)$$

is described by a Gaussian function for the radial distance ρ . On the beam axis therefore the intensity is given by

$$I(0, z) = I_0 \left(\frac{W_0}{W(z)} \right)^2 = I_0 \frac{1}{1 + \left(\frac{z}{z_0} \right)^2}, \quad (3.18)$$

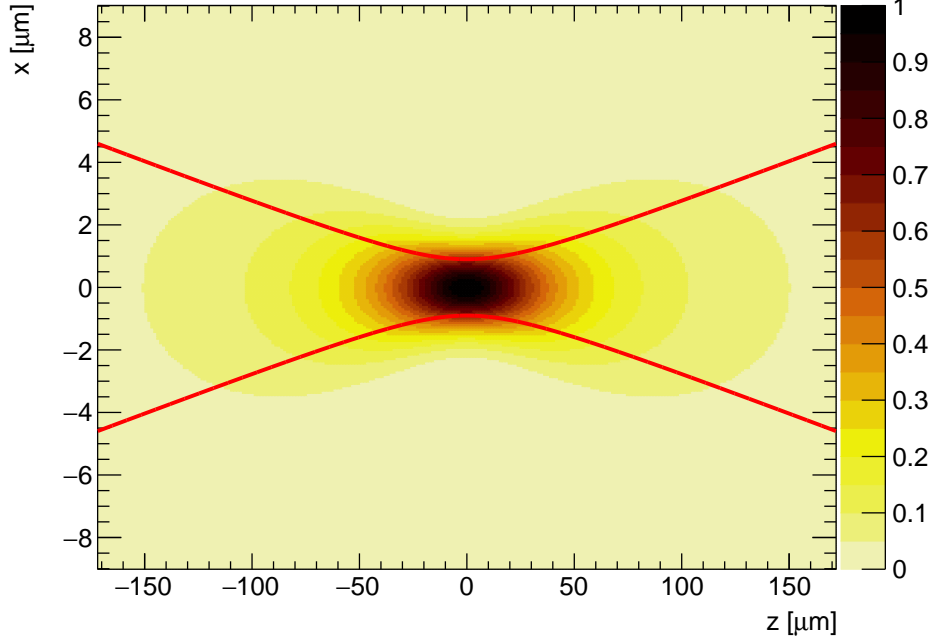


Figure 3.5: $I(z, x)/I_0$ of an ideal gaussian beam in intrinsic silicon without absorption. The beam parameters are $2W_0 = 3.6 \mu\text{m}$, $\lambda = 1056 \text{ nm}$, $n_{\text{Si}} = 3.554$. The red lines indicate, where $I(x, z)/I(x=0, z) = 1/e^2$.

where the Rayleigh range z_0 is defined as $I(z_0) = 0.5I_0$. At $\rho = W(z)$ the intensity is $I = e^{-2}I_0$ and 86 % of the laser power is contained inside a circle with this radius. The beam radius from equation (3.13) may be written as

$$W(z) = \frac{W_0}{z_0}z = \theta_0 z \quad (3.19)$$

for $z \gg z_0$.

Figure 3.5 shows a plot of the relative intensity with the beam parameters of the laser system used in the scope of this thesis.

This gives rise to the definition of the beam parameter product

$$\theta_0 = \frac{\lambda}{\pi W_0} \quad (3.20)$$

Equation (3.20) shows, that wavelength, half angle and waist size are related for a gaussian beam. A general solution of the Helmholtz equation leads to Bessel/Hermite functions and a general form for equation (3.20) is

$$\theta_0 = M^2 \frac{\lambda}{\pi W_0}, \quad (3.21)$$

where M is introduced as the beam quality factor. For an ideal Gaussian single mode TEM_{00} beam $M = 1$. Real beams contain higher modes and therefore the values for M are greater than 1. The depth of focus is given by $2z_0$, which is the distance, where the beam radius is contained in $\sqrt{2}W_0$. The relation in equation (3.16) states that a small wavelength and a small Rayleigh range results in small waist size. The real part of the refractive index for silicon $n(\lambda = 1056 \text{ nm}) = 3.554$ [22] has the effect, that the Rayleigh range is $z_0(\text{Si}) = n(\lambda = 1056 \text{ nm})z_0$.

The generation rate $G_{p/n,light}$ of **EHPs** for photons of a given wavelength reads

$$G_{p,light}(\mathbf{r}) = G_{n,light}(\mathbf{r}) = \alpha \frac{I(\mathbf{r})\delta E}{E_{ph}e}, \quad (3.22)$$

where α is the absorption coefficient in silicon, δE is the mean energy to create an **EHP**, E_{ph} the photon energy, e the elementary charge.

The plots in figures 3.6a to 3.6e show $G_{p,light}(\mathbf{r})$ not to scale for different positions of the beam waist with respect to the silicon surface at $z = 0$. The charge collected at the electrodes follows the primary charge distribution in the bulk. Diffusion leads to broadening of the charge distribution.

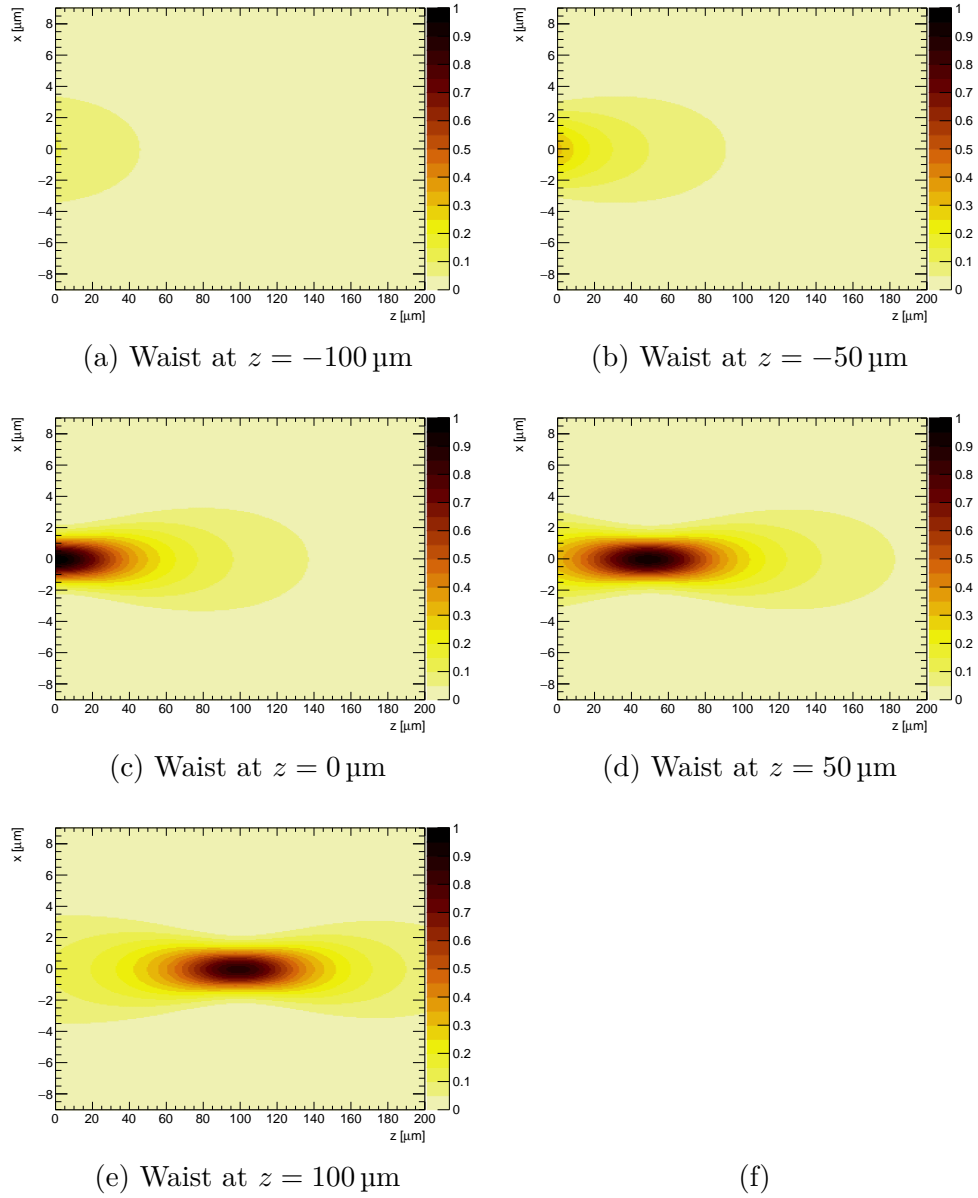


Figure 3.6: Relative **EHP** generation rate in silicon with silicon surface at $z = 0$ and beam waist at different z -positions absorption included (a-e).

Chapter 4

Semiconductor physics

4.1 Intrinsic silicon

Silicon as semiconductor material is used in high energy physics for particle detectors. The most important aspects and properties of the material are shortly summed up as presented in [31, chap. 1] in the following.

Silicon has a diamond face centered cubic lattice structure. The bandstructure in figure 4.1a, which is a (E - \mathbf{k}) relationship, of Si is given by the solution of the Schrödinger equation using the Bloch theorem. For semiconductors the conduction band with the lowest energy E_C and the valence band with the highest energy are separated by the band gap energy $E_G = E_V - E_C$. The effective mass of a charge carriers is defined as

$$E(k) = \frac{\hbar^2 k^2}{2m_{eff}}. \quad (4.1)$$

For Si the minimum of the conduction band and the maximum in the valence band do not coincide in the k -space, which is called indirect band gap (see figure 4.1a). This has several consequences for charge carrier generation and recombination processes (see section 3.3). The band gap energy is temperature dependent and for Si $E_G(T = 300 \text{ K}) = 1.12 \text{ eV}$. Semiconductor properties like resistivity ρ can be modified in a wide parameter range

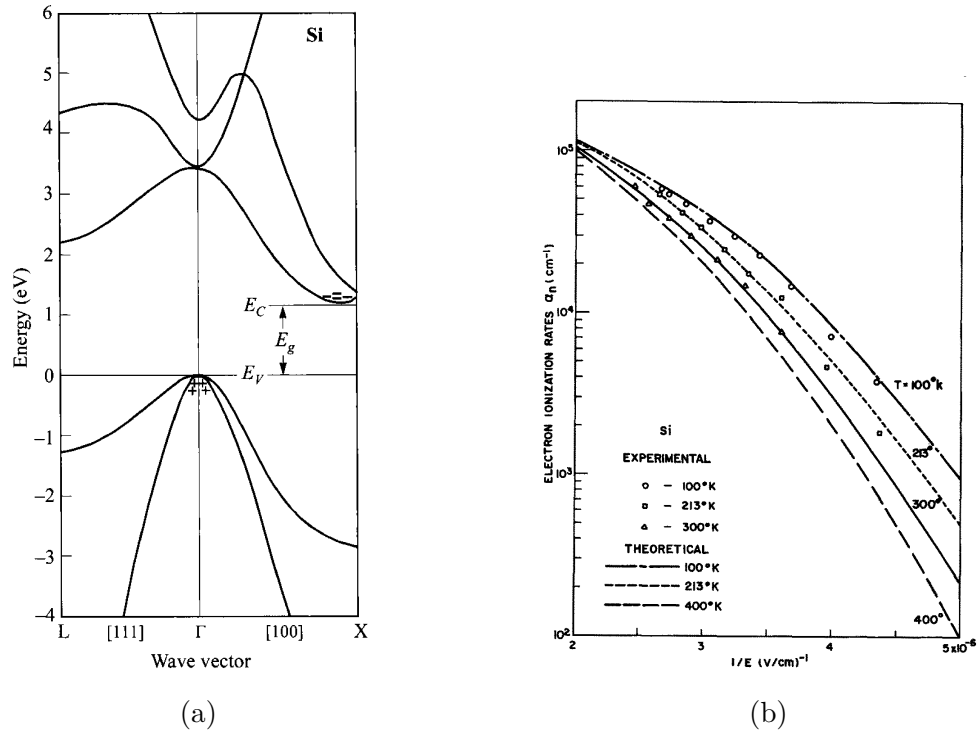


Figure 4.1: (a) The bandstructure of silicon from [31, p. 14]. (b) The electron ionization rates for different temperatures for silicon from [32].

by doping, which means deliberately adding impurities. Elements from main group III like boron are used as acceptors to create p-type material, while group V elements like phosphorus are used as donors to create n-type silicon. Donor atoms donate additional electrons to the conduction band, while acceptor atoms create holes in the valence band, by accepting one electron to form four covalent bonds.

Carrier concentration

The charge carrier concentration n in intrinsic silicon is

$$n = \int_{E_C}^{\infty} N(E)F(E)dE, \quad (4.2)$$

where $N(E)$ is the density of states and $F(E)$ is the occupancy. The occupancy is a Fermi-Dirac distribution function and strongly depends on temperature.

$$F(E) = \frac{1}{1 + \exp((E - E_F)/kT)}, \quad (4.3)$$

where the Fermi-Energy E_F can be derived from the charge neutrality condition. The effective density of states in the conduction band is

$$N_C = 2 \left(\frac{2\pi m_{de} kT}{h^2} \right)^{3/2} M_C, \quad (4.4)$$

where m_{de} is the density-of-state effective mass for electrons and M_C is the number of equivalent minima in the conduction band. Using the Fermi-Dirac integral

$$F_{1/2} \left(\frac{E_F - E_C}{kT} \right) = \int_{E_C}^{\infty} \frac{((E - E_C)/kT)^{1/2} dE}{1 + \exp((E - E_F)/kT) kT}, \quad (4.5)$$

equation (4.2) is rewritten as

$$n = N_C \frac{2}{\sqrt{\pi}} F_{1/2} \left(\frac{E_F - E_C}{kT} \right). \quad (4.6)$$

In non-degenerate semiconductors the doping concentration is smaller than N_C and $(E_C - E_F)/kt \gg 1$. In this case Boltzmann statistics applies and equation (4.6) becomes

$$n = N_C \exp \left(-\frac{E_C - E_F}{kT} \right) \quad (4.7)$$

For the hole density a similar approach results in

$$p = N_V \exp \left(-\frac{E_F - E_V}{kT} \right), \quad (4.8)$$

where N_V is the effective density of states in the valence band and is given by

$$N_V = 2 \left(\frac{2\pi m_{dh} kT}{h^2} \right)^{3/2}, \quad (4.9)$$

where m_{dh} is the density-of-state effective mass of holes in the valence band.

For intrinsic semiconductors in thermal equilibrium the rate of excitation of electrons from the valence band to the conduction band equals the rate of recombination from the conduction band and the concentration of electrons and holes are equal

$$n_i = n = p, \quad (4.10)$$

where n_i is the intrinsic charge carrier density. Using equation (4.10) the Fermi level is

$$E_F = E_i = \frac{E_C + E_V}{2} + \frac{kT}{2} \ln \left(\frac{N_V}{N_C} \right), \quad (4.11)$$

and for n_i

$$n_i = \sqrt{N_C N_V} \exp \left(\frac{-E_G}{2kT} \right), \quad (4.12)$$

$$n_i \propto T^{3/2} \exp \left(\frac{-E_G}{2kT} \right), \quad (4.13)$$

is obtained, where E_G is the band gap energy.

Donor, Acceptors and the Fermi Energy

Donors or acceptors add impurity energy levels E_D and E_A , which usually lie in the band gap. This donor levels are either neutral, if filled with electron and positive, if empty. An acceptor level is neutral, if empty and positive, if filled with an electron. At room temperature for impurity introduced energy levels close to the band edges the ionization energy is comparable to kT and therefore the dopants are fully ionized. The ionized impurity concentration is N_D^+ for donors and N_A^- for acceptors. The Fermi level in a doped n-type semiconductor is shifted and obtained as a solution of

$$n_{n0} = N_D = N_C \exp \left\{ \frac{-E_C - E_F}{kT} \right\} = n_i \exp \frac{E_F - E_i}{kT}, \quad (4.14)$$

assuming $N_D \gg N_A$ and complete ionization of the impurities. A similar calculation is done for p-type material.

4.2 Charge carrier transport in semiconductors

The important processes for charge carrier transport in semiconductors drift and diffusion, according to [15, chap 4.7] and [33, chap 2.5], are introduced in the following. In case an electric field \mathbf{E} is present, the charge carriers are accelerated between random collisions. The drift velocity $\mathbf{v}_{n/p}$ for electrons and holes is given by,

$$\mathbf{v}_n = \frac{-q\tau_c}{m_{eff}^n} \mathbf{E} = \mu_n \mathbf{E} \quad (4.15)$$

$$\mathbf{v}_p = \frac{-q\tau_c}{m_{eff}^p} \mathbf{E} = \mu_p \mathbf{E}, \quad (4.16)$$

with symbols defined in table 4.1. The charge carrier mobility $\mu_{n/p}$ depends on temperature and doping concentration. For high fields deviations from equation (4.15) occur. Consequently there a field dependent mobility was defined by Caughey and Thomas, which includes saturation of charge carrier velocities in high electric fields, due to energy transfer to the crystal lattice by emission of optical phonons [34].

Table 4.1: Symbols and constants for equation (4.15)

| Symbol | Definition |
|-------------|---------------------------------|
| v_n | Drift velocity for electrons |
| v_p | Drift velocity for holes |
| q | Elementary charge |
| τ_c | Mean time between collisions |
| m_{eff}^n | Effective mass electron |
| m_{eff}^p | Effective mass hole |
| μ_n | Electron mobility |
| μ_p | Hole mobility |
| n_n | Electron concentration |
| n_p | Hole concentration |
| D_n | Diffusion coefficient electrons |
| D_p | Diffusion coefficient holes |
| k | Boltzmann constant |

The second important mechanism is diffusion, which is a macroscopic effect, caused by the microscopical random movement of charge carriers in the crystal lattice. The process is described by the diffusion equation, which is a continuity equation. In case no additional generation and recombination of charge carriers is considered for the current density of electrons and holes it reads,

$$\mathbf{J}_n = q\mu_n n_n \mathbf{E} - qD_n \nabla n_n \quad (4.17)$$

$$\mathbf{J}_p = q\mu_p n_p \mathbf{E} - qD_p \nabla n_p \quad (4.18)$$

$$D_n = \frac{kT}{q} \mu_n \quad (4.19)$$

$$D_p = \frac{kT}{q} \mu_p \quad . \quad (4.20)$$

There are several components for the electron and hole mobility and the reciprocal of the mobility is given by sum of reciprocals of the contributions from the different processes,

$$\frac{1}{\mu} = \sum_i \frac{1}{\mu_i} \quad (4.21)$$

The important contributions are **Acoustic Phonon Scattering (APS)** with a temperature dependence

$$\mu_{\text{APS}} \propto \frac{1}{m_{\text{eff},c}^{5/2} T^{3/2}} \quad , \quad (4.22)$$

and the **Ionized Impurity Scattering (IIS)**,

$$\mu_{\text{IIS}} \propto \frac{T^{3/2}}{n_{\text{II}}(T) m_{\text{eff}}^{1/2}} \quad (4.23)$$

where n_{II} is the impurity concentration. The **IIS** is a coulomb scattering process. μ_{IIS} decreases with higher temperatures, because of the smaller deflection for charge carriers with higher energies.

For high electric fields the effective temperature of charge carriers increases and more energy is transferred to the crystal lattice.

Interactions with optical phonons become relevant at very high electrical fields. These processes lead to decreasing mobility and saturation of drift velocity for high electric fields.

For a very high electric field, the energy a charge carrier gains between two subsequent collisions may be high enough to generate an additional **EHP** by impact ionization, which leads to avalanche generation.

The standard values for intrinsic silicon at 300 K are given in table 4.2. For n-type semiconductors the resistivity is defined as,

$$\rho = \frac{1}{q\mu_n n_n} \quad , \quad (4.24)$$

where μ_n is the electron mobility and n the electron concentration.

Table 4.2: Material constants for intrinsic silicon at 300 K.

| Symbol | Definition | nominal Value/Unit |
|---------|---------------------------------|--|
| μ_n | Electron mobility | 1450 cm ² V ⁻¹ s ⁻¹ |
| μ_p | Hole mobility | 500 cm ² V ⁻¹ s ⁻¹ |
| D_n | Diffusion coefficient holes | 36 cm ² s ⁻¹ |
| D_p | Diffusion coefficient electrons | 12 cm ² s ⁻¹ |
| kT/q | Thermal voltage | 0.025 86 V |

4.3 Continuity equation

Taking into account the processes for generation and recombination of **EHPs** the full dynamics in the semiconductor are described by the continuity equations,

$$\frac{\partial n_n}{\partial t} = G_n - R_n + \frac{1}{q} \nabla \cdot \mathbf{J}_n \quad (4.25)$$

$$\frac{\partial n_p}{\partial t} = G_p - R_p + \frac{1}{q} \nabla \cdot \mathbf{J}_p, \quad (4.26)$$

$$(4.27)$$

where $G_{n/p}$ and $R_{n/p}$ are the total generation and recombination rates for electrons and holes.

4.4 The p-n junction

The p-n junction is the basis of a modern tracker detector and many other modern electronic devices such as computers, mobile phones etc. A segmented p-n junction is part of every silicon sensor, where each segment is an isolated pixel or strip. In this section the relevant characteristics for a p-n junction are introduced and the capacitance voltage characteristic in reverse bias is derived.

A p-n junction is a two terminal device, with two distinct semiconductor regions, namely p-type and n-type material, with acceptor density N_A and donor density N_D . For simplicity the 1D case of an abrupt junction with zero bias voltage is considered, where the respective impurity concentrations are constant on both sides of the junction. Due to the strong charge carrier concentration gradient a diffusion current I_{diff} builds up. Electrons from the n material diffuse into the p material and holes from the p material into n region. This leads to a build up of a negative net charge in the p region and of positive net charge in the n region. An electric field counteracts the diffusion and sweeps out the mobile charge carriers in the boundary region, which results in a drift current I_{drift} .

For this example, the charge carrier concentration is given by

$$\rho = \begin{cases} -qN_A & \forall -x_p < x < 0, \\ +qN_D & \forall 0 < x < x_n. \end{cases} \quad (4.28)$$

The boundary conditions for solving the Maxwell equation $\frac{dE}{dx} = \rho(x)/\epsilon\epsilon_0$ are $E(-x_p) = E(x_n) = 0$. Therefore the electric field yields

$$E = \begin{cases} \frac{-qN_A}{\epsilon\epsilon_0}(x + x_p) & \forall -x_p < x < 0, \\ \frac{-qN_D}{\epsilon\epsilon_0}(x - x_n) & \forall 0 < x < x_n, \end{cases} \quad (4.29)$$

and for the electrostatic potential

$$\phi = \begin{cases} \phi_p + \frac{qN_A}{2\epsilon\epsilon_0} (x + x_p)^2 & \forall -x_p < x < 0, \\ \phi_n + \frac{qN_D}{2\epsilon\epsilon_0} (x - x_n)^2 & \forall 0 < x < x_n. \end{cases} \quad (4.30)$$

This defines a built-in voltage V_{bi} , which depends on the difference of the doped Fermi levels to the intrinsic Fermi level in the n and p regions

$$V_{bi} = \phi_p - \phi_n \quad (4.31)$$

$$= \frac{kT}{q} \ln N_A/n_i + \ln N_D/n_i \quad (4.32)$$

$$= \frac{kT}{q} \ln \frac{N_A N_D}{n_i^2} \quad (4.33)$$

$$= V_{th} \ln \frac{N_A N_D}{n_i^2} \quad (4.34)$$

For a typical silicon sensor of n-strips in p-bulk material with peak doping concentrations as in table 7.5 at room temperature the built-in voltage is $V_{bi} = 0.655$ V. For the abrupt junction, x_p and x_n depend on V_{bi}, N_A, N_D and can be expressed as [15, p. 293]

$$x_p = \sqrt{\frac{2\epsilon\epsilon_0 V_{bi}}{q} \frac{N_D}{N_A(N_D + N_A)}}, \quad (4.35)$$

$$x_n = \sqrt{\frac{2\epsilon\epsilon_0 V_{bi}}{q} \frac{N_A}{N_A(N_D + N_A)}}, \quad (4.36)$$

$$W = x_n + x_p = \sqrt{\frac{2\epsilon\epsilon_0 V_{bi}}{q(N_A + N_D)}} \left(\sqrt{\frac{N_A}{N_D}} + \sqrt{\frac{N_D}{N_A}} \right) \quad (4.37)$$

$$W = \sqrt{\frac{2\epsilon\epsilon_0 (N_A + N_D) V_{bi}}{q N_A N_D}} \quad (4.38)$$

So for an abrupt junction with doping concentrations from table 7.5 the width of the natural space charge region is $W = x_p + x_n = 28.9 \mu\text{m} + 2.9 \times 10^{-6} \mu\text{m}$.

When a reverse bias voltage V_b is applied to the junction replace V_{bi} by $V_{bi} - V_b$.

4.4.1 Capacitance of a p-n junction

Considering the reverse biased p-n junction as a parallel plate capacitor, due to the low carrier concentration in the depletion region, then the capacitance per area is defined as

$$C/A = \frac{\epsilon\epsilon_0}{W} \quad (4.39)$$

$$= \sqrt{\frac{q\epsilon\epsilon_0 N_A N_D}{2(N_A + N_D)(V_{bi} - V_b)}} \quad (4.40)$$

The finite thickness gives rise to the definition of the full depletion voltage V_{fd} , which is reached, when the depletion region extends over the full thickness of the bulk material. For $V_b < V_{fd}$ it holds $C^{-2} \propto V_b$.

4.4.2 Characteristics of segmented diodes

A segmented diode is an essential building block in a particle detector. The unit cell of an infinitesimally long segmented diode is characterized by pitch p and width w of the segmented implant. The segmentation results in a higher full depletion voltage and lower full depletion capacitance. For a given ratio w/p and thickness d , an analytic expression for V_{fd} is found [35]

$$V_{fd} = V_{fd0} \left(1 + 2 \frac{p}{d} f\left(\frac{w}{p}\right) \right), \quad (4.41)$$

where $f(w/p)$ is shown in figure 4.2 and V_{fd0} is for the unsegmented diode.

For a silicon strip sensor with $w = 25 \mu\text{m}$ and $p = 100 \mu\text{m}$ the result of equation (4.41) is $V_{fd} = 1.32V_{fd0}$.

4.4.3 Junction Breakdown

Three different mechanism are known to cause breakdown of a reverse biased p-n junction [31, chap. 2.4].

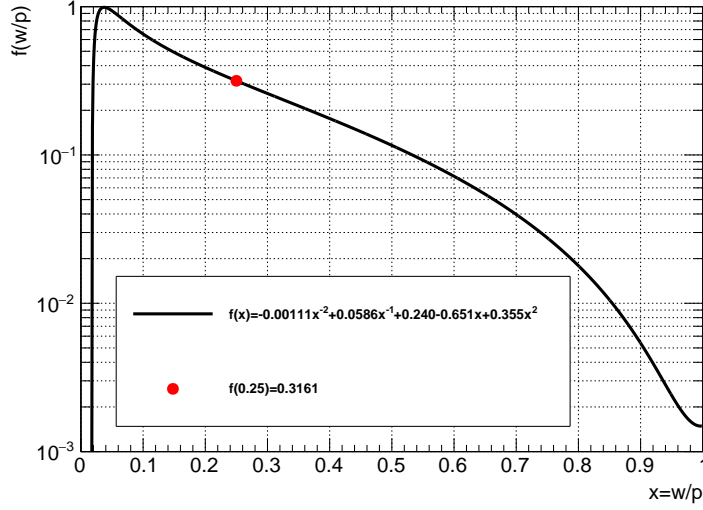


Figure 4.2: The function $f(w/p)$ from [35].

Thermal instability is caused by heat dissipation and the negative temperature coefficient of the differential resistance. Heat dissipation leads to self heating, thermal runaway and destruction of the device, if no limiting series resistor is used.

The tunneling effect occurs, when the electric field reaches $10 \times 10^6 \text{ V cm}^{-1}$, by band-to-band transitions. Tunneling is relevant for the breakdown voltage $V_{bd} < 4E_g/q$. This process has a negative temperature coefficient or the breakdown voltage decreases with increasing temperature.

Impact ionization or avalanche multiplication occurs, when charge carriers obtain enough energy between two subsequent collisions, that further charge carrier pairs are produced. In the following the ionization integral according to [31, chap. 2.4] is introduced. It is convenient to define the impact ionization coefficient $\alpha_{n/p}$, which designates the number of **EHPs** generated per unit distance for a moving charge carrier.

$$\alpha = \frac{1}{nv_{n/p}} \frac{dn}{dt} \quad (4.42)$$

depends on temperature, electric field and background doping concentration [32].

In a depletion region of width W_{Dm} , the electron and hole current will increase from the initial values $I_{p0}(x = 0)$ to $M_p I_{p0}$ and $I_{n0}(x = W_{Dm})$ to $I_n(x = 0) = I - I_{p0}$ reaching the opposite end of the junction. $M_p = I_p(x = W_{Dm})/I_p(x = 0)$ is the multiplication factor of holes. The total current at the steady state is $I = I_p + I_n$. For the infinitesimal distance dx it holds:

$$dI_p = I_p \alpha_p dx + I_n \alpha_n dx \quad \text{or,} \quad (4.43)$$

$$\frac{dI_p}{dx} - (\alpha_p - \alpha_n) I_p = \alpha_n I \quad (4.44)$$

The solution of equation (4.43) defines the ionization integral $\Phi_{n/p}$

$$1 - \frac{1}{M_p} = \int_0^{W_{Dm}} a_p \exp \left[- \int_0^x (\alpha_p - \alpha_n) dx' \right] dx, \quad (4.45)$$

$$(4.46)$$

with the breakdown condition

$$1 = \int_0^{W_{Dm}} a_p \exp \left[- \int_0^x (\alpha_p - \alpha_n) dx' \right] dx, \quad (4.47)$$

$$(4.48)$$

which is reached, when the gain $M \rightarrow \infty$. For silicon the electron component is dominant for charge carrier multiplication and the avalanche condition is reached earlier for electrons due to their lower effective masses and higher mobility.

Chapter 5

Silicon sensors

A silicon sensor is segmented in a high number of diodes, which are readout separately and are reverse biased. Each of these diodes, is formed by a p-n junction and characterized by the w/p ratio. Ionizing particles generate **EHPs** in the depletion region. The produced charges move due to the electric field in the sensor towards their corresponding electrodes. The movement of the charges induces charges in the readout electrodes. The temporal change of the influenced charges on the electrodes is given by the movement of the charges in the active sensor volume and equals the signal current, which is generated by the external voltage source [36, 37].

In this section the sensor geometry and building blocks of a silicon sensor are explained on the basis of the prototype sensors, which were tested during the work on this thesis (see section 6.3). The terms cell, strip, macro-pixel and pixel refer to different cell geometries.

5.1 Sensor material

The first silicon sensors for high energy physics were built with n-type bulk material and p-type strip implants [38–40], due to reasons of lower cost and availability of n-type bulk material. However p-type substrate material has shown to be more tolerant to irradiation and ensures the required radiation

hardness for a tracking system in the **HL-LHC** era [41–48]. For fast charge collection full depletion of the bulk material is necessary, which is achieved with high resistive material of about $4\text{ k}\Omega\text{ cm}$ to $7\text{ k}\Omega\text{ cm}$ resistivity (ρ), which is equivalent to an effective bulk doping concentration around $10 \times 10^{12}\text{ cm}^{-3}$. The typical thickness of the final device is around $150\text{ }\mu\text{m}$ to $350\text{ }\mu\text{m}$. However the thickness of the active volume depends on the production process and may be smaller than the physical thickness, if deep diffused material is used. Physically thinned material is important in tracker and pixel detectors, where the material budget is a concern. In addition radiation tolerance is also a function of physical thickness. For a physical thickness below $300\text{ }\mu\text{m}$ special production techniques are necessary. Two different methods to increase the radiation tolerance of a silicon sensor are known, namely defect engineering and design optimization. Defect engineering addresses the possibility to add deliberately impurities to the base material, e.g. oxygen enrichment [41, 49–51]. In the microscopic scale oxygen enrichment results in a suppressed deep-acceptor level and an enhanced bistable donor level in the band-gap, which significantly improves the radiation hardness to detector grade silicon. Typically the oxygen enriched sensor grade silicon is produced in either with float-zone method or Czochralski process [52, p. 1.8.1].

Design optimization refers to the chosen base material, the sensor geometry, which can be altered, if it meets the constraints required by the experiment and the sensor thickness. For the sensor thickness the trade off in radiation hardness has to be chosen. Increased thickness leads to increased dark current from the bulk and deteriorated detector noise (see section 6.2.1). However also the amount of charge created in the active volume is increased. The optimizations for the **CMS** tracking sensors **HL-LHC** yield $200\text{ }\mu\text{m}$ [7].

5.2 Cell geometry

In order to achieve the desired position resolution of $\mathcal{O}(10\text{ }\mu\text{m})$ for a tracking detector the cell dimension in the sensitive direction is in the order or $\mathcal{O}(100\text{ }\mu\text{m})$. The size of the cell in the not sensitive direction is constraint by

the expected occupancy, the wafer size and the dark-current induced noise component.

In p-bulk material an electron accumulation layer builds up at the interface, due to the oxide charge concentration in the SiO_2 top layer and at the material interface, which requires in turn additional p-stop implant to isolate the n-implant cells. The geometry and doping profiles of the p-stop isolation affect the sensor properties like HV-stability, radiation tolerance and inter-cell resistance. A common design with two isolated p-stop implants between the n-implants is called atoll configuration. However different other possibilities exist, like p-stop common, where the p-stop implant is not segmented among the cells, and p-spray, which refers to an unstructured p-implant on the whole wafer. Exemplarily the unit cell building block of a p-type macro-pixel sensor is shown in figure 5.1a. The n-type cell implants are shown in green, the p-stop in red and the metal layer on top of the cell implant in light blue. An additional p-type doping at the backplane electrode of the sensor avoids the formation of a rectifying Schottky-contact [52, p. 54].

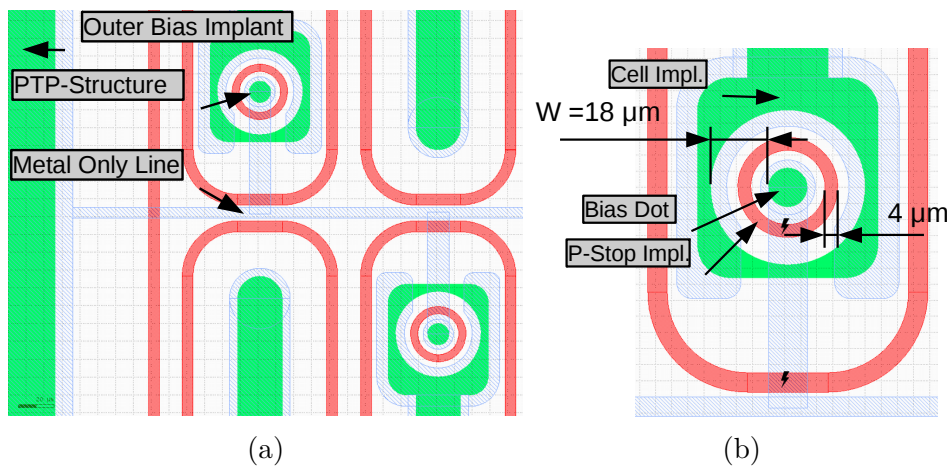


Figure 5.1: (a) shows a unit cell of the **PS-p light (PS-p light)** prototype sensor (see 6.3) with bias ring with n-implant below, metal bias rail and **Punch-Through Protection (PTP)** structures. In (b) the important **PTP** design parameters, the width of p-stop implant (red) and distance between the n-implants (green) are introduced. The lightning shows critical points for HV-stability of the structure, which depend also on the quality and thickness of the silicon dioxide layer on top.

The coupling of the cells to the **Charge Sensitive Amplifier (CSA)** of a readout chip is realized, for instance, via direct connection in form of bond wires for strip sensors, or with flip-chip technology for pixel sensors. This technique requires a leakage current compensation in the readout chip, e.g. a current mirror [33] and is referred to as DC-coupling. Figure 6.7b shows the layer stackup of a DC-coupled sensor, where the cell implant is connected to an overhanging metal layer via contact holes through a dielectric. Alternatively AC-coupling makes use of an additional insulating layer (e.g. of SiO_2) on top of cell implants, which are biased via the bias grid (see section 5.4). A metal layer, which overhangs the implanted cell electrode, on top of the insulating layer is connected to the readout chip. A signal is induced in the metal electrode via capacitive coupling to the implanted electrode. This method is mainly chosen for strip sensors and eliminates the necessity for additional circuits in the readout chip and the parallel noise component (see section 6.2.1).

5.3 Sensor periphery and sensor protection

The sensor is protected from scratches and humidity effects by a SiO_2 passivation layer, which covers the front side surface of the device. The passivation oxide charges should be well defined. Openings in the passivation allow electrical contact to the aluminum metal layer.

A typical sensor periphery is shown in figure 5.2. A bias ring frames the sensor active area and ensures a homogeneous potential for all strips. For this sensor the bias ring forms part of the bias grid, described in section 5.4. During normal operation of this DC-coupled sensor, however the pixels are biased via the readout chip and therefore the bias ring has field shaping and overcurrent protection purpose only.

The floating guard ring ensures a smooth potential drop from the p-implanted edge and minimizes the edge effects in the active area.

Cracks from the cutting process of the sensors lead to additional current due to the high density of defects at the cutting edge. Therefore leakage current

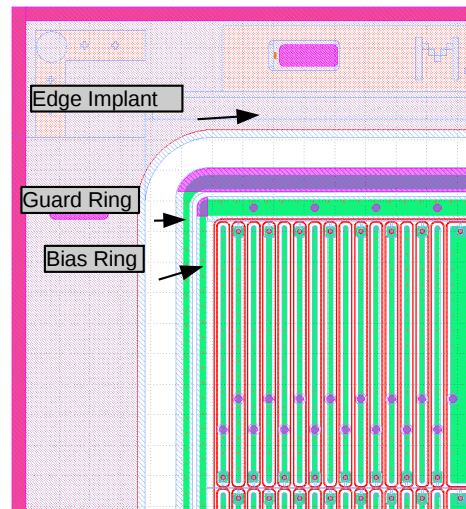


Figure 5.2: The periphery of a macro-pixel sensor has a bias ring surrounding the active area, a guard ring and p-implanted edge region.

suppression is achieved with the edge p-implant field shaper, which causes the potential to drop on the front side of the sensor [52, p. 34].

5.4 Biasing circuit via Punch-Through Protection

For testing purpose it is favorable to have a bias grid, which connects to the cell (strip/pixel) implants via a high resistive resistor. In principle different options like polysilicon resistors, FOXFET, open p-stop and simple punch-through are feasible [33, chap. 7.8.1],[53, chap. 2.2.7], [15, chap. 8.5.4]. For a cell with direct connection to a readout chip a **PTP**, as shown in figure 5.1b, is the natural choice, keeping the production process as simple and inexpensive as possible. The bias grid has several advantages:

- It allows the measurement of the total sensor current, in a similar potential configuration, as if the strips were biased via the readout chip. Measurement of single cell dark currents are possible and bad cells with higher dark current can be identified. The dispersion of the single cell currents can be used as sensor quality parameter.
- In addition a **PTP** protects the readout chip from high input currents in case of beam loss scenarios [54, 55]. Furthermore the bias grid ensures a good homogeneity of the electric field. The chosen **PTP** design maintains a high geometric efficiency, in contrast to the early linear designs of the structure.

5.5 Design parameters PTP

The electrical specifications of a **PTP** resistor are constraint by the aforementioned purpose. For a typical pixel sensor this resistor is realized as a bias dot, connected to the metal line of the outer bias ring, a ring of p-stop implant, which separates the depletion regions in the unbiased case and is surrounded by the cell implant. Typically the width of the p-stop implant around the bias dot is half of the width of the p-stop implant, which directly separates the cell n-implants from each other. In such a configuration it is possible to achieve strip isolation with a defined connection to the bias rail.

Trade offs must be considered for a good compromise:

- First of all the size of the bias dot should be as small as possible, because charge collected on the implanted dot is lost, which leads to inefficiencies [56, chap. 8.8.1],[53, p. 96].
- Typically the bias dot implant is the smallest feature on the sensor and respective the smallest metal overhang of about $2\mu\text{m}$, which ensures good HV-stability of the device, is found in this region. Mask misalignment affects the region with minimum metal overhang the most and the device HV-stability is possibly deteriorated. However mask misalignment is a partially a statistical process and therefore during large-volume production a structure with very small metal overhang may lower the yield.
- With decreasing radius of the bias dot implant however, the maximum electrical field increases, leading eventually to electrical breakdown and microdischarge [57, 58].
- During operation the current across the **PTP** is very small, because the cell implants are directly biased via the readout chip. This is why no excess noise contribution is expected, which is different for an AC-coupled strip sensor with this biasing method [59, 60].

During standard sensor testing, the electrostatic potential of the cell implant is floating and depends strongly on the width of the p-stop implant and the channel width W , which denotes the distance of the bias dot implant to the cell implant (see figure 5.1b) and the circumference of the inner dot. When a bias voltage V_b is applied between the bias grid and the backplane, the potential of the strip implant should be kept close to bias grid potential, usually far below $\mathcal{O}(0.01V_b)$, otherwise it is difficult to reach full depletion before electrical breakdown.

The situation in the **PTP** resistor is similar to a field effect transistor in weak inversion. In the 1D case an analytic treatment of the effect is found in [61, 62] and [33, chap 7.8.1]. This npn(pnp)-sandwich structure can be

seen as two diodes in back to back configuration. Four different situations for the charge carrier concentration, electric field and potential are shown in figure 5.3.

For $V_b < V_{pt}$ the structure is high resistive. When a voltage is applied one of the diodes is forward biased, while the other is reverse biased. Therefore, with increasing voltage the depletion region of the reverse biased diode will grow. The punch through voltage at $V_b = V_{pt}$ is defined, where both space charge regions join. The flatband case, $V_b = V_{fb}$, is defined as $\frac{dV}{dx} = 0$ at one end of the junction, which corresponds to full depletion of the structure. In real structures full depletion of the sandwich may be reached by the built-in depletion region, without application of external bias.

Using the thermal voltage $V_T = kT/q$, the Debye length in a semiconductor is defined as

$$L_D = \frac{\epsilon kT}{q^2 N_{A/D}} = \frac{\epsilon V_T}{q N_{A/D}}. \quad (5.1)$$

The current voltage characteristic of the punch through effect for small currents (see [61]) is given by

$$I_{pt} = I_{p0} e^{\left(\frac{V_b - V_{pt}}{m V_T}\right)} \quad (5.2)$$

$$\text{with } I_{p0} = A \frac{q D_p n_i^2}{2\sqrt{\pi} L_D N_D}, \quad (5.3)$$

where I_{p0} is the current at $V_b = V_{pt}$ and m is the non ideality factor, which is mainly defined by the device parameters and can be written as

$$m = \frac{2W}{x_{j0} + x_j} \quad (5.4)$$

where W is the channel width, x_{j0} is the built-in length of the forward biased region and x_j is the distance of the maximum of the potential from the source, when a outer voltage is applied. The current is exponentially dependent on the barrier height and inversely proportional to the distance of the maximum from the source. Therefore with increasing channel width, the resistance of the structure in the high ohmic region increases.

As soon as the mobile charge carrier concentration is in the same order of magnitude than the doping concentration the electric field deviates from the linear case. For even higher voltages, the charge carrier velocity saturate at v_s and the space charge limited current is

$$I_{\text{scl}} = \frac{2A\epsilon v_s}{W^2} (V_b - V_{\text{fb}}), \quad (5.5)$$

where A is the area of the punch through device, $V_{\text{fb}} = qN_{\text{eff}}W^2/2\epsilon$. The common term used is “space charge limited” region [63]. This gives rise to the definition of a saturation resistance $R_{\text{sat}} = W^2/2A\epsilon v_s$.

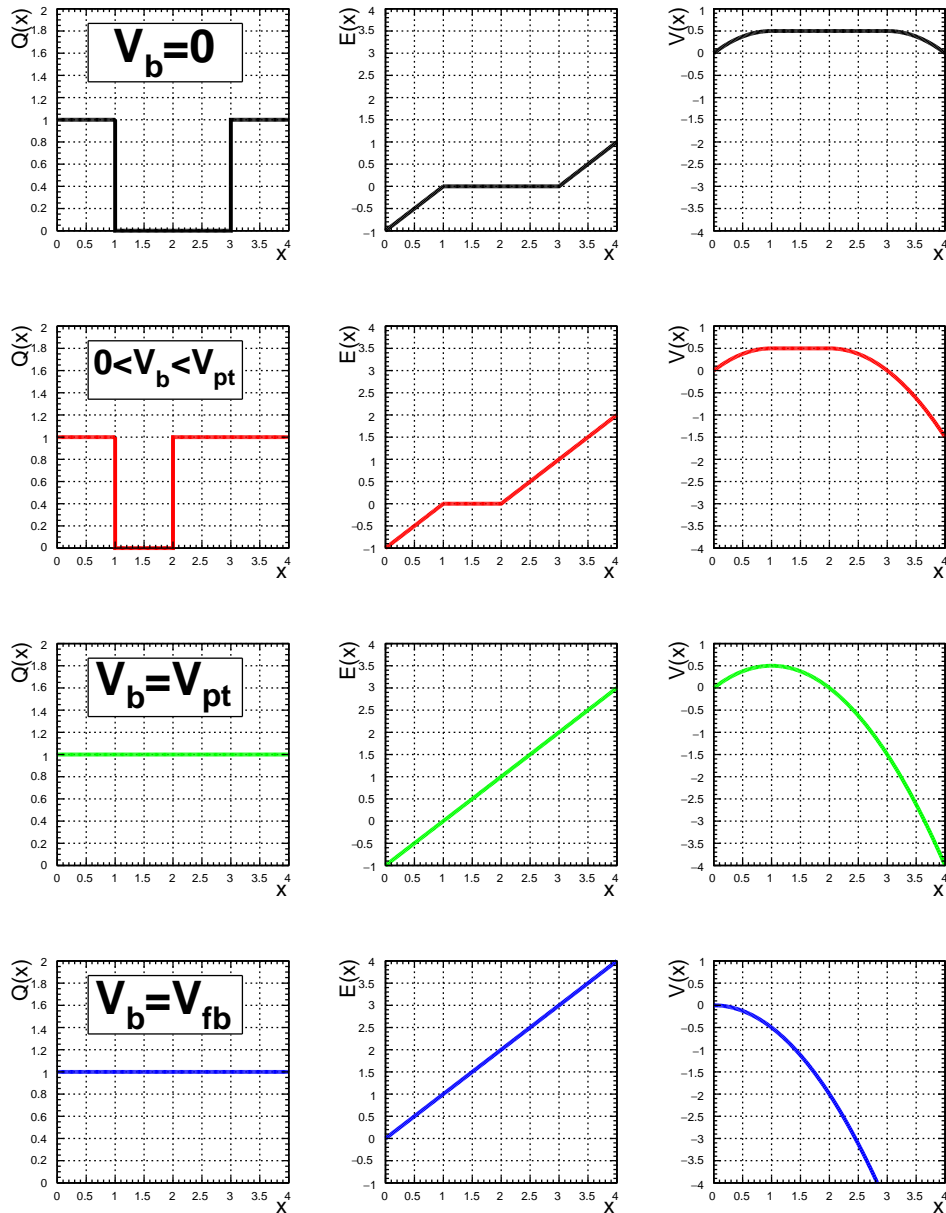


Figure 5.3: The punch through mechanism for a box charge concentration in the 1D case, when a bias voltage is applied. Left column shows the charge concentration depending on the x coordinate, the middle column the electric field, and the right column the electrostatic potential. Arbitrary units are used.

Chapter 6

CMS Tracker Detector phase II upgrade

The following is a short introduction to the measures, which are foreseen for the tracker upgrade, in order to fulfill the requirements from section 2.5, with strong focus on the outer tracker. As shown in figure 6.2 the new device is divided in the **Inner Tracker (IT)** (green, yellow), with silicon pixel modules with high spatial resolution for good vertex reconstruction, and **OT** (red,blue) with modules of silicon strip sensors. These special p_T -modules (see section 6.1) allow discrimination of the transverse momentum at bunch crossing rate and send data to the Level-1 Trigger. Due to the expected increased Level-1 Trigger rate of 750 kHz with a specified maximum trigger latency of 12.5 μ s binary readout is foreseen.

In order to include the tracking information in the Level-1 Trigger decision, a part of the data reduction is realized in the p_T -modules, which are capable to perform p_T -discrimination at around 2 GeV.

The p_T -discrimination is based on the bending of the particle tracks in the magnetic field of the solenoid. The p_T -modules therefore combine two closely spaced silicon sensors and the corresponding intelligent readout chip incorporates the correlation and discrimination logic. The strip direction is chosen parallel to the z-axis in the barrel and radial in the endcaps.

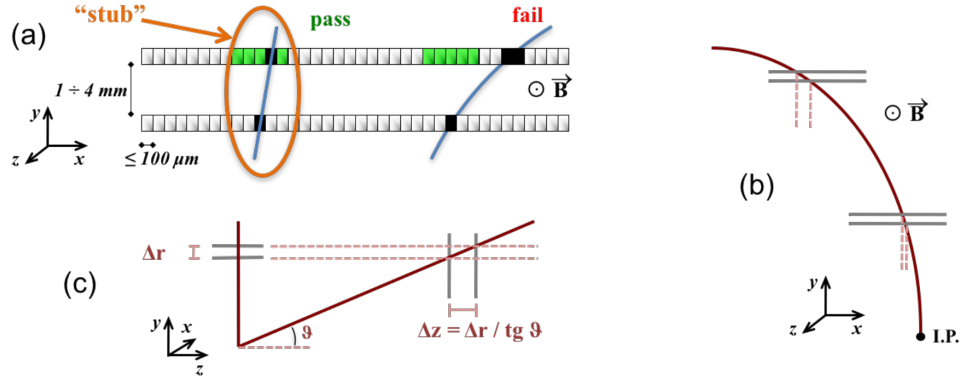


Figure 6.1: (a) Shows the principle of p_T -discrimination. A coincidence of two hits in closely spaced sensors is accepted, if inside the programmable correlation window (green). (b) For fixed sensor distance the distance in x of the hits forming a stub increases with distance from the interaction point (I.P.). (c) In order to have a homogeneous discriminating power in all tracker partitions, a set of sensor spacings is foreseen. E.g. for the same discriminating power a larger spacing is necessary in the endcaps. The picture is taken from [7, p. 24].

Stiff tracks of high p_T particles produce hits in both sensors inside an adjustable correlation window as shown in figure 6.1. The distance of the sensors, the programmable width of the correlation window and the programmable offset of the correlation window are optimized, such that a homogeneous p_T -threshold is achieved in the whole tracker volume. For particles exceeding the p_T -threshold so called stubs are produced and transmitted to the **L1** track finder at bunch crossing frequency. It is possible to exploit the stub principle down to a minimum radius of 200 mm from the interaction point in the 3.8 T magnetic field for a strip pitch of $100 \mu\text{m}$.

The **L1** track finder is designed to accept around 15 000 stubs from particles with $p_T > 2 \text{ GeV}$ per bunch crossing and reconstructs **L1**-tracks with a maximum latency of $5 \mu\text{s}$. The track finding process comprises data organization, pattern recognition, track fitting, and duplicate removal. The coarse tracks are then used in the **L1** trigger decision.

The tracker is divided in barrel and endcap regions. Different types of modules, as presented in detail in section 6.1, are foreseen. This accounts for the necessity of higher granularity due to the expected track density in the in-

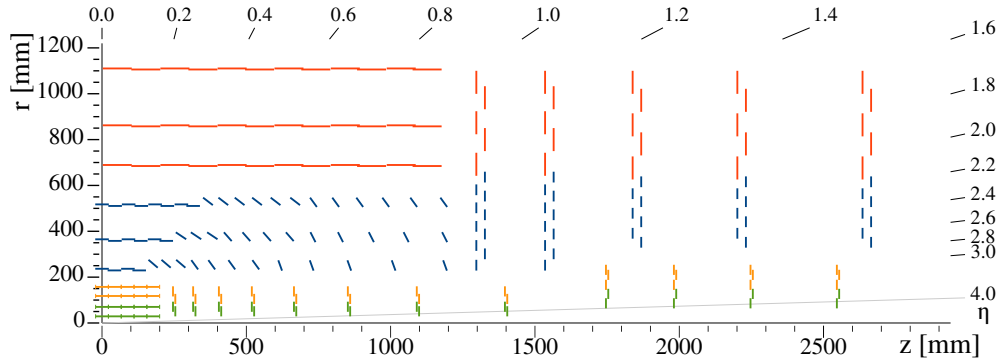


Figure 6.2: The layout of the upgraded tracker. PS-modules are shown in blue, 2S-modules are shown in red, pixel modules in green and yellow. A part of PS-modules in the barrel region is tilted. The picture is taken from [7, p. 22].

ner region of the tracker. A part of the modules in the inner region are tilted with respect to the z -axis. This improves the stub efficiency for particles with large incidence angle. The strip sensors are readout from both ends and the strip is segmented in two halves. However the readout chips do not communicate between the two halves and stubs are formed only, if the z -coordinate of the two hits is in the same halve of the module. In a flat layout, with strip direction always parallel to z in the barrel region, this leads to geometrical inefficiency of larger than 30% [7, p. 25]. Tilting a part of the modules as shown in figure 6.2 in the barrel region strongly reduces the effect.

6.1 Module Design

For the upgrade two different types of modules are foreseen in the **OT** region. The 7680 **2-Strip Modules (2S Modules)** cover the outer regions. For this module strip sensors with $90\ \mu\text{m}$ pitch and 5 cm long strips are used. Each of these strip sensors comprises 1016 strips, split in two halves and readout at the edges. For the **2S Module** 1.8 mm and 4.0 mm sensor spacing is foreseen. In this work the focus is on the **Pixel-Strip Module (PS Module)**, which is used in the inner region, where high granularity is required in order to keep the occupancy at the desired target level.

6.1.1 The PS Module

The **PS Module**, shown in figures 6.3a and 6.3b, combines the **PS pixel (PS-p)** macro-pixel sensor with $100\ \mu\text{m}$ pitch and approximately 1.5 mm long cells and the **PS strip (PS-s)** sensor with $100\ \mu\text{m}$ pitch and 2.4 cm long strips. The **PS-p** sensor has 32 rows in 960 columns.

In total 5616 **Pixel Strip (PS)** modules are foreseen in sensor spacings of 1.6 mm, 2.6 mm and 4.0 mm. The correct distance is achieved with an **Aluminum-Carbon Fiber (Al-CF)** precision spacer, with low thermal expansion coefficient and high thermal conductivity. The **Carbon Fiber Reinforced Polymer (CFRP)** material has a high thermal conductivity and is used as stiffener for the flex-hybrid and as base plate. The important factors for heat production are the **Macro Pixel ASIC (MPA)**, **Short Strip ASIC (SSA)** and the sensors, with 85 % heat production from the chips. A front-end hybrid carries the **SSA** readout chips and the **Concentrator Integrated Circuit (CIC)** chip, which aggregates the data and distributes clock, trigger and control signals. The **PS-s** sensor is directly connected to the hybrid via wire bonding technique, avoiding the use of a pitch adapter and extra material. The complementary part with the **MPA** and **PS-p** sensor is called **Macro-Pixel-Sub-Assembly Block (MaPSA)**.

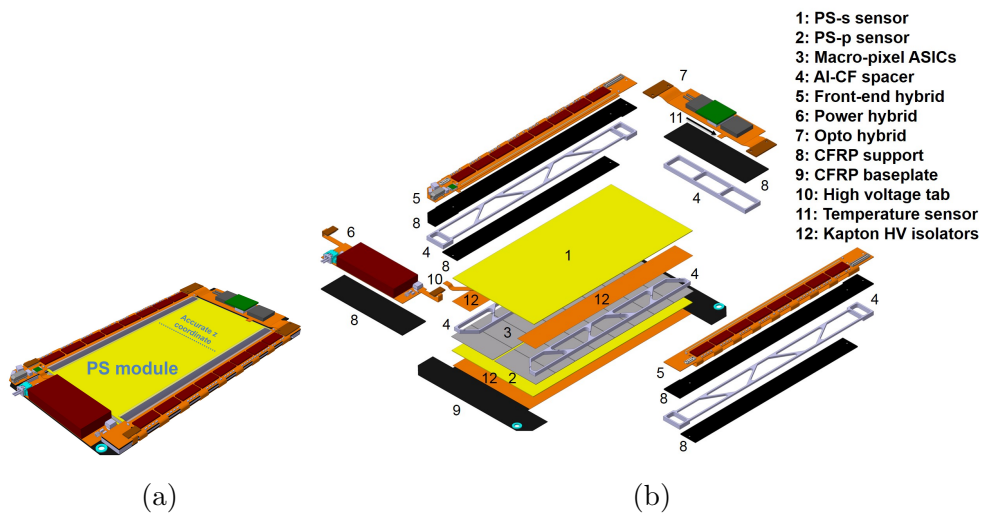


Figure 6.3: (a-b) The mechanical view of the **PS Module** from [7, chap. 3.1.2].

In addition two service hybrids provide auxiliary electronics for powering and optical readout.

6.1.2 The Macro-Pixel-Sub-Assembly Block

The **MaPSA** is the bump bonded assembly of 2 x 8 **MPAs** and one **PS-p** sensor. The assembly is build with technology for a hybrid pixel detector as shown in figure 6.4. Due to the variety of applied connection techniques and the tight constraints for clearance, which are required for HV-stability, the production of the **MaPSA** and complete assembly of the module is challenging. For mass production the C4 process for bump bonding is used. The bump bonding is necessary, because due to the high number of readout channels the signals cannot be routed to the periphery independently and on-chip data reduction is necessary to minimize the amount of connections to the outside [53, chap. 1]. Typically the amount of charge collected on the electrode is very small and therefore the **CSA** should be placed as close as possible to the sensing electrode.

Baseline Design

One option is to connect the **Front-End hybrid (FE hybrid)** to the **MPA** via wire bonding technique. In the following this is referred to as baseline design (see figures 6.5a and 6.6a).

In this case the **MPAs** are located between the silicon sensors of the module. This implies a proper isolation of the high voltage of up to 800 V [7, chap. 3.3.3], which is applied on the backplane of the **PS-p** sensor, from the **MPA** front side. Hazardous sparks potentially occur in the region of the sensor edge to the passivated front side of the **MPA** and in the wire bonds. The distance of 80 μm of sensor and readout chip is constrained by the bump bonding technique. The dielectric strength of air is $3 \text{ V } \mu\text{m}^{-1}$ and therefore not sufficient to protect from sparking. In addition considering the dielectric strength of silicon dioxide of $1 \times 10^3 \text{ V } \mu\text{m}^{-1}$ and a typical passivation

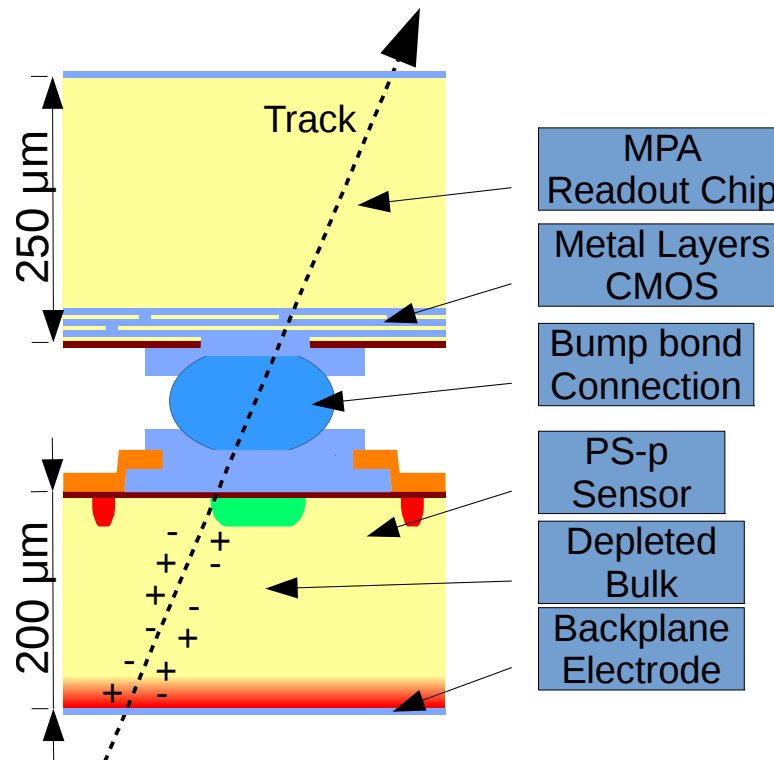


Figure 6.4: A cut, not to scale, through the hybrid pixel cell shows the connection of **MPA** readout chip and silicon sensor with a bump bond. In the baseline design of the module an additional high resistive underfill is placed in the voids between sensor and chip as spark protection. The foreseen distance of sensor and chip is $80\ \mu\text{m}$ [7, chap. 9.2.2.5].

layer thickness of $500\ \text{nm}$ on the sensor, the design constraint is not reached without special measures.

In history for hybrid-pixel detectors therefore two sided processing was preferred, which confines the high voltage to the back plane of the sensor via an additional guard-ring on the back plane [53, p. 11]. However double sided processing is expensive for mass production and consequently in the baseline design a high resistive underfill with sufficient dielectric strength is foreseen [7, chap 9.2.2.5]. The wire bonds are protected with wire bond encapsulation technique from sparking and from vibrations, which occur in the magnetic field. The **MPA** to **PS-p** sensor overhang is therefore also constrained by the clearance of the wire bonds pads and wire bonding machine.

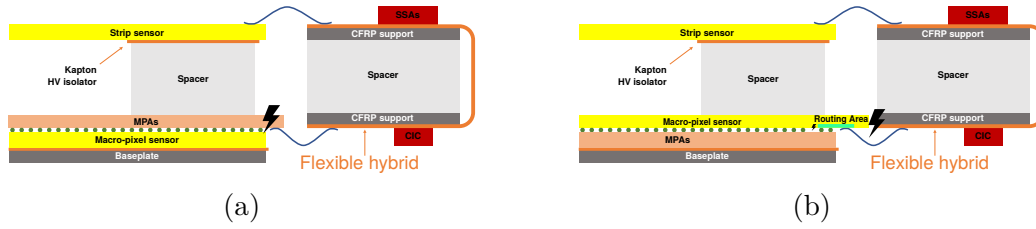


Figure 6.5: Side view of the **PS** module for the baseline concept (a) from [7, chap. 3.1.2] and the inverted concept (b). The olive circles represent the bump bond connections. A high resistive underfill avoids possible sparking (lightning symbol) in the edge region in (a). The critical region for sparks in (b) is near the wire bonds.

The surface area of the **PS** sensor is used to remove the heat produced by sensor leakage current and readout chip through a **CFRP** base plate covering the full sensor area exploiting the thermal conductance of the bump-bonds.

Inverted Design

In the following paragraph a different option to connect the **MPA** to the **FE hybrid** is introduced. In this concept, which is referred to as **Inverted MaPSA (Inverted MaPSA)**, the **MPA** digital IO and low voltage connections are fed through a dedicated routing area on the sensor (figures 6.5b and 6.6b) and wire bonding connects **FE hybrid** and routing area (see figure 6.7a). In this case the natural choice is to flip the assembly, such that the backplanes of **PS-p** and **PS-s** sensors face each other.

Direct cooling of the **MPAs** is possible. The absence of additional scattering material, which may affect the stub measurement quality due to **MCS**, between the two sensors is beneficial. A smaller distance of sensor to readout chip can be chosen, which reduces the cost of the bump bonding process and in general facilitates the utilization of a variety of compatible readout chips, which have certain requirements for the bump bonding process.

In this concept the critical points for possible sparking are the transition region in between the guard rings from sensor area to routing area and the clearance of the wire bonds to the edge of the sensor. For sufficient clearance, the geometry of the bond loop has to be considered for the design of sensor

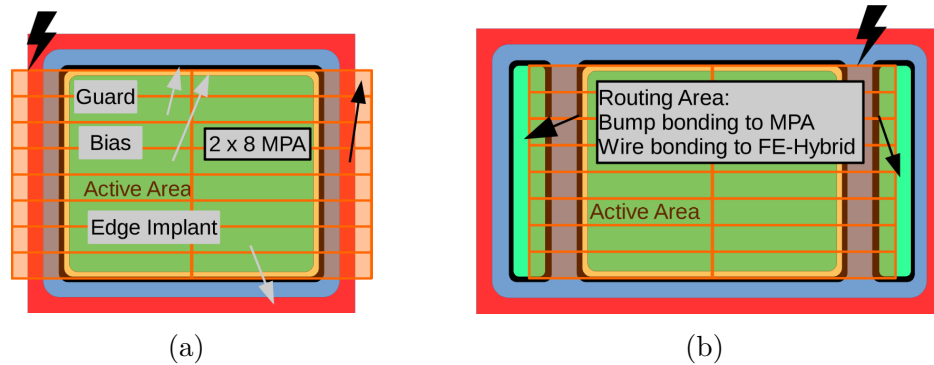


Figure 6.6: (a) A simplified sketch (Top view) of the **MaPSA** in the baseline design. The p-type edge implant in red is at backplane potential. The potential drops from bias ring (yellow) to edge ring. A floating guard ring (black) improves HV-stability and field homogeneity at the edge of the active region. 2 x 8 **MPA** chips are bump bonded to the sensor in the final version. (b) In the inverted concept a routing area connects the **MPA** to the **FE hybrid**. Active area and routing have separate guard rings. The lightning symbol indicates critical regions for sparking in (a,b).

and **FE hybrid**. The underfill process step can be omitted, which reduces costs and complexity.

A possible improvement of the currently available inverted sensor prototype design may be a common guard ring for routing area and active sensor area, which isolates the chip-sensor interface completely from backplane voltage and could improve the HV-stability.

One possible drawback of the design is the additional material for the routing area foreseen on the silicon sensor. Here the crucial figure is the ratio of the line density of the chip IO to the number of rows read out by the chip. This figure strongly depends on online data reduction capability of the chip. The impact of the additional ineffective area is smaller for sensors with high number of rows.

Routing area signal transmission

The signals induced by a **MIP** in the sensor are $\mathcal{O}(1 \times 10^6)$ times smaller than the digital IO signals for the **MPA**. The principle of the routing area

exploits the microstrip transmission line for the single ended signals and a coupled microstrip transmission line for differential signals. The microstrip consists of a metal strip on top of a layer of silicon dioxide. The ground plane is given by grounded n-implanted region, which ensures good capacitive decoupling from backplane implant and sensitive volume of the sensor (see figure 6.7a).

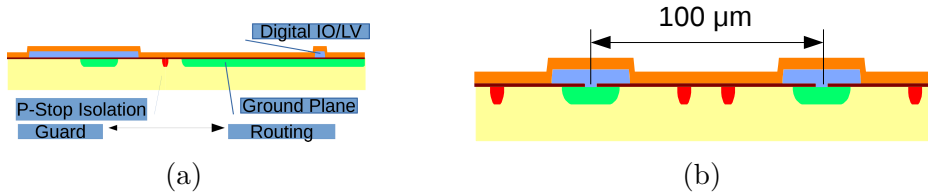


Figure 6.7: A cut through the wafer. P-stop implant red, strip implant green, metal light blue, thin dielectric brown, passivation oxide orange. (a) shows the edge of the routing area with guard ring and one signal trace. The implant below is kept at 0 V (ground plane). (b) shows two macro pixel cells with p-stop isolation in between. Strip implant and metal strip is connected.

The 320 MHz system clock, which is needed for the chip, is realized as differential pair in **Current Mode Logic (CML)**, which provides good common mode noise rejection. For the inverted concept the always active system clock is a possible additional source of correlated noise phenomena, due to remaining capacitive coupling to the active volume via the backplane. Therefore the isolation of the routing area is crucial for the inverted module concept.

6.2 Readout Electronics

6.2.1 Noise in silicon detectors

In the following the relevant relevant quantities regarding electronic noise of a silicon detector with **CSA** and multichannel readout are introduced according to [64, chap. 3.3.2].

The single channel noise of a silicon detector is characterized by the achieved **Equivalent Noise Charge (ENC)**, which is the total integrated **Root**

Mean Square (RMS) noise of the analog front end system in units of elementary charge depending on the peaking time of the signal t_p , a bias resistor R_{bias} , the feedback resistor R_f , the input capacitance C_T , the feedback capacitance C_F and the leakage current I_1 as shown in figure 6.8. In a DC-coupled sensor the cells are directly biased via the readout chip and the contribution of a bias resistor is omitted.

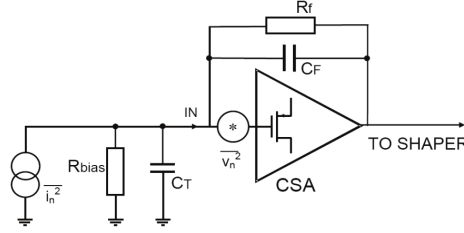


Figure 6.8: Noise in a charge sensitive amplifier from [64, chap. 3.3.2].

$$\text{ENC}_{\text{CSA}}^2 = \text{ENC}_i^2 + \text{ENC}_w^2 + \text{ENC}_f^2, \quad (6.1)$$

The main contributions for the **ENC** in silicon detectors with a **CSA** (CR-RC shaper for simplicity) as given in equation (6.1) of a single readout channel according to [64, chap. 3.3.2] are:

- Parallel noise ENC_i^2
- Voltage thermal noise ENC_w^2
- Flicker noise ENC_f^2

Using the capacitance and resistance as shown in figure 6.8 equation (6.1) reads

$$\begin{aligned} \text{ENC}_{\text{CSA}}^2 &= 0.924t_p \times a + 0.924 \frac{(C_F + C_T)^2}{t_p} \times b \\ &+ 3.695(C_F + C_T)^2 \times A_F, \end{aligned} \quad (6.2)$$

where $a = 2qI_1 + \frac{4kT}{R_{\text{bias}}} + \frac{4kT}{R_f}$. b and A_f are constants constrained by the parameters of the input transistor. The dominant terms for a DC-coupled

silicon strip sensor are the total input capacitance C_T and the leakage current I_L , which gives a shot-noise contribution. Typically pixel sensors have a lower input capacitance than strip sensors and therefore this results in a lower **ENC** in comparison with a strip sensor.

In a high energy physics experiment the peaking time t_p is usually short, in order to achieve high rate capability. Therefore the total input capacitance is the dominant term for **ENC**. However the radiation damage induced rise of the leakage current increases the ENC_i term, during the operation of the sensor, which leads to degradation of the detector performance.

6.2.2 Multichannel readout and threshold dispersion

In a multichannel readout chip the random variations in the production of the detector, due to component mismatch causes channel-to-channel variation in the detector response. For the input MOS transistors these variations are mainly due to statistical fluctuations of channel dopant density, oxide thickness, geometry, interface charges and oxide charges [64, chap 4.3]. In addition from the sensor side statistical dispersion of input capacitance and geometrical variations of the cell geometry, and cell leakage current I_{Strip} (e.g. see table 6.1) contribute [53].

Often in modern readout systems comparators and discriminators are used in the signal processing chain. Equalization of the discriminator or of the comparator response is possible via the adjustment of a local trim. The local trim is applied either via a trimming **Digital To Analog Converter (DAC)** or via a correction voltage stored in a capacitor, which allows to achieve a much more precise trim of the channels, using only a single precision **DAC** to store the voltage in the capacitors. However in high energy physics the capacitor method is impracticable, due to radiation induced discharge of these capacitors and the required high refresh rate [64, chap. 3.6.1]. The aim of the trimming procedure is the equalization of the channel response, by reduction of threshold dispersion with the help of the local trim to a minimum.

6.2.3 MPA and SSA

The **MPA** and the **SSA** readout chips are used in the final version of the **PS Module**. The **MPA** is connected to the **PS-p** sensor, while the **SSA** interfaces to the **PS-s** sensor. The **MPA** contacts 120 rows in 16 columns, in total 1920 cells.

Both chips comprise an analog front-end and a sophisticated digital block. The chips are connected via printed circuits on the flexible front-end hybrid. The architecture of the digital readout for the **PS Module** is shown in figure 6.9. For both chips the data from the binary-readout stage is split into a fast trigger data path and the **L1** data path, where the real-time correlation is performed and finally the data is transmitted via **CIC** to the trigger system. The **SSA** sends the strip trigger data to form the stubs to the **MPA** and stores the L1 trigger data for the strips. The correlation and stub logic however is realized on the **MPA**. Approximately 80 % of the available bandwidth for data transmission is occupied by trigger data, which is provided to the **L1** system at bunch crossing frequency. Per module one **CIC** buffers, aggregates and formats the data generated by the readout chips and communicates with the back-end system.

The following is a short revision of the analog front end and digital logic of the **MPA**. The analog front end consists of a **CSA**, shaper and discriminator stage (see figure 6.10). A Krummenacher feedback [65] provides leakage current compensation up to 200 nA for the DC coupled pixel cells, which puts an upper limit on I_{Strip} before and after irradiation. A mutual 8-bit **Threshold DAC (THDAC)** sets the discriminator threshold voltage. A local 16-bit ripple counter increments on the falling edge of the discriminator output for both analog signal polarities. The counter is active, when the shutter signal is high.

The circuit components of the front end of the real **MPA**, which is produced in 65 nm low-power CMOS technology [66, chap 4.2], show variations in the electrical properties (see section 6.2.2). These effects lead to a statistical mismatch, which is compensated by a local 5-bit **Trimming DAC (TRIMDAC)** at the discriminator stage. A trimming procedure ensures a

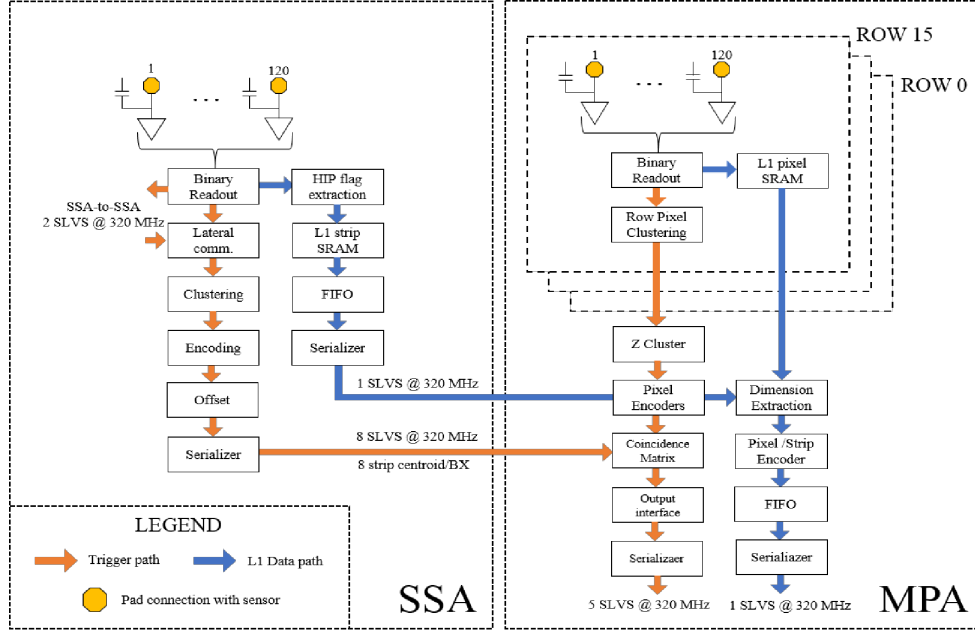


Figure 6.9: The data path for the **PS Module** from [7]. In the **L1** data path the zero-suppressed data is stored in a FIFO pipeline and transmitted to the back-end via a serializer, when the trigger signal arrives. The trigger path exploits real-time coincidence logic and data reduction steps in order to finally transmit the data to the **CIC** at bunch-crossing frequency.

homogeneous response across all channels and the quality of the trim directly, irrecoverably affects the stub production and data quality. Due to the binary readout less options for offline filtering and algorithmic data quality improvements exist.

Monte Carlo simulation has shown, that for the ideal **PS** modules only $\mathcal{O}(0.1)$ of the produced stubs correspond to a high p_T particle [66, p. 77]. Badly trimmed channels produce inefficiencies or extra noise, which generates additional combinatorial background in the stub logic and may propagate to the trigger system. Therefore the trimming procedure is essential to achieve good data quality.

The discriminator signal is fed to an edge detector, which detects the rising edge of the signal and accounts for a configurable signal polarity. A flip-flop (Sync FF) synchronizes pulses from the front end with 40 MHz.

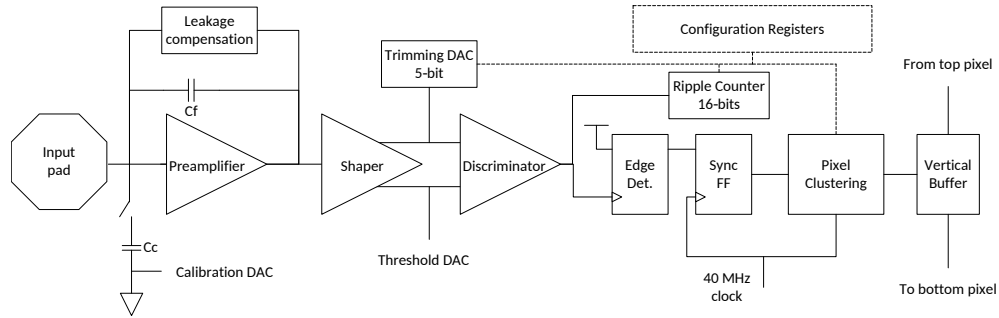


Figure 6.10: The pixel front end of the **MPA** from [66, p. 88].

In the trigger path the synchronized signals are then passed to the pixel clustering logic. The so called centroid [66, chap 4.61] is extracted in this step. In contrast to a geometric binary center of gravity clustering algorithm with floating point precision, this real time logic assigns the hit position in cell coordinates to the cell next to the periphery of the chip in case the cluster size is even. In case the cluster size is odd, all cluster positions are given in even cell coordinates. This algorithm takes into account that cells on the chip edges have the $200\ \mu\text{m}$ cell pitch. The guess to assign these towards periphery keeps the error low for clusters, when one of the periphery cells is involved, which is denoted as boundary effect error. For the offline reconstruction a half pixel flag [66, chap 4.6.3] reduces the loss of precision due to the sparsification.

Wide clusters exceeding a programmable threshold are discarded for the correlation logic, which works on already zero-suppressed data and generates the stubs, with the sparsified cluster data from the **SSA** at bunch crossing frequency. The logic is limited to transmit a maximum of 2 stubs per bunch crossing. For the precision of the stub measurement it is beneficial to have a constant pixel cell geometry. This is because in digital clustering and stub logic only simple corrections are applied for non regular cells. E.g. in the online stub logic, half-strip resolution is not exploited, and for even cluster size the cluster center is assigned to the pixels closer to the periphery, which accounts for the greater area of the edge pixels. However in the offline track reconstruction, this coarse estimate for the center of gravity, can be improved with different weighting factors, depending on the track incidence angle and depending, whether a cluster incorporates pixels with different geometries.

Two different data paths with fast high bandwidth data transmission are distinguished, a third data path is the asynchronous readout, which is designed for calibration purpose only.

The trigger data path contains the stub information which is constantly sent to the L1-Trigger if a stub is detected. In the L1-Trigger data path a radiation hard **Static Random-Access Memory (SRAM)** is used to store the binary raw data of the pixel matrix up to 12.8 μs until the **L1** signal is received. Upon the arrival of a trigger signal the raw data is compressed and the strip position and width of the hit is sent to the output.

For reduction of power consumption due to **SRAM** memory write operations, the so called memory gating technique is applied. This technique allows to limit write operations of the raw data from the pixel matrix on **SRAM** to the events, where one pixel is above threshold. According to [66, chap 4.8.2] this contributes to a significant portion of the chip power consumption and therefore noisy cells should be identified during a calibration procedure and masked during the normal chip operation.

6.3 Prototypes

In this section the prototypes of the **PS-p** sensor and the **MPA** chip and the laboratory DAQ system, which are relevant for this thesis are introduced.

The **PS-p light** is a small size prototype sensor with 288 cells in four different geometries, as given in table 6.1 and regular cell pitch $p_x = 100 \mu\text{m}$ in the sensitive direction. Cells of 200 μm width are necessary at the boundaries of the up to 6 **MPA-light (MPA-light)** readout chips, which is a lightweight prototype the full **MPA**. The standard length of the cells is 1446 μm and at the edges the cells have 1746 μm . The geometrical position of the different cell variants on the sensor is visible in figure 6.11, together with an arrow, which symbolizes the movement of a probe needle, which is used to contact the cells during electrical testing. The sensor has a bias grid and the cells are connected to the bias grid via a **PTP**. The unit cell of the sensor is shown with the nominal dimensions in figure 5.1a and the **PTP** in figure 5.1b.

Table 6.1: Cell types and geometry parameters for the PS-p-light prototype sensors.

| Type | p_x [μm] | p_y [μm] | A_{cell} [mm^2] | $2(p_x + p_y)/A_{\text{cell}}$ [mm^{-1}] |
|------|----------------------------|----------------------------|--|--|
| 1 | 100 | 1446 | 0.1446 | 21.38 |
| 2 | 100 | 1746 | 0.1746 | 21.14 |
| 3 | 200 | 1446 | 0.2892 | 11.38 |
| 4 | 200 | 1746 | 0.3492 | 11.14 |

In addition there is an inverted **PS-p light** sensor, which comprises the routing area to connect the chip to the back-end electronics. The ratio of active area to total area is found in table 6.2. However for a real size prototype the difference in the ratio $A_{\text{active}}/A_{\text{total}}$ is expected to improve, because the number of readout rows and columns by one chip will increase, while the digital IO and LV connections do not scale linearly with the number readout cells. Consequently in a possible future version of the inverted prototype the 4 staggered rows for the bump bonding could be possibly reduced to one, which results in a smaller routing area.

Furthermore standard sensors with different edge-implant geometries were produced.

Table 6.2: Comparison of the active area to total area ratio for inverted and standard prototype sensor design.

| PS-p light | Area | x [mm] | y [mm] | A_{active} [mm^2] | $A_{\text{active}}/A_{\text{total}}$ |
|------------|---------|-------------|-------------|--|--------------------------------------|
| standard | Active | 5.19 | 9.26 | 48.04 | 0.5064 |
| | Total | 7.86 | 12.07 | 94.86 | |
| inverted | Active | 5.19 | 9.26 | 48.04 | 0.3473 |
| | Routing | 5.46 | 2.34 | 12.75 | |
| | Total | 7.86 | 17.60 | 138.32 | |

The corresponding readout chip is the **MPA-light**, which is a reduced size demonstrator for the full **MPA**. The **MPA-light** implements from analog front-end to the digital data reduction steps, all features described in section 6.2.3. The chip connects to 48 cells in 16 columns and in 3 rows. Up

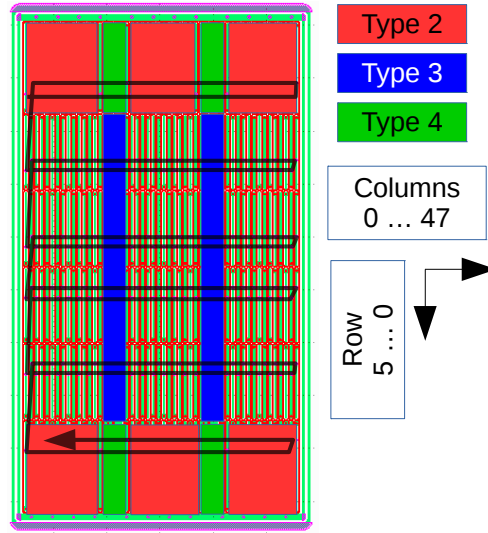


Figure 6.11: The different cell types with geometry parameters from table 6.1 are depicted on the PS-p light standard sensor. Type 1 refers to standard cell geometry and has no extra colored box. The black line indicates the needle movement during the electrical characterization. The column and row numbering scheme is introduced.

to 6 readout chips are connected to the sensor in 2 rows of 3. The configuration signals and the ripple counter signals are connected in daisy chain configuration and routed through all chips. For these signals an SPI-like protocol for data transmission is used. The simulated **Least Significant Bit (LSB)** values and full scale range of the **TRIMDAC**, **Calibration DAC (CALDAC)** and **THDAC** are given in table 6.3.

In contrast to the full **MPA**, which uses 320 MHz, the **MPA-light** runs on a 160 MHz system clock, which is realized as differential pair in **CML**. In the **MPA-light** the flip-flop, which is used to synchronize the pulses from the edge-detector to the 40 MHz clock, is reset with a 3.125 ns strobe signal every clock cycle. This introduces a detector dead time. For future versions, the strobe signal is replaced, by a logic, which resets the flip-flop only, if a signal was detected, which reduces the dead time to a minimum. In the **MPA-light** prototype different zero suppression modes are available for testing purpose covering all data reduction steps of the **L1**-data path. However in this work no zero-suppression was used, which is called no-processing mode.

Table 6.3: MPA-light specifications from simulation.

| Symbol | Definition | Nominal Value | |
|----------------------------------|-----------------------------|------------------------|-------------------------|
| | | [mV fC ⁻¹] | [V e ⁻¹] |
| G | Gain | 85 | 1.36×10^5 |
| | | [mV] | [e] |
| $E_{\text{FSR}}(\text{THDAC})$ | Full scale range THDAC | 0 to 370 | 0 to 27.2×10^3 |
| $E_{\text{FSR}}(\text{TRIMDAC})$ | Full scale range TRIMDAC | 0 to 120 | 0 to 8.81×10^3 |
| $E_{\text{FSR}}(\text{CALDAC})$ | Full scale range CALDAC | 0 to 450 | 0 to 33.0×10^3 |
| | Discriminator offset spread | 90 | 6.6×10^3 |
| Q_{THDAC} | LSB THDAC | 1.456 | 107.0 |
| Q_{TRIMDAC} | LSB TRIMDAC | 3.750 | 275.4 |
| Q_{CALDAC} | LSB CALDAC | 1.768 | 130.1 |

The hybrid **MaPSA**-light assemblies are connected with gold stud bump bonding (see figure 6.4), which is a low cost high density interconnect technology [67] and suitable for small scale prototype production.

The laboratory test system, which was used for data acquisition, features a mother-board, which comprises electronics for low voltage powering of the readout chip, level converters and buffer ICs. The assembly is glued and wire bonded to a dedicated daughter board. Two different versions of this daughter boards were designed during the work in this thesis. Due to the low-cost PCB technology only a maximum of 2 **MPAs** can be readout simultaneously. The mother-board is connected to the **Gigabit Link Interface Board (GLIB)** [68–71], which features an **Field Programmable Gate Array (FPGA)** and memory, which is used to buffer the **MPA** data before transmission to a **Data Acquisition (DAQ)** PC using the IP-Bus protocol. The **GLIB** board interfaces to a FMC-Card, which allows to connect an external clock, a trigger signal and a busy signal.

Chapter 7

Characterization of PS-p-light sensor prototypes

Several variants of the **PS-p light** sensor prototypes were produced and characterized within the scope of this thesis. The production of a new set of photo-lithographic masks is expensive. Therefore different small sensor geometries are placed on the same wafer. In addition process parameters are varied and their impact on the sensor performance is studied. In the case of the **PS-p light** prototypes four different variants as presented in table 7.1 were produced.

Table 7.1: Sensor variants for the **PS-p light** prototypes and their target process parameters. Only measured wafers are presented.

| Variant | Isolation | (Batch Wafer) | p-stop/p-spray | | Nom. Thickness [μm] |
|---------|-----------|---------------|------------------------------------|----------------------------|-------------------------------------|
| | | | Peak Conc. [cm^{-3}] | Depth [μm] | |
| 1 | | (1 11),(5 02) | 1×10^{16} | 1.5 | |
| 2 | p-stop | (1 17),(5 13) | 1×10^{16} | 2.5 | 200 |
| 3 | | (1 20),(5 15) | 1×10^{17} | 2.5 | |
| 4 | p-spray | (6 1) | 2×10^{15} | 0.5 | 200 |

The different variants allow to study the impact of p-stop depth and p-stop doping concentration. For n-strips in p-bulk material sensors the p-

stop ensures significant strip isolation in the unirradiated sensor. During irradiation of the sensor, however oxide charges build up in the silicon dioxide silicon interface, which have a similar effect on strip isolation. Both buildup of oxide charges and radiation damage in the silicon bulk lead to increasing electrical fields at constant bias voltage, while the increase in V_{FD} is caused by bulk damage only. In case of p-stop strip isolation the concentration and depth should be as low as possible before irradiation under the condition, that the strips show good isolation. Sensors with high initial p-stop concentration configurations show higher electric fields after irradiation in simulation. In a silicon detector this causes microdischarges, which produce non-Gaussian noise [72–74].

7.1 Static global characterization

IV Characteristic

For the ideal p-n junction, with no recombination and generation of currents in the depletion region, the volume current is given by the Shockley diode equation [15, p. 298],

$$I = I_S(e^{eV_b/kT} - 1), \quad (7.1)$$

where V_b is the externally applied voltage and

$$I_S = eA \left(\frac{D_n n_{po}}{L_n} + \frac{D_p p_{no}}{L_p} \right) \quad (7.2)$$

$$\approx eA \left(\frac{D_n n_i^2}{L_n N_A} + \frac{D_p n_i^2}{L_p N_D} \right), \quad (7.3)$$

where A is the cross sectional area of the junction, L_n/p the characteristic diffusion length for electrons and holes and the diffusion constants were introduced in equation (4.17).

In a silicon sensor, the leakage current I_L has a volume and surface contribution. The volume contribution is generated by thermally generated **EHPs** from the Shockley-Read-Hall process swept out of the depletion region and

the current is proportional to the depleted volume $V = A \cdot W$ and it holds [52, p. 13],

$$I_L^{gen} = eV \frac{n_i}{2\tau}, \quad (7.4)$$

where τ is the mean carrier lifetime, which is a quality parameter of the bulk material. The volume current of a diode shows a $T^{(3+\gamma/2)}e^{-E_G/2kT}$ dependency [31, p. 95], where γ is a constant factor.

Deviations from the ideal behavior occur due to generation and recombination of carriers in the depletion layer due to thermionic emission, a parasitic $I \times R$ drop due to series resistance, tunnel effect and surface effects, and avalanche generation. A more general treatment for the volume current accounts for thermionic emission and **SRH**-processes, which gives an additional current contribution

$$I_L \propto T^2 e^{-(E_G+\Delta)/2kT}, \quad (7.5)$$

where Δ is the difference of energy of the deep level defect to the Fermi energy [75]. Using

$$E_G = E_{G,0} - \frac{\alpha T^2}{\beta + T}, \quad (7.6)$$

[31, p. 16], where $E_{G,0} = 1.169$ eV, $\alpha = 4.9 \times 10^{-4}$ eV K⁻¹ and $\beta = 655$ K for equation (7.5) it holds,

$$I_L \propto T^2 e^{-E_{eff}/2kT} \quad (7.7)$$

and $E_{eff} \approx E_0 + 2\Delta$.

The reverse IV characteristic of a silicon sensor can be divided in different regions namely underdepletion, overdepletion and breakdown.

In the underdepleted case the current depends on $\sqrt{V_b}$, which is due to the volume term from equation (7.4). For $V_{FD} < V_b < V_{bd}$ the ideal volume current is given by equation (7.1). For a fully depleted bulk, the current saturates and is mainly dominated by the sum of saturation current I_S and the contribution from **SRH**.

The point, where avalanche generation becomes relevant, is called breakdown. However a large number of different definitions is found, how to extract the breakdown voltage from a IV-curve. In this work the ionization integral is

used for the extraction of V_{bd} from the simulation results. Above the breakdown voltage V_{bd} there is a steep increase in current, which eventually leads to thermal runaway. Furthermore so called microdischarge, which corresponds to localized avalanche breakdown, deteriorates the noise spectrum of the sensor. Design optimization of a silicon strip sensor aims to maximize V_{bd} , while the other parameters like charge collection efficiency and inter-strip capacitance stay in the region of their target value.

The measurements shown in this section for global characterization of the sensors, were conducted by applying a negative voltage to the backplane of the samples. A needle puts the bias ring to ground. All IV-measurements were performed under laboratory conditions and in dry atmosphere (RH < 20 %) in a dark box with a Keithley 237 SMU for bias voltage, unless stated otherwise.

1/ C^2V -Characteristic

In order to operate a silicon strip sensor fully efficient, all charges, which are produced by incoming particles, should be collected at the readout strips. This is only achieved, when the silicon bulk is fully depleted with $V_b > V_{FD}$. The capacitance voltage characteristic of an ideal diode depends on the depth of the depletion region, which is linearly dependent on the applied reverse voltage (see section 4.4.2). For the second partial derivative of it holds [33, p. 50]

$$\frac{\partial^2 C^{-2}}{\partial V^2} \begin{cases} \frac{2}{qN_{bulk}\epsilon\epsilon_0} & \forall 0 < V < V_{fd}, \\ 0 & \forall V_{fd} < V, \end{cases} \quad (7.8)$$

where $C = C'/A$ the capacitance per unit area. Consequently, the bulk doping concentration N_{bulk} is obtained from the slope

$$N_{bulk} = \frac{2}{q\epsilon\epsilon_0 \frac{\partial C^{-2}}{\partial V}}. \quad (7.9)$$

The capacitance at $V_b = V_{fd}$ is proportional to $A\epsilon\epsilon_0/W$ and approximately constant, unless avalanche occurs. The scaled $C^{-2}V$ curves from TCAD simulation of the **PTP** are shown superimposed to the measured $C^{-2}V$ for

variant 1 and 2 in figure 7.1. For the simulated curves for very low p-stop peak doping concentrations of $1 \times 10^{15} \text{ cm}^{-3}$ and low implant depth of $0.5 \mu\text{m}$ the diodes are not sufficiently isolated, which results in greater full depletion capacitance and lower V_{fd} . The variation of p-stop depth has a small effect on V_{fd} , while $C(V_b = V_{fd})$ is not affected. Increasing p-stop depth at constant p-stop peak concentration affects the slope and V_{fd} .

For the measured curves from figures 7.4a and 7.4b the depletion voltage was extracted via the intersection of fits of two linear functions. The bulk doping concentration was approximated by assuming an effective area of 0.4804 cm^2 and extracted from the slope of the linear fit. The results are shown in table 7.2. Variant 1 and 4 form a group with lower full depletion voltage with respect to variant 2 and 3. Despite their equal physical thickness of $(200 \pm 4) \mu\text{m}$ a significant difference in V_{fd} was observed.

Table 7.2: The full depletion voltages extracted from the the intersection of a fit of two linear functions to the $C^{-2}V$ -characteristics and the estimate of the bulk doping concentration extracted using equation (7.9) under the assumption of an area of $A_{eff} = 0.48 \text{ cm}^2$. The values are mean and standard deviation with statistic of 5 sensors per wafer.

| Variant | (Batch Wafer) | V_{fd} [V] | N_{bulk} [cm^{-3}] |
|---------|---------------|------------------|------------------------------------|
| 1 | (5 02) | 40.84 ± 1.51 | $2.59 \pm 0.52 \times 10^{12}$ |
| 2 | (5 13) | 75.60 ± 3.82 | $2.40 \pm 0.57 \times 10^{12}$ |
| 3 | (5 15) | 80.37 ± 1.76 | $8.71 \pm 0.23 \times 10^{11}$ |
| 4 | (6 01) | 42.35 ± 3.64 | $2.73 \pm 0.94 \times 10^{12}$ |

For the inverted PS-p light sensors the curves in figure 7.4b have higher end capacitance with respect to the standard geometry. This may partially be attributed to the punch through biasing of the routing area, which enlarges the depleted volume and increases the total sensor capacitance.

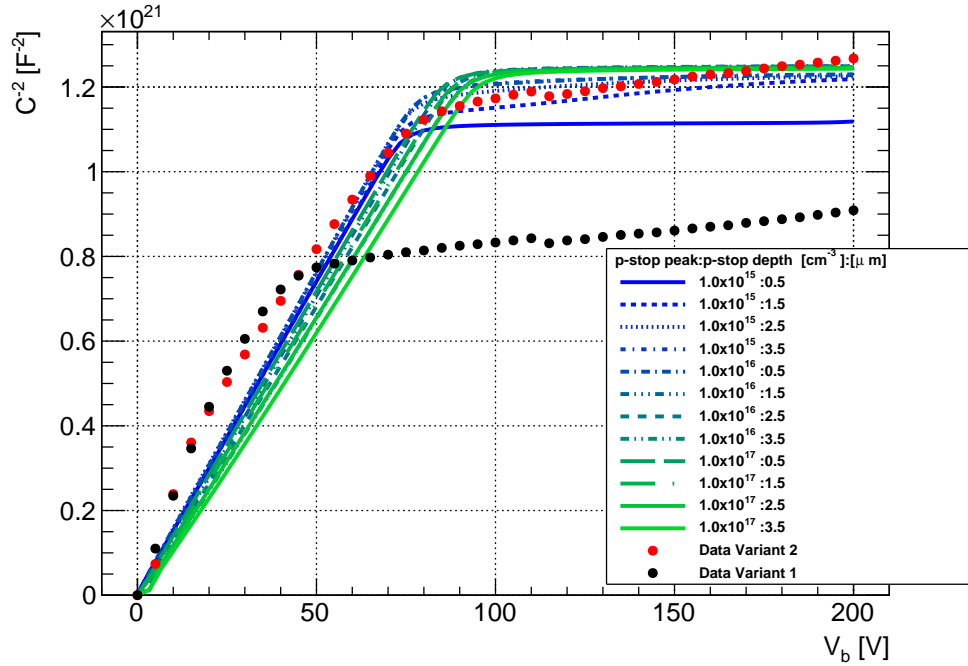


Figure 7.1: The $1/C^2V$ characteristic for samples of variant 1 and 2 with the standard geometry and scaled simulated curves for different p-stop concentrations and p-stop depth, for the nominal **PTP** geometry and nominal conditions.

7.1.1 Results of p-spray and p-stop strip isolation techniques

Figure 7.2a show the IV characteristics for the four variants in the standard geometry. Clearly in the pre-breakdown region variants two and three form a group and variants one and four form a group. This is probably due to a difference in the bulk material. The hypothesis is, that this the base material is from distinct single crystals, which come with different impurity concentration and this affects the lifetime of thermally generated **EHPs**.

Due to the logarithmic scale the onset of microdischarge and deviation from the ideal IV-behavior is emphasized. This is visible as sudden increase in the order of magnitudes in leakage current [76, 77]. In general different forms of breakdown are found in the data. Breakdown may be caused by single faulty strips and the additional current caused by the strip is limited by the **PTP**,

which is called soft or ohmic breakdown. If the avalanche generation is localized in the **PTP** itself or in the periphery of the sensor, the current increase is more pronounced and steeper, due to the lack of a limiting series resistance. Both effects result in a clear deviation from the ideal diode characteristic in saturation region, which has a linear form in the semi-logarithmic scale. In case both electrons and holes gain enough energy in between two collisions to generate additional **EHPs** avalanche develops, which is seen as sudden increase in orders of magnitude in the leakage current.

For variant three early breakdown occurs for all standard, inverted and edge geometries (see figures 7.2a, 7.2b and 7.3c), which indicates a general problem of the design with high p-stop peak concentration and deep p-stop implantation. Variant one and two achieve the best HV-stability, where one sample has a breakdown voltage above 650 V for variant two. Comparing samples with early breakdown from the same variant, optical inspection with a microscope indicated problems with irregular **PTP** structures. Mainly three effects were identified. Firstly mask misalignment breaks the effect of protective metal overhang, which should overlap the bias dot implant. The second effect are shorts between the metal lines of bias grid and the strip metal. The third problem identified were scratches on the surface of the sensor. A scratch in the strip region does not necessarily lead to a defective sensor in terms of increased current. However if visible scratches affected one single **PTP** the sensor shows higher current. This irregularities also heavily impact single-strip currents (see section 7.6).

Figure 7.2b shows the leakage currents for the inverted geometry. As expected additional current from the routing area, which is biased via punch-through mechanism, leads to a slightly higher leakage current. In the assembly breakdown voltage may improve, when both routing area n-implants are contacted as well. A steeper increase of the current, with respect to the standard geometry, is found in the breakdown region. This is related to the floating routing area implant during the one needle contact measurement and improves, when routing area and strip strip implants are biased, when the readout chip is connected.

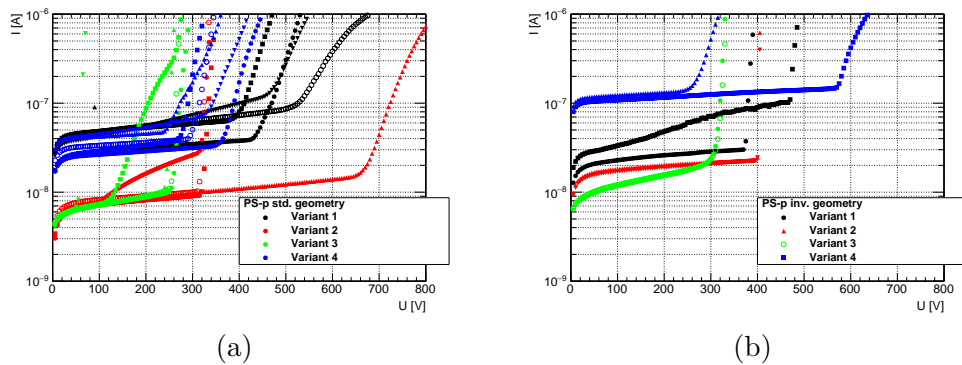


Figure 7.2: The IV characteristic for variant 1, 2, 3 and 4 with the standard geometry in (a). The inverted geometry was measured contacting the bias ring of the sensor active area only (b)

7.1.2 Edge implant geometry studies

Microscopic cracks induced by the sawing process provide extra generation and recombination centers in the forbidden band gap [52, p. 34]. In case they spatially coincide with a high field region, additional currents are generated. In order to avoid extra current due to the sawing process, an edge implant (see figure 6.6a) is used. In the current sensor design in the unirradiated case, the edge implant causes the backplane potential to drop on the surface of the sensor from the edge implant to the bias ring implant. The additional guard ring smooths the potential drop. In the following the possibility of improvements of the sensor edge implant geometry is explored.

A general recommendation for the width of the edge implant is to use three times the wafer thickness between the cutting edge and the sensitive region of a silicon sensor [53, p. 95]. However this is only a rule of thumb, which relies on the fact, that the lateral spread of the depletion region depends on $\sqrt{V_b}$. If the defects introduced by the sawing process do not reach into the depletion region, this assumption is valid. However the edge ring should be as thin as possible due to the additional dead material in the tracking detector, which lowers the ratio of active to total area of the sensor.

Sensors with three different widths of the edge implant (350 μm , 500 μm and 850 μm) are discussed in the following.

Comparisons of the IV characteristics for edge geometries in figures 7.3a to 7.3d must take into account the p-stop variations from table 7.1 and therefore only samples from the same wafer are compared. Due to reasons stated in section 7.1.1 variant three is not considered, because of early breakdown found in all sensors. It is expected, that in case the edge implant geometry is wide enough the minor effects are seen in the IV characteristic. When the width of the edge implant is too small, this should have a negative impact on HV-stability. For variant one in Figure 7.3a however both 500 μm sensors have a soft breakdown, which is attributed to irregular **PTPs** as seen in figures 7.19b and 7.19c. For variant one and two a slight trend is visible to prefer 850 μm over 350 μm . However the statistic of good samples is low. For variant four, which has the p-spray isolation no clear trend is observed.

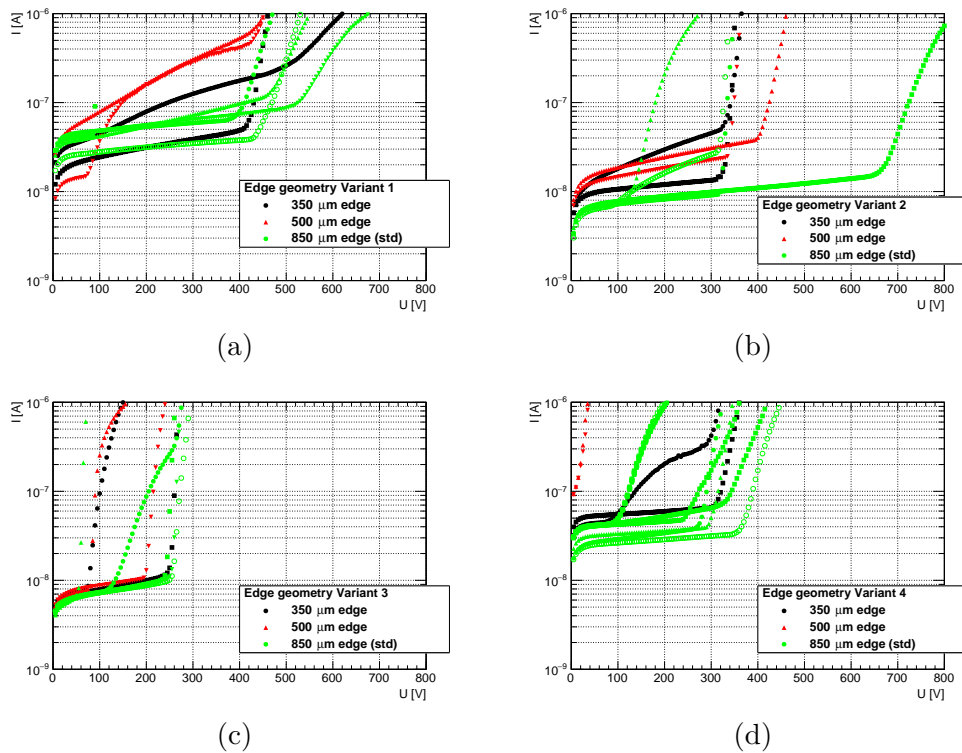


Figure 7.3: The IV characteristic for variant 1, 2, 3 and 4 in (a,b,c,d)

In figures 7.3a to 7.3d for the 350 μm and 500 μm geometries two samples are shown, for the 850 μm standard geometry five.

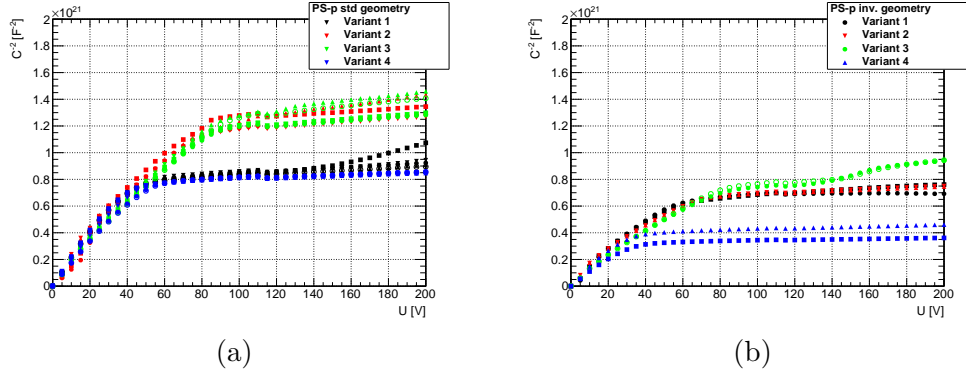


Figure 7.4: The $1/C^2V$ characteristic for variant 1, 2, 3 and 4 with the standard geometry in (a). The inverted geometry was measured contacting the bias ring of the sensor active area only (b)

7.2 Measurement of effective energy

The measurement of the $(\ln I) - (1/kT)$ characteristic of an overdepleted sensor allows to distinguish surface currents and eventual charge multiplication effects from **SRH** generated ideal volume currents, as given in section 7.1.

The currents of sensors from variant 1, 2 and 3 were recorded at $V_b = 130$ V during a period of ca. 3 days with the sensors inside a climate chamber under slow variation of temperatures, in order to keep the sensors in thermal equilibrium with the surrounding air. In this period the sensors undergo three full temperature cycles from 15°C to 65°C under constant humidity, as shown in figure 7.6. The results shown in figure 7.5 are well described by equation (7.7), which suggest a volume current dominated behavior for variant 1 and 2. The effective energies with the parametrization from equation (7.7) are found in table 7.3. The presented errors from the fit are underestimated, due to the limited accuracy of the temperature measurement, which relies on the temperature sensor of the climate chamber. The sensing element has no physical contact to the sensor surface, but measures the temperature of surrounding air at the exhaust of the climate chamber. However the measured values for E_{eff} for variant 2 sensors are comparable to the reported values from [75].

The deviation of variant 3 samples from the expected linear behavior may be explained by additional charge carrier multiplication due to impact ioniza-

tion, which is highly temperature dependent. This is probable, because bias voltage was closer to the measured breakdown voltage at 20 °C for variant 3 sensors during the test and multiplication effects may be relevant well before breakdown voltage [78]. With increasing temperature, the breakdown voltage increases with reported temperature coefficients of $\mathcal{O}(50 \text{ mV K}^{-1})$ [79]. This is the observed behavior for variant 3 sensors, which show significant deviation from the model only at lower temperatures or higher values of $1/k_B T$, where breakdown voltage is lower than the measured breakdown voltage at room temperature and therefore the $V_{bd} - V_b$ is smaller and avalanche multiplication causes the measured current to deviate from theoretical prediction. Due to the non negligible impact ionization effects for non irradiated sensors the application of the effective energy model is questionable for variant 3 sensors.

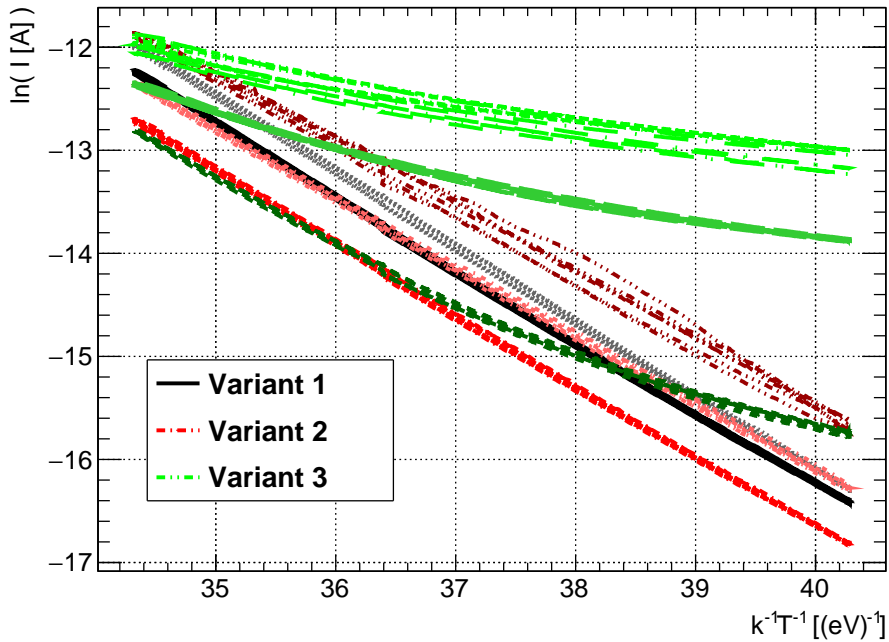


Figure 7.5: The logarithm of the sensor currents vs $1/kT$ for in total 8 samples from variant 1, 2 and 3. Sensors from the variant 1, 2 and 3 are shown in different gray, red and green colors.

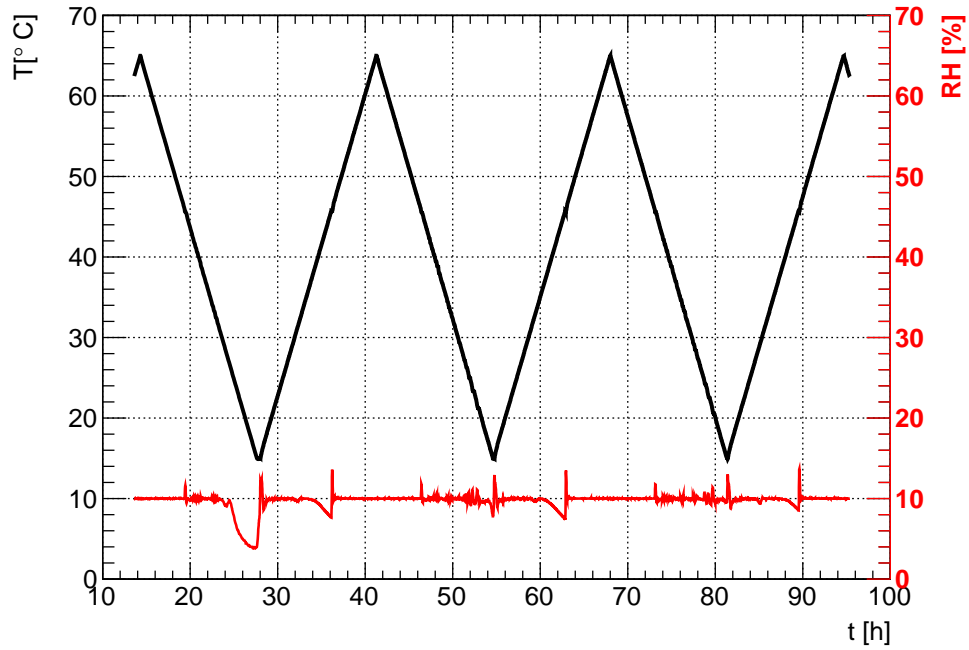


Figure 7.6: The temperature and humidity during the recording of the Arrhenius curves from figure 7.5. A low temperature ramp rate is necessary to keep the sensors in thermal equilibrium with the surrounding environment. A constant low relative humidity reduces effects due to varying surface current contribution.

Table 7.3: Effective energies and errors at $V_b = 130$ V from the fit with the temperature dependent dark current model. Note that the values for variant 3 sensors are not comparable due to insufficiencies in the used model.

| Variant | (Batch Wafer) | Sensor | E_{eff} [eV] |
|---------|---------------|--------|---------------------|
| 1 | (1 11) | 9 | 1.3048 \pm 0.0005 |
| 1 | (1 11) | 11 | 1.3473 \pm 0.0005 |
| 2 | (1 17) | 8 | 1.2146 \pm 0.0005 |
| 2 | (1 17) | 9 | 1.2824 \pm 0.0005 |
| 2 | (1 17) | 11 | 1.171 \pm 0.001 |
| 3 | (1 20) | 8 | 0.907 \pm 0.002 |
| 3 | (1 20) | 9 | 0.241 \pm 0.001 |
| 3 | (1 20) | 10 | 0.404 \pm 0.001 |

7.3 Measurements on test structures

The **Metal Oxide Semiconductor (MOS)** structure [31, chap. 3] is formed by a layer of insulating material in between a semiconductor and a metal layer. In the following the metal contact is called gate, while the semiconductor layer is called body. A **MOS** test structure allows to determine the V_{fb} , oxide charge concentration N_{ox} and t_{ox} .

When a voltage is applied between gate and body three different situations occur. Accumulation refers to majority carriers (holes for p-type silicon) to accumulate at the gate electrode, when a negative voltage is applied at the gate, if the applied voltage is smaller than the flatband voltage. The capacitance of the device is defined by the thickness of the oxide, which acts as dielectric for a plate capacitor, formed by the accumulation layer and the gate electrode.

The flat-band condition is reached, when the energy band diagram is flat. In this case the fixed oxide charges are compensated by the applied voltage $V = V_{fb}$.

Depletion regime is reached by further increasing the voltage to $V > V_{fb}$. The majority carriers are repelled from the surface and a depletion region builds up below the oxide with the effect of an decreasing capacitance.

The thickness of the oxide t_{ox} is given by the capacitance in the accumulation regime

$$t_{ox} = \epsilon_0 \epsilon_r \frac{A}{C_{acc}}, \quad (7.10)$$

where A is the area of the gate electrode.

The intersection of two linear fits of the capacitance measured in the accumulation regime and the capacitance in the depletion regime the flat-band voltage V_{fb} is determined. With the metal-semiconductor work function difference $\phi_{ms} = \phi_m - \phi_s$ the fixed-oxide charge concentration is obtained

$$N_{ox} = \frac{C_{acc}(\phi_{ms} - V_{fb})}{qA} . \quad (7.11)$$

The **MOS** test-structure is used to control the process parameters, which are not easily accessible in a direct measurement on a sensor. The design of the test-structure from the prototype wafer is shown in figure 7.7. The measurement of the capacitance is realized applying a small 250 mV AC signal for different low frequencies, performing a sweep of the the gate voltage at fixed backplane potential with a Agilent E4980A LCR meter. The measurement results for the different variants are shown in figures 7.8a to 7.8d.

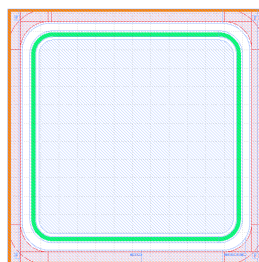


Figure 7.7: The test structure design of the 7 mm \times 7 mm MOS.

Table 7.4: The flat-band voltage and oxide charge concentration calculated with the measured bulk doping concentration and the effective gate area of 0.2809 cm^{-2} at 22°C . The model does not apply for the p-spray variant.

| Variant | (Batch Wafer) | V_{fb} [V] | N_{ox} [cm^{-2}] |
|---------|---------------|------------------------|---|
| 1 | (5 1) | -4.4 | 3.54×10^{11} |
| 2 | (5 12) | -3.08 | 2.98×10^{11} |
| 3 | (5 15) | -23.5 | 2.00×10^{12} |

The parameters shown in table 7.4 are extracted at 1 kHz using equation (7.11). The measured oxide-charge concentration and flat-band voltage for the samples is remarkably high compared to non-irradiated sensors from other vendors. In addition for variant 3 a strong frequency dependence is observed, which may be caused by a rectifying Schottky contact at the backplane. However a low initial oxide charge concentration is beneficial for the sensor quality for reasons explained in section 7.7. For variant 4 the p-spray implantation is applied on the whole wafer and the measured curves therefore have a different behaviour.

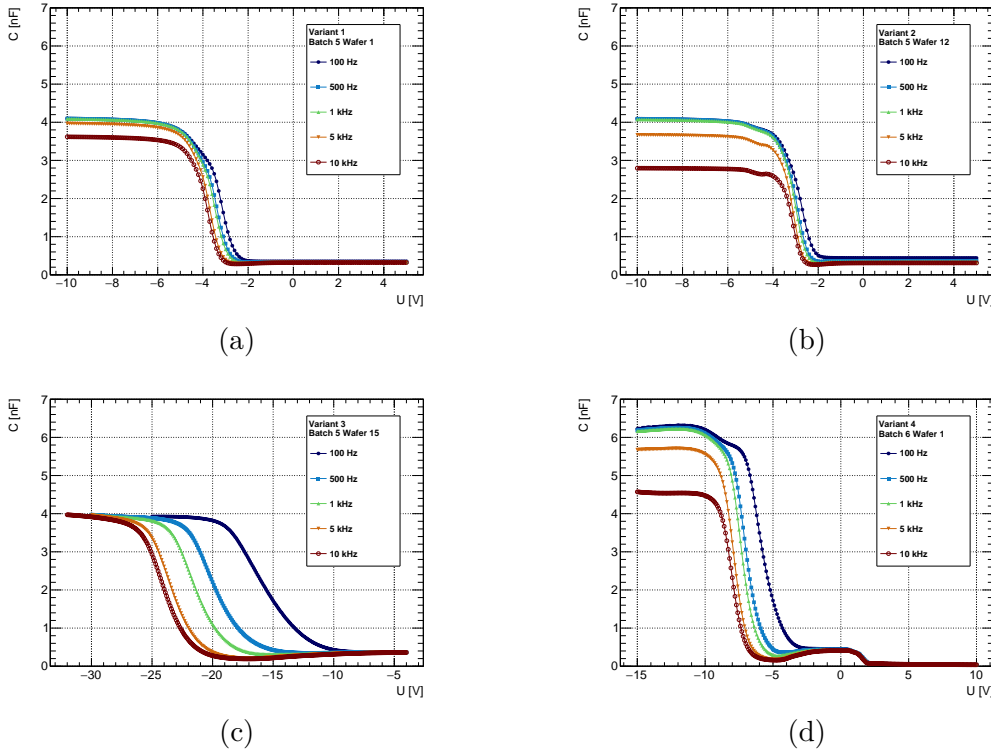


Figure 7.8: The capacitance of the P-MOS structure for a sweep of the gate voltage. From negative to positive gate voltages three different regimes, accumulation, depletion and inversion are visible.

7.4 Characterization of the PTP-structure

The theoretical treatment of the **PTP** is found in section 5.4. For the manual measurement of an IV characteristic on the **PTP** a voltage is applied between the DC-pad of a pixel and the bias ring at ground potential with a Keithley K237, while the backplane HV potential is defined with an additional Keithley 2410 **Source Measure Unit (SMU)**. The important parameter during the normal operation of the sensor is the differential resistance of the structure, when the source, which corresponds to the bias dot implant, is at the potential of the cell implant. In the space charge limited region the differential resistance is characterized. For a sample of variant 1, the influence of the backplane voltage on the characteristic of the structure presented in figures 7.9a and 7.9b. With decreasing backplane potential down to 150 V,

V_{th} decreases and the curves are slightly shifted. For increasing voltage drop across the structure the differential resistance drops to $\mathcal{O}(500 \text{ k}\Omega)$. For currents of $10 \mu\text{A}$ the resistor was thermally destroyed, due to self-heating. When the sensor is biased via the bias grid, the voltage drop across the structure adjusts to the current of the strip implant. Automated measurements and comparison of the different p-stop variants are found in section 7.5.

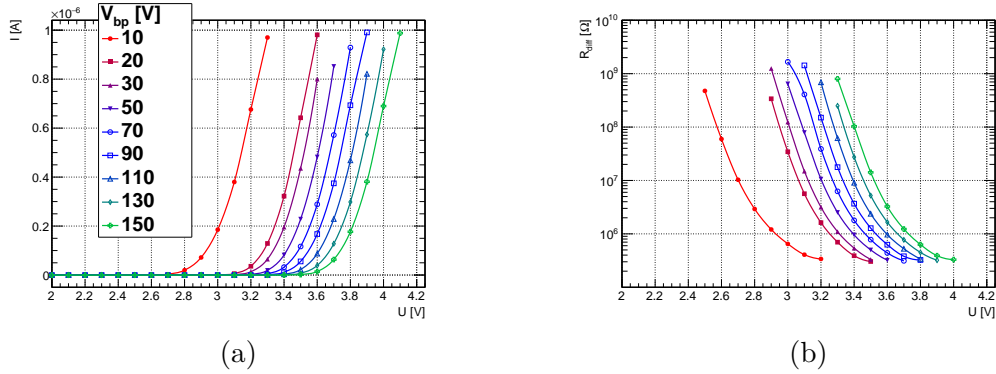


Figure 7.9: The IV characteristic of the **PTP** resistor for different backplane voltages V_{bp} in (a) and the differential resistance in (b). Zero potential is at bias ring, while a constant negative bias V_{bp} is applied to the backplane. A negative voltage sweep is conducted on the DC-pad with a second SMU.

7.5 TCAD Simulation of the PTP-structure and macro-pixel cell

In order to understand the characteristic of the **PTP** structure and the macro-pixel cell, regarding avalanche breakdown, simulations were conducted via Synopsys **TCAD** [80]. The simulation produces a solution of the continuity equations equation (4.25) coupled with the Poisson equation for the stationary case ($\frac{dn}{dt} = 0$) on a two-dimensional mesh. For the **PTP**-resistor, cylinder coordinates are used, unless stated otherwise. A set of nominal input parameters for the simulation is defined in table 7.5. The effect of small variations on one parameter, while all other parameters stay at the nominal values is shown in the following sections.

Table 7.5: The nominal input parameters and mesh parameters for the simulation.

| | Value | Unit | Type |
|--|-----------------------|------------------|------------|
| Geometrical Parameters | | | |
| Metal Overhang (MO) implant head | 5 | μm | |
| MO implant strip | 4.5 | μm | |
| MO bias dot PTP | 2.5 | μm | |
| Distance n-implants cell-bias dot | 18 | μm | |
| Distance n-implants strip | 75 | μm | |
| Width p-stop implant | 4 | μm | |
| Oxide thickness | 0.25 | μm | |
| Doping Profile Parameter | | | |
| Bulk doping conc. | 1.00×10^{12} | cm^{-3} | Boron |
| N-implant conc. | 1.00×10^{19} | cm^{-3} | Phosphorus |
| N-implant depth | 2 | μm | |
| P-stop max. doping conc. | 8.00×10^{15} | cm^{-3} | Boron |
| P-stop depth | 1.5 | μm | |
| Backplane implant conc. | 5.00×10^{18} | cm^{-3} | Boron |
| Backplane implant depth | 1 | μm | |
| Interface Parameter | | | |
| Oxide charge density Si-SiO ₂ | 1.00×10^{11} | cm^{-2} | |
| Mesh Parameters | | | |
| Mesh Elements Strip | 3.89×10^5 | | |
| Mesh Elements PTP | 2.85×10^5 | | |

In figure 7.10a the density of free electrons for a backplane voltage of -300 V is shown. The varied parameters are: Thickness of SiO₂ layer, the p-stop width, the p-stop peak concentration and the p-stop depth. The orange arrow indicates the electron accumulation layer at the Si-SiO₂ interface, which builds up due to the positive oxide charge density in the SiO₂. The sampled analytic doping profiles for n-strip implant, p-stop implant and backplane implant after meshing are shown in figure 7.10b.

The terminology used, regarding the interface charges is N for the net number of charges per unit area and at the Si-SiO₂ interface and Q for the net effective charge per unit area [81]. For the oxide charge density N_{ox} a value of $1 \times 10^{11} \text{ cm}^{-2}$ is assumed in the simulation [82, p. 94], which is an educated guess for unirradiated sensors. However it should be stated, that in the aforementioned study, samples from the same vendor, which produced the sensors characterized in the scope of this work, showed higher measured oxide charges.

N_{ox} is the sum of the contributions for mobile ionic charge N_m , fixed oxide charge N_f , oxide trapped charge N_{ot} and interface trapped charge N_{it}

[83, chap. 3.1.3,3.3.1]. N_{ox} leads to a electron accumulation layer directly under the surface, which is interrupted by the p-stop. Therefore the surface channel is blocked in the **PTP** and currents are generated via the punch through mechanism, when a voltage is applied between source and drain (see figure 7.10a).

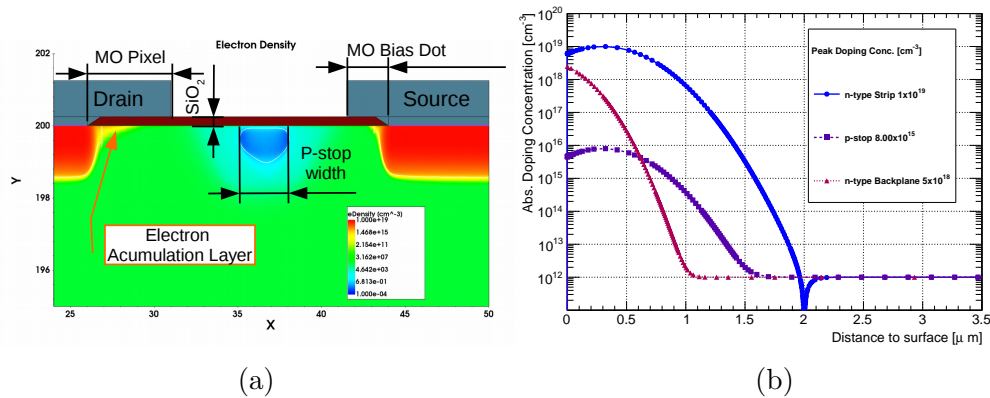


Figure 7.10: (a) The density of free electrons at backplane voltage of 300 V. X/Y axis in μm . Source refers to the bias grid contact and drain to the pixel. The cylinder rotation axis is at $50 \mu\text{m}$. (b) The absolute value of the nominal doping concentration. A cut through the cell implant, p-stop region and backplane is shown. The dots represent the sampling points of the analytic Gaussian and Error function profiles after the mesh is created.

Breakdown voltage simulation

The experiment requires sensors with $V_{bd} > 700 \text{ V}$ before irradiation [7, p. 143] and for the tested samples the requirements are not met (see section 7.1). This specifications are based on the requirement to be able to collect sufficient signal, when design fluence of $1 \times 10^{15} \text{ n}_{eq} \text{ cm}^{-2}$ is reached. The results of the optical inspection of the samples showed some irregularities in the **PTP** structure as shown in figures 7.19a to 7.19c, which motivates studies of the robustness of the design of the **PTP**. The most important finding in the optical inspection, which affects all **PTP** structures on the wafer is the mask misalignment, which possible leads to complete loss of the protective metal overhang of the inner bias dot implant and this deteriorates the HV-stability. The breakdown voltage of the device was simulated with

a ramp of the backplane electrode to negative potential, keeping the strip implant and bias dot implant at ground potential. The ionization integral from equation (4.45) for electrons and holes for the nominal conditions is shown in figure 7.11b and the breakdown voltage V_{bd} is extracted by interpolation using the avalanche condition from equation (4.47). This procedure is justified for $N_{ox} = 1 \times 10^{11}$, where different other extraction methods for the breakdown voltage show similar results [83, chap. 4.6.2]. In the simulation the van Overstraeten de Man impact ionization model [84] is used together with drift and diffusion.

For a one sided abrupt junction the critical electric field [31, p. 107] is expressed as

$$E_{bd} = \frac{4 \times 10^5}{1 - 1/3 \log_{10} \left(\frac{N}{1 \times 10^{16} \text{ cm}^{-3}} \right)} \text{Vcm}^{-1}, \quad (7.12)$$

which results in $E_{bd}(N = 1 \times 10^{12} \text{ cm}^{-3}) = 1.71 \times 10^5 \text{ Vcm}^{-1}$ for the nominal simulation parameters, which is lower than the value for intrinsic silicon $E_{bd}(\text{Si}) = 3 \times 10^5 \text{ Vcm}^{-1}$.

The electrical field for the **PTP** structure with nominal parameters at -300 V backplane voltage is shown in figure 7.11a. High electric fields, which may cause breakdown occur below the edge of the metal overhang of the bias dot and at the edge of the implant of the bias dot. In the nominal configuration breakdown occurs at the edge of the junction. In general however this depends on oxide thickness, p-stop concentration, p-stop depth and metal overhang.

Problems in the fabrication of the **PTP** due to the small feature size, which eventually lead to early breakdown, could eventually be circumvented with a linear version of the **PTP**. This traditional design was used for strip sensors before, and is implemented with a n-implant below the metal bias line and regular pixel cells as presented in figure 7.11c, where no p-stops lines drawn. Such a design comes with the disadvantage of slightly lower geometrical efficiency, with respect to the round bias dot, but with the advantage of an improved HV-stability. The impact of the rounding radius on the ionization integral is shown in figure 7.11b along with the curve for the ionization in-

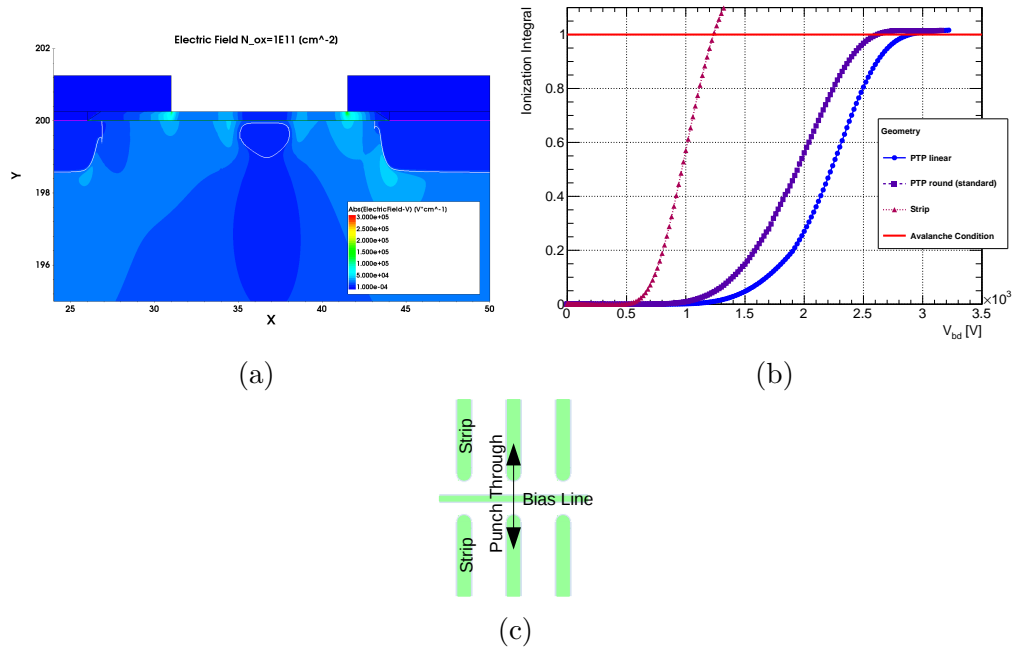


Figure 7.11: (a) The electric field in the **PTP** at -300 V backplane voltage peaks at the edge of the implant of the bias dot. A second point where the critical electric field E_{bd} is reached for some parameter configurations is below the edge of the metal overhang of the bias dot. (b) The ionization integral for a standard round **PTP**, a linear **PTP**, and the pixel geometry for nominal parameters. The top view for a traditional linear punch through geometry without p-stops is shown in (c)

tegral of the regular macro-pixel geometry. From figure 7.11b it is deduced, that V_{bd} of the strip is lower than for the **PTP** by design. This is related to the larger gap of the cell implants for the macro-pixel geometry, which leads to a stronger bending of the electrical field lines.

However the simulated breakdown voltage is greater than V_{bd} measured in figure 7.2a, which is partly explained by the one-needle measurement and the voltage drop across the **PTP** structures, which leads to additional inhomogeneity in the electrical field. In addition, the exact values of the simulated V_{bd} depend on the mesh density in the high field regions and usually a higher mesh density results in a higher simulated value for the breakdown voltage. A higher mesh density comes however with increased computing time and

therefore a trade-off is made. The mesh parameters are kept constant for all parameter sets, which ensures comparability among different geometries.

The extracted V_{bd} are shown in figures 7.12a to 7.12d. For increasing p-stop width, increasing p-stop depth and increasing p-stop peak concentration V_{bd} decreases. The simulated V_{bd} stays well above the design value before irradiation. Usually the HV-stability decreases with a greater distance of the n-implants. This is observed in the simulation, where the strip geometry has a lower breakdown voltage.

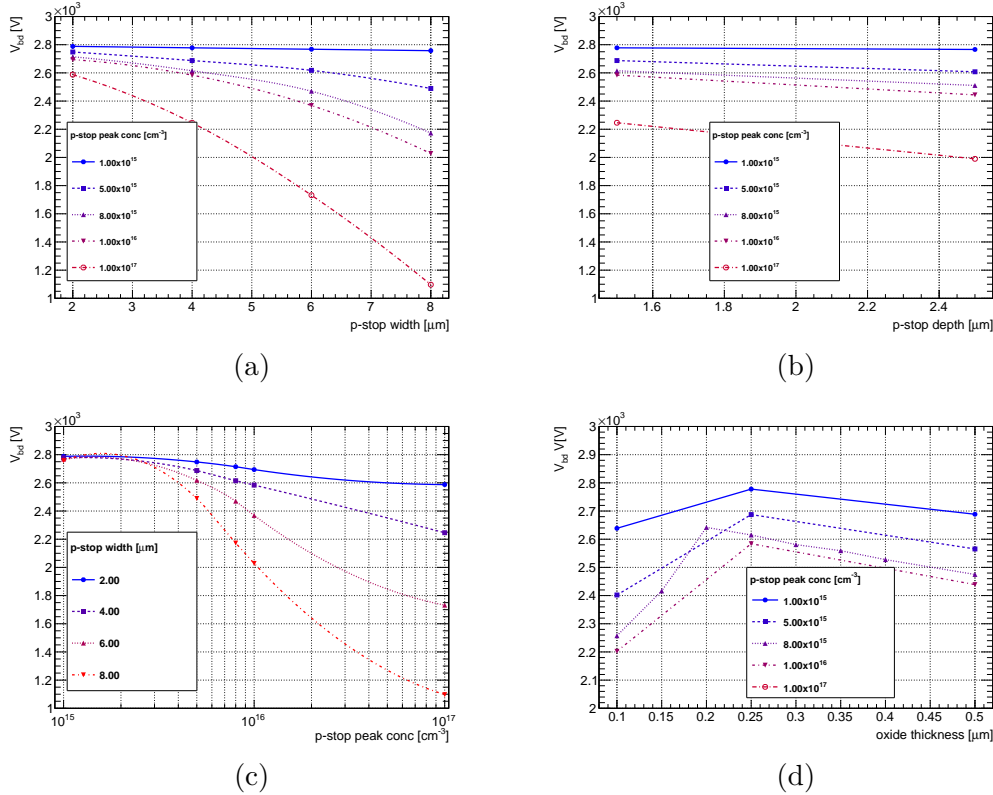


Figure 7.12: The extracted breakdown voltage V_{bd} depending on p-stop width (a), p-stop depth (b), p-stop concentration (c), and oxide thickness (d).

Simulations of the PTP device characteristic

The understanding of the **PTP** characteristic is important for the initial IV-testing of the sensors. Previous work ([48]) mainly targets the strip ge-

ometry and sensor periphery. The characteristic of the **PTP** when a voltage is applied between source and drain, while the sensor is fully depleted, has two different regions, which are described in section 5.4. For the simulations presented in the following a bias voltage of $V_b \approx 1.3V_{fd} = 130\text{ V}$ is applied at the backplane, which is similar to the applied voltage during testing of the sensors.

Nonetheless it is useful to define a threshold voltage V_{th} , different from V_{fb} , analog to the situation in a transistor. For a MOSFET a threshold voltage V_{th} can be extracted from $I_d V_G$ characteristic via different methods described in [85]. For the case of the **PTP** V_{th} is extracted from the $I_d V_{sd}$ characteristic, via

$$V_{th} = \text{Max} \left(\frac{d^2 I_d}{dV_{sd}^2} \frac{1}{I_d} \right), \quad (7.13)$$

which is shown in figure 7.13a. The used naming convention for the three terminal device is source for the bias dot implant and drain for the strip implant, I_d the total current measured at the strip implant contact, which includes the dark current of the bulk. For a sensor, which is biased by the **PTP** $V_{sd} > 0$. The threshold voltage separates the exponential off-state region from the region, with strong increasing currents and eventually space charge limited region. During testing, the strip current defines the potential of the strip implant, which adjusts close to the threshold voltage V_{th} , also for strips with higher currents.

In the off-state region a high differential resistance R_{diff} is required. In the standard mode of operation of the detector this R_{diff} contributes to the inter-macro-pixel resistance R_{int} and gives a small contribution from thermal noise $\propto \sqrt{\frac{kT}{R_{diff}}}$ in the readout electronics [52, p. 39], if no charge carrier multiplication is present.

The experiment requires a cell isolation of $R_{int} > 1\text{ G}\Omega\text{ cm}$ before irradiation [7, p. 143], which puts a lower limit for $R_{diff}(V_{ds} = 0\text{ V})$. This is due to the lower interstrip resistance found after irradiation, which possibly deteriorates the spacial resolution of the device. The isolation properties of the strip geometry were simulated and measured by [48, 73, 74, 86]. However the the geometry of the **PTP** needs additional studies.

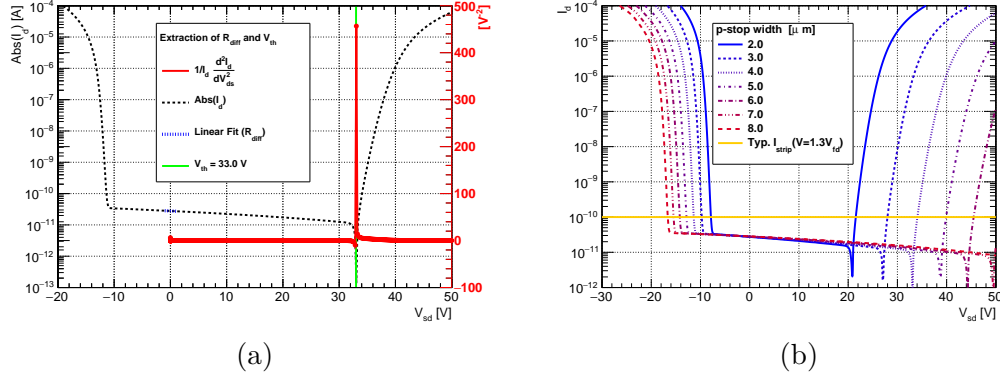


Figure 7.13: The extraction of V_{th} from the $I_d V_{sd}$ characteristic in (a). In (b) the absolute value of the drain current vs V_{sd} is shown. The effect of the p-stop width on V_{th} and R_{diff} is visible.

$R_{diff}(V_{sd} = 0 \text{ V})$ was extracted from simulation with a linear fit to the $I_d V_{sd}$ characteristic from -1 V to 1 V , where the linear approximation of the exponential is justified (see figure 7.13a). This extraction method properly accounts for the leakage current of the device.

The impact of p-stop width on V_{th} and R_{diff} is shown in figures 7.13b, 7.14a and 7.15a. A weak increase with p-stop width is found for R_{diff} for the nominal values, while V_{th} increases rapidly to values of more than $.5V_b$, which reduces testing functionality of the bias grid.

The dependence of the **PTP** differential resistance and threshold voltage on the p-stop peak concentration is shown in figures 7.14c and 7.15c. A minimum of concentration of $5 \times 10^{15} \text{ cm}^{-3}$ is required to obtain a functional device. Only small increase of differential resistance is found. However the threshold voltage shows a more pronounced dependence on the p-stop peak concentration. For high p-stop concentrations the obtained threshold voltage is too high for the **PTP** to be used during testing.

The increase of p-stop depth results in slightly higher R_{diff} and slightly higher V_{th} (see figures 7.14b and 7.15b). For $1 \times 10^{15} \text{ cm}^{-3}$ p-stop peak concentration however R_{diff} of about $10 \text{ k}\Omega$ are found experimentally, which is too low for proper strip isolation. The simulation indicates, that built-in depletion regions of the n-implants join and the electron accumulation layer

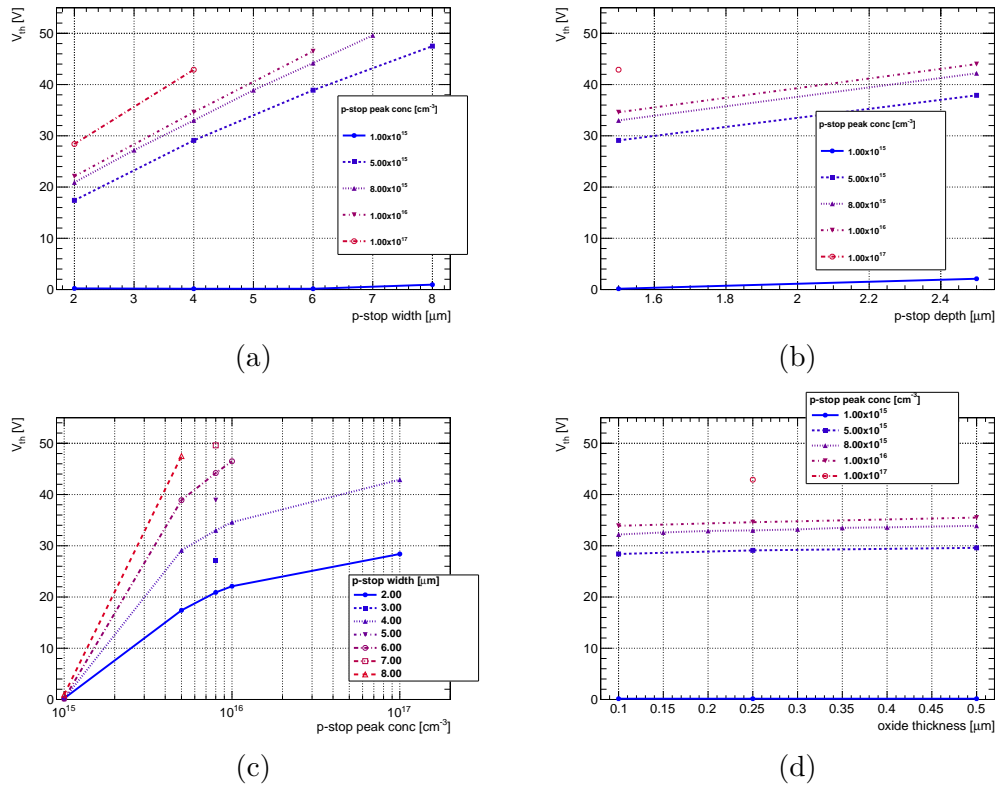


Figure 7.14: The extracted threshold voltage V_{th} depending on p-stop width (a), p-stop depth (b), p-stop concentration (c), and oxide thickness (d).

is not interrupted. Apart from insufficient R_{int} , also the capacitance at full depletion of the sensor is affected.

R_{diff} and V_{th} is not dependent on oxide thickness, as shown in figures 7.14d and 7.15d, which is the expected behavior, due to the simple model for the oxide charge density, which is assumed to be a homogeneous charge cloud at the interface Si-SiO₂.

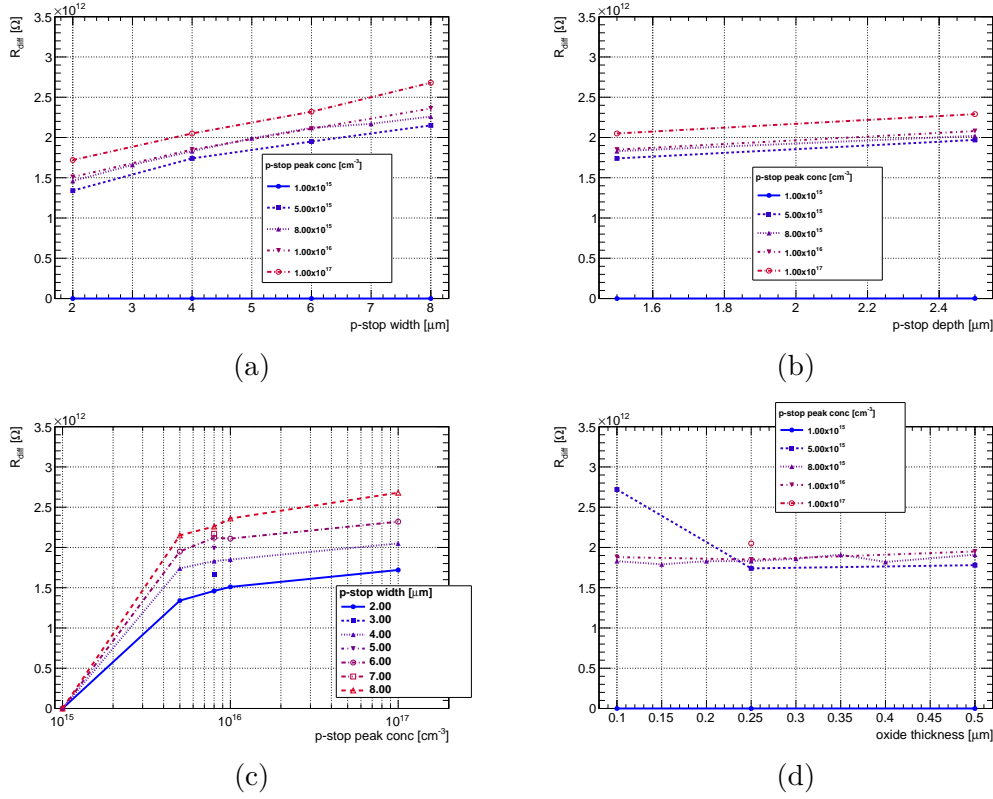


Figure 7.15: The extracted differential resistance $R_{diff}(V_{sd} = 0 \text{ V})$ depending on p-stop width (a), p-stop depth (b), p-stop concentration (c), and oxide thickness (d).

7.6 Homogeneity of strip parameters

The PS-p light sensor prototypes have 288 cells in 6 rows of 48. Different cell types as shown in figure 6.11 and in table 6.1 are realized in the geometry. While the standard cell of type 1 is $1446 \mu\text{m} \times 100 \mu\text{m}$, the $1446 \mu\text{m} \times 200 \mu\text{m}$ type 3 cells correspond to the cells opposite to the edges of the readout chips. For row 0 and 5 pixels are elongated in the y direction to $1746 \mu\text{m}$, but follow the same pattern in x. Therefore one regular row is formed of 15-2-14-2-15 cells of type 1-3-1-3-1, while for row 0 and 5 the schema is 15-2-14-2-15 of type 2-4-2-4-2. The motivation for the measurement of single cell parameters is given by the requirement to estimate the number of defect cells before the bump bonding procedure. Depending on the severity of the defects, either single cells are affected and lead to hot pixels due increased strip currents or

loss of signal, due to unwanted resistive charge sharing if the inter strip or the **PTP** resistance is too low, or the whole device shows increased current and is discarded for the use as a particle detector. This tests may be applied during prototyping, however during the module production phase, strip scans for sensors for module production are not foreseen, due to the interference with the bump bonding process.

In addition in the legacy not optimized measurement system, used during the work on this thesis, the measurement of the single strip current, including the movement of the stages, takes roughly 10s, which means a total measurement time of 24 000 days for the currently foreseen 6740 full size **PS-p** sensors with 30 720 cells [7, chap. 3.3]. Dedicated probe cards with educated switching systems could speed up the measurements. However, if the quality of the bias grid and the overall sensor quality is good enough, then it may be sufficient to use the global IV-measurement, in order to estimate the maximum number of bad strips on a sensor, which is fine, when a defective **PTP** structure always leads to an detectable increase of the total current.

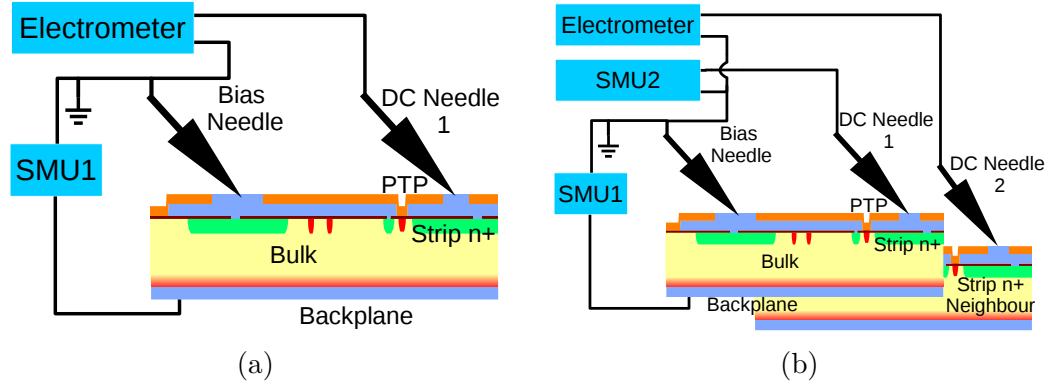


Figure 7.16: (a) The measurement schematic for the strip current and for the characterization of the **PTP**.

An automated scan procedure is performed at $V_b = -130\text{ V}$, with bias needles at ground potential contacting the bias ring and one moving needle, which contact the DC-pads sequentially. Two measurement modes are distinguished. For the measurement of the single strip current one needle is connected to the Keithley 6514 electrometer for the current measurement as in figure 7.16a. For the measured sensors $V_b \approx 1.4V_{fd}$ was used, which is be-

low the breakdown voltage of the sensors. A more detailed explanation of the measurement setup and the applied switching scheme for changing between the I_{Strip} and $R_{\text{int}}, R_{\text{pt}}$ measurements is found in [87].

For the I_{Strip} measurement in a switching matrix, the DC-needle is connected to a Keithley 6514 electrometer. For a perfectly isolated strip the measured current is given by the bulk and surface contribution of the single strip only. The measurements are sensitive to irregular **PTP**, which short the strip to the bias grid. In this case the electrometer measures the compliance value and neighboring strip currents are only slightly increased.

The measured single cell current for a good variant 1 sensor are found in figure 7.17a. A mapping of the currents to the sensor geometry is shown in figure 7.17b. The strips of 200 μm width show increased single cell currents, as expected. The single cell currents can be normalized to the cell area, as shown in figure 7.17c. In the data cells of type 1 and 2 form a group and cells of type 3 and 4 (see table 6.1), because they have a similar edge-to-area ratio and the normalization to the cell area leads to similar values. However the tentative specification on the maximum value of the normalized strip current of 0.3 nA mm^{-2} are not met.

In the data for sensors of variant 1 and 4 a general loss of strip isolation was found, which may be attributed to charge up effects during handling for variant 1. However for variant 4 sensors this could be a general problem related to the insufficient p-spray implantation.

Charge up deteriorates the strip isolation, and this has several consequences: The sum of the single strip current, excluding the full shorts in the **PTPs**, exceeds the total dark current of the sensor. For a measurement without charge-up, the sum current and the total dark current are found in figure 7.17d. This sensitivity to charge up is characteristic for the p-spray variant 4 and variant 1 sensors with low p-stop depth and p-stop dose.

In figure 7.18a three different measurements of the same variant 1 sensor, which susceptible to charge up are shown. The repetition of the first two scans show the typical pattern, which is possibly attributed to charge-up of the sensor. In a third measurement the normal behaviour is observed and

apparently the device has recovered. Ion blower treatment to prevent this behavior was applied, however this was not a reliable method to recover the sensor. The normalized single cell currents for the measured devices for variant 1, 2 and 3 are presented in figures 7.18b to 7.18d. The bad quality of the variant 4 sensors prohibited measurements in the setup.

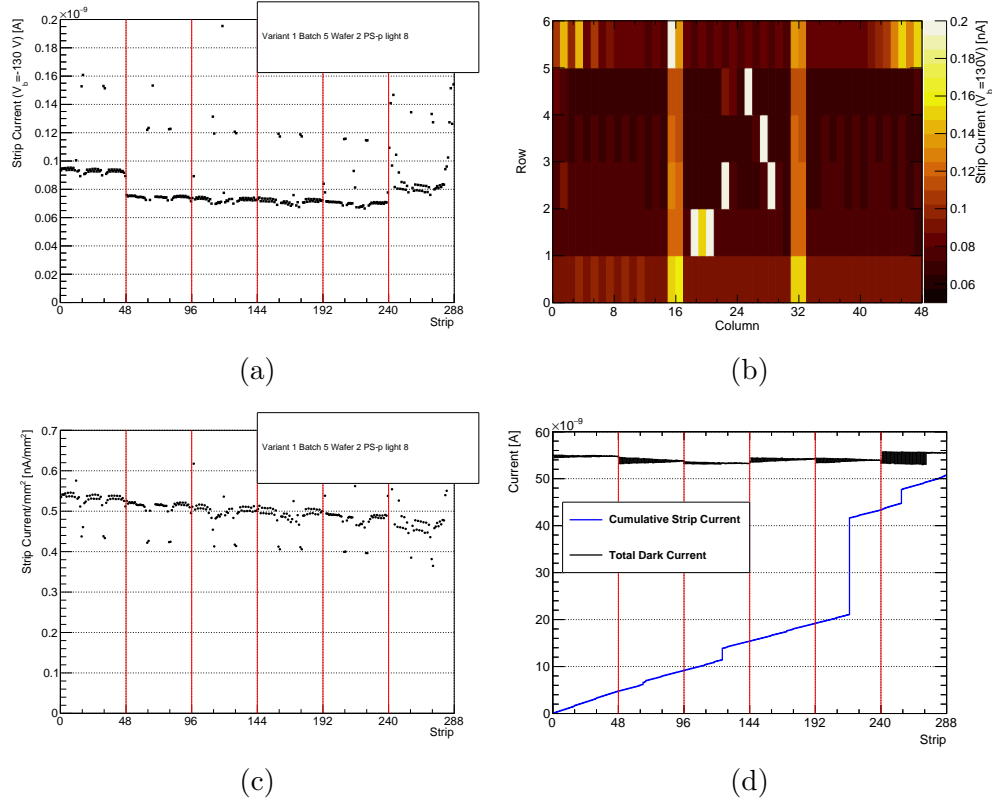


Figure 7.17: (a) The measured pixel current for a variant 1, batch 5, wafer 2 sensor, with red lines as row separators. In (b) the current mapped to the sensor geometry is shown. The cell geometry affects the current. In (c) the current is shown normalized per cell area. The tentative, maximum allowed cell current from [7, p. 143] is 0.3 nA mm^{-2} for $p_x = 100 \mu\text{m}$. (d) shows the cumulative sum of the single pixel current and the total dark current of the device measured at each measurement step.

The statistical results for the single pixel current measurements are found in table 7.6. The defective cells are defined as cells with currents deviating more than $50 \times \mathbf{MAD}$ from the median current, which is a robust procedure to automatically detect outliers in the data. The experiment allows $N_{bp} = 0.2\%$ bad pixels in a tentative specification list [7, chap. 9.2.1.7]. However the

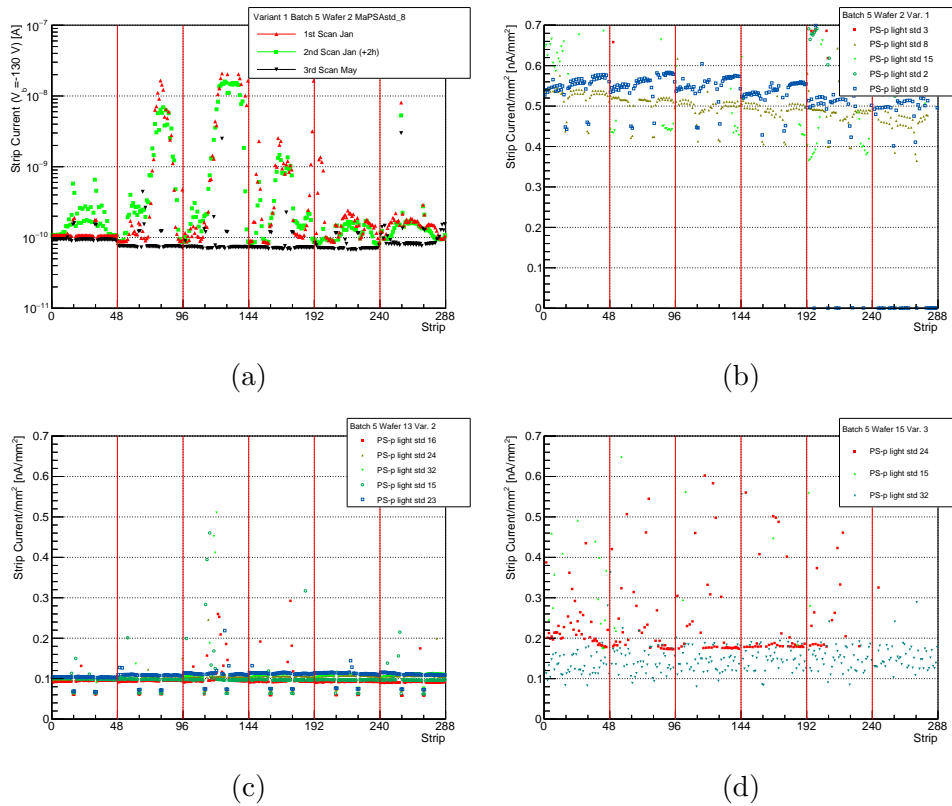


Figure 7.18: (a) shows the effects of charge up on the pixel current. (b-d) The normalized single strip currents for the measured devices from different variants (Batch 5).

classification of a pixel as bad pixel is depends on other factors, apart from single pixel current and inter-pixel resistance. Different failure modes could lead to a bad pixel in the final module:

- Interruption of pixel implant causes a local inefficiency
- High single pixel current causes hot pixel and additional noise propagates to the stub logic, resulting fake stubs.
- Defective bump bonds inhibit collection of the signal on the readout chip.

Table 7.6: The Median cell current for batch 5 PS-p light sensors and the **Median Absolute Deviation (MAD)**. Defective cells are defined as cells exceeding the median cell current the corresponding cell type by $50 * \text{MAD}$.

| Var | Wafer | Sensor | Cell Current ($p_x = 100 \mu\text{m}$) | | Cell Current ($p_x = 200 \mu\text{m}$) | | Defective Cells [%] |
|-----|-------|--------|--|---------------------------|--|---------------------------|---------------------|
| | | | Median [nAmm ⁻²] | MAD [nAmm ⁻²] | Median [nAmm ⁻²] | MAD [nAmm ⁻²] | |
| 1 | 2 | 3 | 2.075 | 1.363 | 5.370 | 4.347 | 2.08 |
| 1 | 2 | 8 | 0.506 | 0.018 | 0.413 | 0.014 | 2.08 |
| 1 | 2 | 15 | 0.972 | 0.544 | 2.072 | 1.407 | 23.26 |
| 1 | 2 | 2 | 1.783 | 1.047 | 0.993 | 0.383 | 1.04 |
| 1 | 2 | 9 | 0.544 | 0.021 | 0.447 | 0.012 | 3.03 |
| 2 | 13 | 16 | 0.093 | 0.001 | 0.061 | 0.001 | 2.78 |
| 2 | 13 | 24 | 0.105 | 0.001 | 0.070 | 0.002 | 0.69 |
| 2 | 13 | 32 | 0.107 | 0.003 | 0.074 | 0.001 | 2.78 |
| 2 | 13 | 15 | 0.097 | 0.001 | 0.064 | 0.001 | 4.86 |
| 2 | 13 | 23 | 0.111 | 0.003 | 0.074 | 0.001 | 1.04 |
| 3 | 15 | 24 | 0.267 | 0.091 | 10.194 | 1.443 | 21.88 |
| 3 | 15 | 24 | 21.469 | 4.694 | 13.084 | 0.209 | 0.00 |
| 3 | 15 | 24 | 0.147 | 0.021 | 0.105 | 0.020 | 1.39 |

7.6.1 Optical inspection

Two dimensional maps of cells, recognized as outliers in the aforementioned analysis, were produced for each scanned sensor. In an optical inspection under the microscope all the smaller clusters not exceeding a couple of pixels with high pixel current could be attributed to defective **PTPs** or scratches as shown in figures 7.19b and 7.19c. Also a mask misalignment of $2.0 \mu\text{m}$ was observed (see figure 7.19a), which could have negative effect on the HV-stability of the sensors, because it removes the metal overhang of the inner bias dot.

7.6.2 Interpixel measurements

For a PS-p light sensor a measurement of interpixel resistance is motivated. Irradiation causes a drop in the interpixel resistance. Nonetheless, after irradiation the interpixel resistance should be an order of magnitude higher than the equivalent resistor of the readout chip for biasing the pixel, which ensures high spatial resolution and avoids spreading of the signal charge to the neighboring electrodes. In the desired configuration all the signal charge should flow into the amplifier [88, chap. 2.9.6]. For the tracker upgrade the CMS experiment requirement is $R_{\text{int}} = 1 \text{ G}\Omega \text{ cm}$ before irradiation. The value for $R_{\text{diff,ptp}}(V_{ds} = 0 \text{ V})$ must be at least in the same order of magnitude as

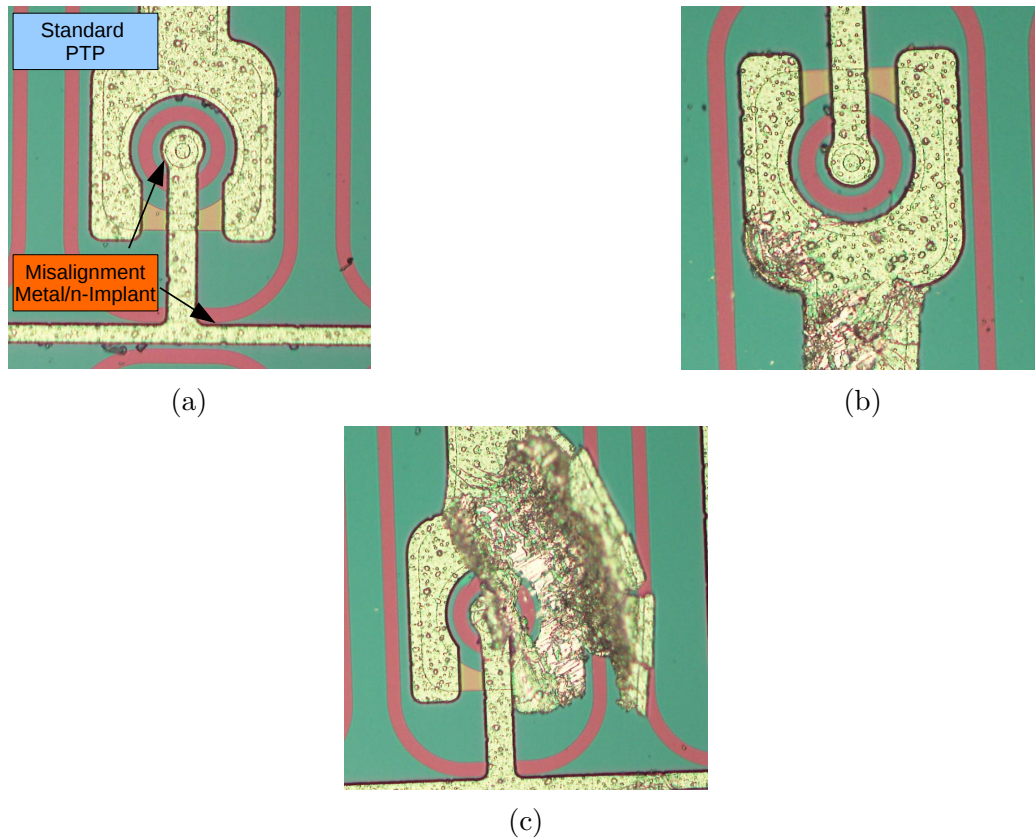


Figure 7.19: Pictures from optical inspection of the **PTP** structures: (a) A regular **PTP** structure, where mask misalignment between metal and n-implant is visible. (b,c) Observed irregularities corresponding to strips with high pixel dark current.

the inter pixel resistance, otherwise a part of the signal is lost to the bias rail. Very high values for $R_{\text{diff,ptp}}(V_{ds} = 0 \text{ V})$ should be avoided as well, because this implies a big voltage drop across the resistor and the capability of the bias grid for testing is reduced. It is supposed, that this effect lead to destructive sparking during testing for several variant 3 sensors.

The measurement is realized as presented in figure 7.16b. A second Keithley 2410 **SMU** is used to apply a voltage ramp across the **PTP** structure, while the current of the direct neighbor pixel is measured simultaneously with a sensitive Keithley 6514 electrometer. For analysis, a linear fit is applied in the region -1.1 V to 1.1 V for the **PTP** current and neighboring pixel current. The differential resistance is extracted from the slopes. This method correctly

accounts for the leakage current of the strips. The number of measured pixel pairs in total is 144 per sensor. For each row 4 pairs of pixels with pitch 100 μm and 200 μm , and 20 pairs with pitch 100 μm are measured. An example of the recorded currents over **PTP** and neighboring strip is found in figures 7.20a and 7.20b.

The extracted differential resistance from the neighbor pixel normalized to the macro pixel length p_y is shown in figure 7.21b and $R_{\text{diff,ptp}}(V_{ds} = 0 \text{ V})$ extracted from the current over the **PTP** in figure 7.21a for sensor of different variants.

Also the nonlinear behavior of the **PTP**, especially the homogeneity of V_{th} is observed. Repeated measurements on the same sensor showed the sensitivity of the **PTP** to charge up effects.

Figure 7.20a shows, that there is a spread in the threshold voltages due to fluctuation in the production process of the wafer. This could be attributed to the mechanical misalignment of the masks and surface defects. The grouping of the pixel currents observed in 7.20b is due to the different cell types. For sensors affected by charge up the neighbor pixel currents are increased due to the low differential resistance of the **PTP** at 0 V (see figures 7.20c and 7.20d) and the reduction of the interstrip resistance. However it is supposed, that the **PTP** is more susceptible to charge up, because of the smaller p-stop width and smaller length of the gate.

Comparing this results with the expected threshold voltages and differential resistance from simulations, the observed quantities are lower in the measurement. This may be partially explained by underestimating the real initial surface charge density and overestimating the real p-stop dose. Especially for this vendor the surface charge density was reported to be higher for the unirradiated case [82] and measurements (see section 7.3) on MOS structures confirm this hypothesis.

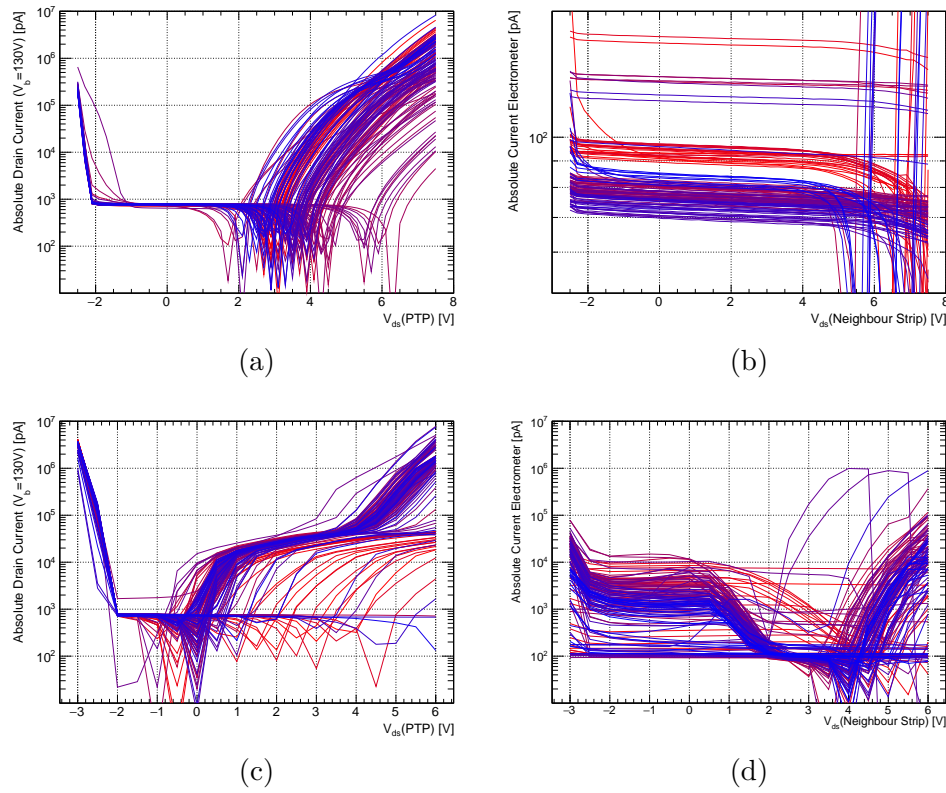


Figure 7.20: (a) shows the absolute current measured with SMU2, when a voltage is applied across the **PTP** for a PS-p light sensor of batch 5, wafer 2. The corresponding current measured on the DC-pad of the neighbor strip is shown in (b). (c) and (d) show a measurement for a sensor affected by charge up from the same wafer.

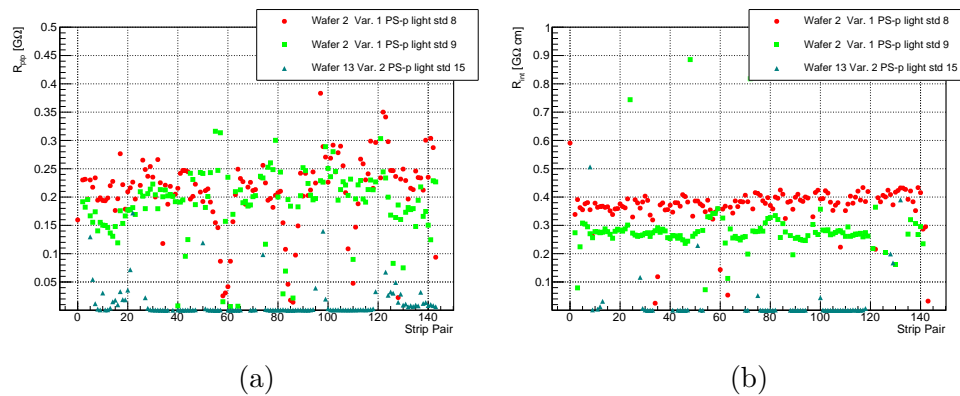


Figure 7.21: The differential resistance of the **PTP** at 0 V (a). (b) The interpixel resistance extracted from the linear fits.

7.7 Summary

The results of the static electrical characterization of the unirradiated sensors indicate that variant 1 and 2 are suitable candidates to be used as sensors in a particle tracker. Considering the increase of the electric field after irradiation, especially the variant 1 is preferred, which has the low p-stop concentration and p-stop depth. For variant 4 in alternative p-spray technology, no samples with sufficient strip isolation were found. Therefore another prototype run with higher p-spray dose and additional simulations is required in order to understand the issues.

However the measured interpixel resistance and number of bad pixels do not meet the experiment specifications yet. Regarding the bad pixels this is mostly attributed to the scratches by insufficient packaging by the vendor, handling and problems in the mask alignment for the metal layer. The highly optimized **PTP**, is designed at the minimum feature size supported by the vendor, however the optimization is a trade-off between sensor yield and sensor efficiency. If one takes into account the macro-pixel geometry, the bias dot, where charge is possibly lost has only a small impact on the geometric efficiency, but a single defective **PTP** may lead to early breakdown of the sensor, it should be considered to make a better trade-off towards more robust geometries in future prototype runs, if necessary.

In addition high sensitivity to charge up in the low p-stop concentration variants was found. This charge-up was induced during handling and ion-blower treatment was not a reliable method to recover the sensors. Charge-up lowers the **PTP** off state resistance and shorts the pixels via the bias grid. This is consistent with the findings in the $C^{-2}V$ characteristic, where loss of pixel isolation leads to differences in full depletion voltages and full depletion capacitance. For a standard geometry sensor with $w = 25 \mu\text{m}$ and $p = 100 \mu\text{m}$ the full depletion voltage $V_{\text{fd}} = 1.32V_{\text{fd0}}$, where V_{fd0} is the depletion voltage of a unstructured p-n junction. Therefore loss of strip isolation across the **PTP** may partially explain the difference in full depletion voltage.

The sensitivity to charge-up could be reduced by increasing slightly the p-stop width in the **PTP** and the distance of bias dot implant to pixel implant, which increases the threshold voltage and increases the off state resistance.

Chapter 8

Module pretest, calibration and analog performance

In figure 8.1a a picture of one inverted **Macro-Pixel-Sub-Assembly block (light) (MaPSA-Light)** module built during the work on this thesis is shown. For the modules, a qualification procedure was established. The tests check IV-curves, proper functionality of the communication with the readout chip, and the calibration of the chip. The comparison of IV-curves of the sensor before assembly and the module after assembly shows, whether the bump bonding, wire bonding and gluing lead to additional current. The challenges to be faced for production of high-quality modules are shorts between pixels, introduced by residues of the bump bonding process, the correct clearance of the bond wires to the sensor edge for the inverted module (see figure 8.1b) and badly connected bump bonds.

Interconnected pixels result in higher single channel noise due to additional input capacitance. Insufficient bond wire clearance leads to additional module currents or malfunction of the readout chip. Badly connected bumps have lower noise due to lower input capacitance and poor response to signals.

In case no significant deviations from the sensors initial IV-curve are found for the assembled and wire-bonded module, a test of the readout chip for

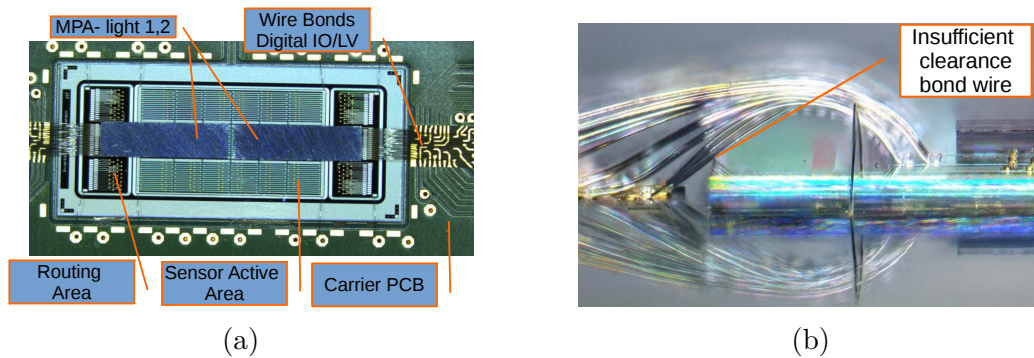


Figure 8.1: (a) Shows one inverted module with two readout chips connected to the sensor after connecting the routing area to the carrier PCB with wire bonds. Due to limitations in the chosen low-cost PCB technology a maximum of two MPA-lights can be used. (b) Tight tolerances together with insufficient mechanical alignment result in wire bonds touching the sensor edge.

proper communication follows, which shows, whether the digital and analog currents of the readout chip are within the specifications.

In the following step the equalization of the comparator response (calibration) of the chip is performed under the application of the sensor bias voltage. The calibration is done in an iterative procedure and results in a set of **TRIMDAC** values, which reduce the channel-to-channel variation in the detector response to a minimum. For this procedure the data of the asynchronous counters are recorded in a simultaneous scan of the **THDAC** register. The obtained pedestal curves (Slices of the data for a fixed channel in figures 8.2a and 8.2b) can be described by the difference of two closely spaced error functions. This is a result of the Schmitt trigger logic realized in the front-end electronics of the readout chip, which means the counters increment, when the analog signal crosses the set **THDAC** threshold regardless of the signal polarity on the falling edge of the discriminator signal. However, the curves are sufficiently described by a Gaussian, which reduces the number of free parameters of the fit. The first threshold scan is performed loading the standard **TRIMDAC** values. Using the relative Q -value $Q_{\text{rel}} = .5\text{LSB}_{\text{TRIMDAC}}/\text{LSB}_{\text{THDAC}}$ (see table 6.3) and the target pedestal value, with a linear extrapolation a **TRIMDAC** value for each channel is predicted. The target pedestal value is estimated with the mean of the pedestal

values or alternatively set manually. At least three iterations are necessary for the procedure to converge.

One advantage of the applied Newton's method is, that it is sufficient to know the approximate Q_{rel} , while the integral and differential non-linearity of the DACs do not affect the quality of the calibration. During the testing of the prototypes it was found, that for some of the channels the dynamic range of the **THDAC** was not sufficient for the nominal readout chip bias voltages (see figure 8.2d). This is an effect of insufficient statistical matching to and will be improved in the next version of the chip.

For the **MPA-light** the minimum achievable threshold dispersion (see section 6.2.2) in units of LSB_{THDAC} is $\text{ENC}_{\text{spread}} = \sqrt{1/12 \times (LSB_{\text{TRIMDAC}}/LSB_{\text{THDAC}})^2} = 0.74$. This estimation is valid, if after the calibration the distribution of the pedestal values P_i is uniform in the interval $I = [\bar{P} - Q_{\text{rel}}, \bar{P} + Q_{\text{rel}}]$, where \bar{P} is the mean value of the pedestals after the trimming procedure.

The total **ENC** for a module is $\text{ENC}_{\text{tot}} = \sqrt{\text{ENC}_{\text{spread}}^2 + \text{ENC}_{\text{channel}}^2}$.

After calibration the noise figure ENC_{tot} of a module is extracted from the threshold scan data, via the Gaussian width of the sum signal of all connected and calibrated channels as shown in figure 8.2c.

In figures 8.2a and 8.2b the asynchronous counter data of each channel for a simultaneous threshold scan of two different prototype modules with two **MPA-light** chips and in total 96 channels readout is shown with equal statistic. Typically, the channels connected to the border cells of the sensor have an expressed non-Gaussian tail towards lower **THDAC** values, which is correlated to the opening of the shutter. For the inverted/standard module ENC_{tot} $(237.4 \pm 0.1) e / (243.8 \pm 0.1) e$ is extracted for σ from the Gaussian fit (figure 8.2c). For the standard module a slightly higher non-Gaussian tail due to the correlated noise of the shutter signal is observed. The **ENC** of both module types are compatible and the differences well explained by variations in the module production. The data of the inverted module follows closely the Gaussian extrapolation, which indicates the high quality of the module regarding correlated noise.

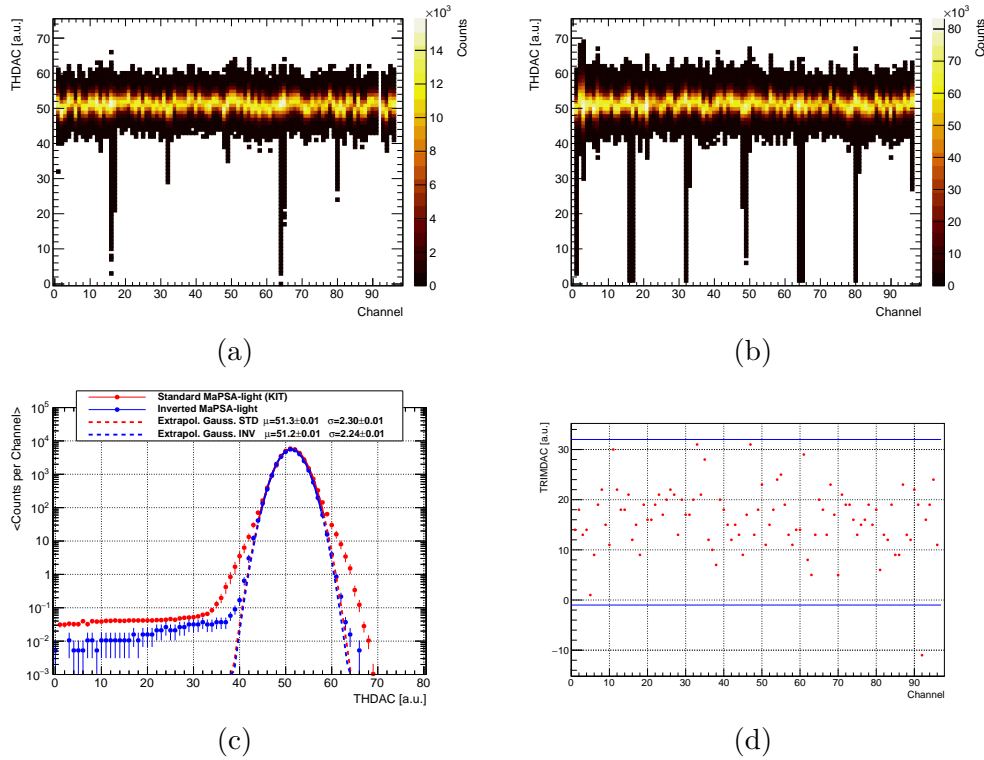


Figure 8.2: (a-b) Shows the data from a threshold scan for the inverted **MaPSA-Light** (left) and the a standard **MaPSA-Light** (right) assembled by KIT with in total 96 channels readout at 100 V after calibration. In (c) the single channel counter data is added and normalized to the number of channels. The extracted total noise figure is taken from a Gaussian fit. In (d) the distribution of the predicted **TRIMDAC** values after the last calibration step is shown. The blue lines indicate the maximum and minimum possible register values. One of the channels is outside the dynamic range and therefore switched off during the operation.

Chapter 9

Measurement of detector response with IR-laser system

The inverted **MaPSA-Light** prototype was tested with an infrared laser system, which was commissioned in the context of this work. The laser system allows precision studies of the response of the prototype to short laser-pulses. Stepper motors with 1 μm accuracy allow adjustment of the laser focus in z-direction and movement perpendicular and parallel to the cells.

9.1 Laser system specifications and setup

A general sketch of the laser system with the **MaPSA** under test is provided in figure 9.1 and the specifications of the system in table 9.1. Results from an in-detail characterization of the laser-beam parameters according to the best practice recommendations in [89] are found in [90].

A laser driver is used for charge injection in the laser diode, which is inside the laser head. The pulse energy is controlled mainly with an adjustable attenuator, which does not affect the properties of the laser pulse in the time domain and is capable of 50 dB attenuation of the nominal 9.1 pJ pulse. For detectors with **MIP** sensitivity an attenuation of about 20 dB is necessary to achieve a signal similar to a **MIP**. An beam splitter beam distributes 90 %

of the beam power to an additional powermeter, which allows to monitor the laser power, and 10 % to the lens system, which comprises a monochromatic collimating lens and an aspheric micro-focus. The expected intensity profile is approximately Gaussian near the beam waist. However, higher modes, which are not fully suppressed by the single-mode fiber, cause small non Gaussian contributions to the beam profile. For the tests the signal height was adjusted to produce around 17.0×10^3 **EHPs**, which corresponds to a **MIP**. A peltier controller inside the laser-head keeps the laser diode at constant temperature and ensures excellent long-term stability of the pulse energy.

Table 9.1: Specifications of the laser system

| Symbol | Definition | nominal Value/Unit |
|--------------------------------|-----------------------------------|-------------------------|
| λ_{laser} | Wavelength | (1055.6 ± 7.8) nm |
| $\alpha^{-1}(\lambda_{laser})$ | Inv. absorption coeff. Si (300 K) | (780 ± 225) μ m |
| $\text{Max}(f_{rep})$ | Max. repetition frequency | 41 MHz |
| $\text{Max}(E_p)$ | Max. pulse energy after SM-fiber | 9.1 pJ |
| $\text{Min}(FWHM_p)$ | Min.(Full With Half Max. Pulse) | 48 ps |
| TJ_p | Total Jitter Pulse | 2.7 ps |
| M_x | Beam quality factor in x | 2.37 |
| M_y | Beam quality factor in y | 1.53 |
| $d_{0x/y} = 2W_0$ | Waist size diameter | 3.6 μ m |

The system is used

- to test the homogeneity of the charge collection efficiency,
- to quantify charge loss in the p-stop region,
- and to reconstruct the analog pulse shape of the binary readout chip.

For each position in space 1000 laser pulses for all settings of the 8-bit mutual **THDAC** register (see section 6.2.3) were recorded. This allows to measure the mean collected charge per laser pulse. Two different acquisition modes were tested:

- Asynchronous mode: This mode is only intended for calibration and testing. Asynchronous refers to the ripple counters, which have no syn-

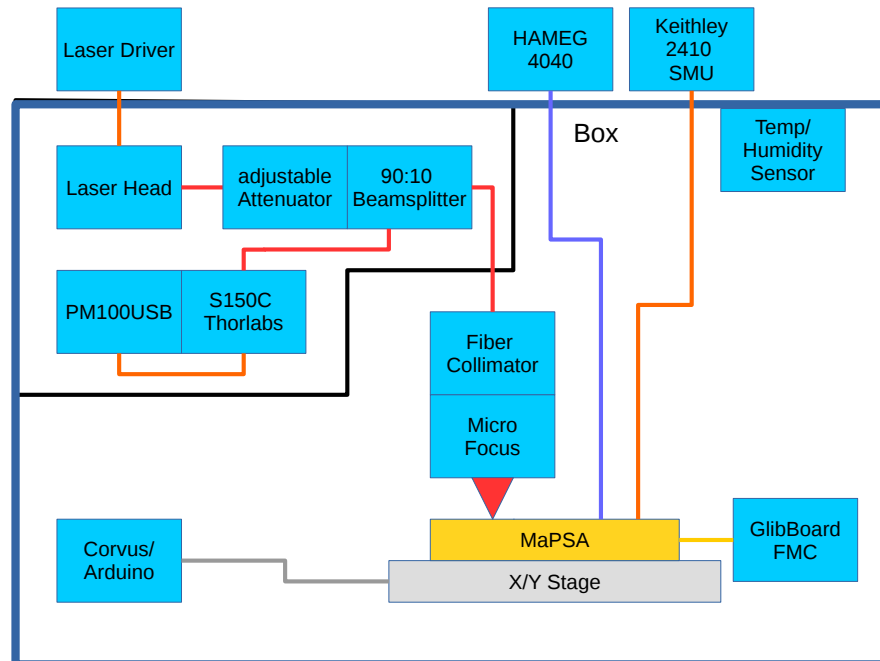


Figure 9.1: A simplified sketch of the laser test setup.

chronization with the system clock. However, with the help of a synchronized shutter signal, a scope like sampling of the analog signal is possible.

- No processing mode (section 6.2.3): In the no-processing mode the binary raw data frame is stored with a time stamp in the 96 cells on-chip **SRAM** (L1 data path), if in any of the channels the edge-detector is active, no online data reduction is applied.

9.2 Tests with constant laser repetition rate

In order to obtain sufficient statistics fast, for the spatial scans, the laser pulse was not synchronized with the system clock of the **MaPSA-Light** and pulses were fired at a rate of 100 kHz continuously. In this case, the shutter opening time was chosen to record 1000 pulses. The tests were conducted under dry air laboratory conditions at 100 V bias, where the tested sensor drew about 40 nA dark current.

The obtained single-channel spectra contain the pedestal peak and eventually a signal s-curve in case of the asynchronous readout, as shown in figure 9.2a. In a small the region around the maximum a Gaussian is fit to the single channel spectrum.

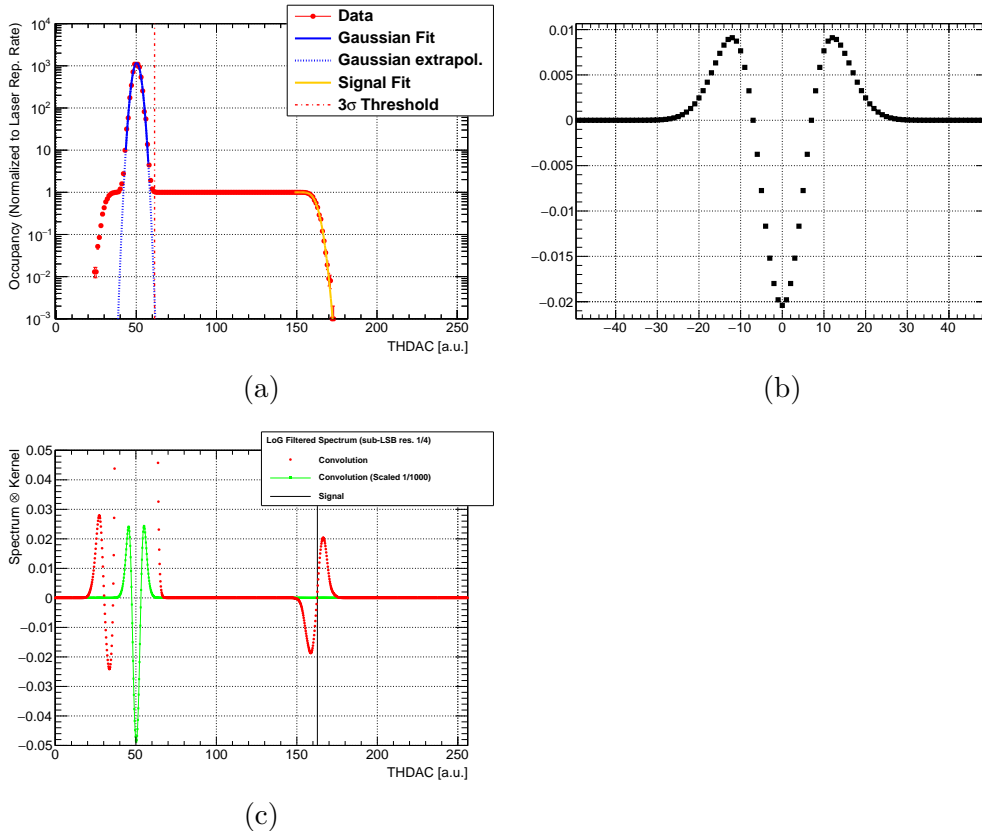


Figure 9.2: (a) A single channel spectrum normalized to the pulse repetition rate contains the noise peak and a signal s-curve. (b) The **Laplacian of Gaussian (LoG)** kernel with $\sigma = 7$ used for the convolution. (c) The signal may be extracted directly from the filtered spectrum. A scaled version is overlaid.

A robust step finding algorithm is used to find the signal with sub **LSB** accuracy [91]. The search region for the algorithm is set to $3 \times \sigma$ above the mean obtained from the Gaussian fit to the full scale range of the **THDAC**. A Laplacian of Gaussian kernel (see figure 9.2b) is convoluted with the spectrum, where the Gaussian σ defines the scale space for the search. The size of the kernel is defined by the width of the excitatory-region and the desired sub-**LSB** resolution, which is chosen to be 0.25. Edges are detected as zero-

crossing in the convolution, as shown in figure 9.2c. The search algorithm presets the parameter for an error function fit of the s-curve of the laser signal (see figure 9.2a). However the edge detection is sufficiently accurate to determine the position of the signal.

The collected charge in units of **LSB** is the difference of the mean of the Gaussian fit to the noise and the mean of the error function. With this procedure it is possible to reconstruct the analog signal with sub-**LSB** resolution and additional errors, due to finite accuracy of the **TRIMDAC** tuning procedure are avoided.

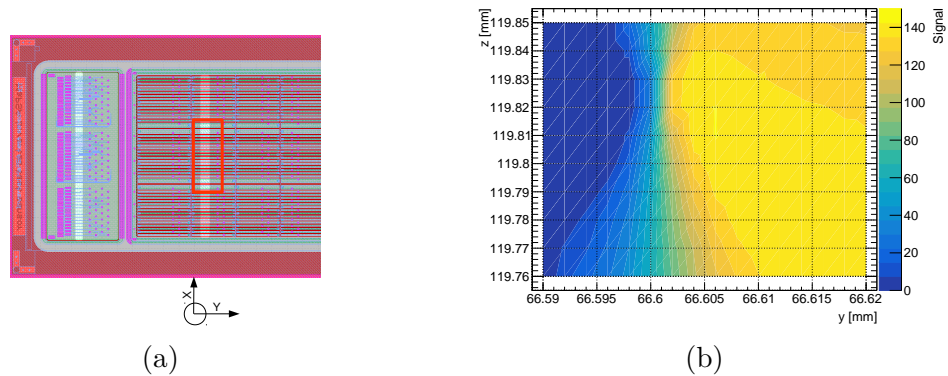


Figure 9.3: (a) Coordinate system for the laser tests. The red square is the test region. x defined perpendicular to long edge of cells, y perpendicular to metal opening. (b) The YZ-scan shows the signal of a single channel and the signal drop at the metal edge at $y \approx 66.6$ mm .

The coordinate system used in the this chapter is defined as in figure 9.3a. An opening in the metal layer on the back-plane of the sensor allows backside illumination. The theoretical initial charge distribution inside the sensor is shown in figures 3.6a to 3.6e.

For good position sensitivity the position of the beam waist must be defined with respect to the surface of the sensor. The applied procedure for focus finding utilizes the signal of a single readout channel only. The edge of the back-plane metal opening was used to apply the knife-edge technique, which is a simple method for profiling a focused laser beam or accurate positioning of a probe in a beam. This technique comprises a 2D scan in y and z direction, and the pedestal subtracted signal on the test cell as function of

the yz -coordinates is shown in figure 9.3b. From the data, the laser focus is reconstructed at $z = (119.825 \pm 0.005)$ mm. In the blue region the metal layer reflects the laser light. The widening of the beam and the beam waist are clearly visible.

The resulting signals of a coarse scan perpendicular to the long edge of the cells in steps of $2\ \mu\text{m}$ in the laser focus are found in figure 9.4a. Cell 17 and 32 have $200\ \mu\text{m}$ cell width in x . For all other cells shown in the plot, the cell width in x is $100\ \mu\text{m}$. The channel-to-channel variation observed in the sum signal in figure 9.4b is $\mathcal{O}(10\%)$ and is explained by the gain variation across the channels, charge collection efficiency variation and interference effects as described in [92]. The dispersion of the gain of the readout channels is an irreducible, intrinsic feature of the readout chip and depends on the quality of the production process. Apart from the typical inter-cell variation, the charge collection efficiency can vary across the sensor surface, due to local defects, where charges get trapped. Interference leads to a change in the absorbed and reflected laser power. This is sensitive to minor changes in the thickness of the silicon-oxide passivation layer of the front side and depend on the spectral width of the laser light [92, p. 37].

The signal of strip 17 has a significant bump in a region outside the geometrical cell edges at greater x -values. The neighboring $200\ \mu\text{m}$ cell is not connected to a readout chip. Therefore the potential of this cell is different and defined by the **P_{TP}** and inter-strip resistance to the neighboring cell only. In this case increased capacitive and resistive coupling could lead to a signal in the adjacent cell, which is not illuminated. Apparently this is an edge effect and needs additional studies, with a full assembly, where all cells of the sensor are connected to readout chips, where this effect should not appear.

A fine scan in $1\ \mu\text{m}$ steps between two adjacent cells next to the laser focus is shown in figure 9.5a. The data allows to study charge sharing between the cells. The peak, which is observed in the signals of all cells, is caused by the back reflection of light in the regions, where aluminum covers the implant of the cells [92, chap. 3.4.2]. The amount of created charge depends on the surface properties due to reflections.

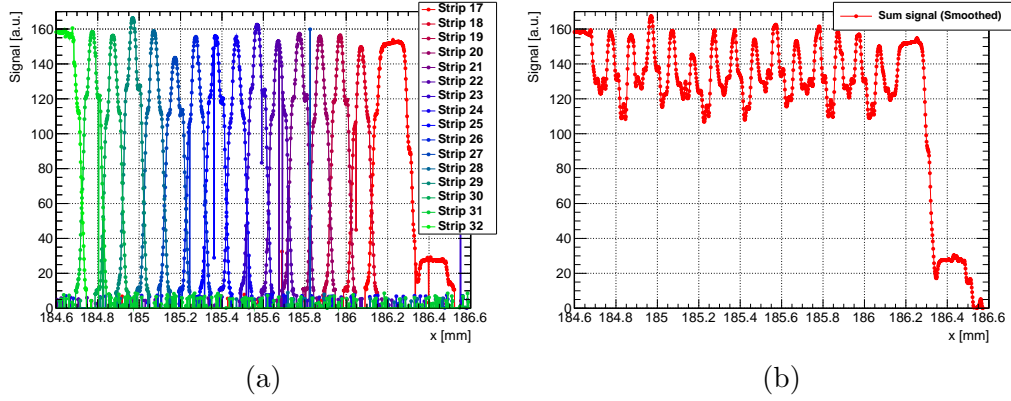


Figure 9.4: The response of the single channels to the laser pulses moving perpendicular to the long edge of the cells (a). The sum signal of all channels shows good uniformity across the channels(b)

For the sum signal a small drop is observed in the region between the p-stop implants, where a small amount of charge is possibly lost. The tail towards small x-values of the individual signals is due to the remaining angle of the pointing vector of the beam and the normal of the sensor surface, which is explained by the finite mechanical accuracy of the fixture.

A measure for charge sharing is found in figure 9.5b, where the difference of the signals divided by their sum is plotted in black. These curves are obtained from the data in figure 9.5a. This representation of the data is independent of the reflection coefficient, which depends on the laser position. It is remarkable that the highest gradient is observed in the regions in between the two p-stop strips.

The zero crossing of the asymmetry curve is the point, where both pixel share the equal amount of charge. The measured width of the charge sharing distribution of $\text{FWHM}_{\text{tot}} = (18 \pm 2) \mu\text{m}$ is indicated by the orange lines. The important contributions for the width of the charge cloud are diffusion and the width of the beam waist

$$\text{FWHM}_{\text{tot}}^2 = \text{FWHM}_{\text{diffusion}}^2 + \text{FWHM}_{\text{beam}}^2. \quad (9.1)$$

In this case the contribution from laser spot is $\text{FWHM}_{\text{beam}} = 2w_0\sqrt{\ln 2}/\sqrt{2} = 2.12 \mu\text{m}$. Therefore one obtains,

$$\text{FWHM}_{\text{diffusion}} = \sqrt{\text{FWHM}_{\text{tot}}^2 - \text{FWHM}_{\text{beam}}^2} \quad (9.2)$$

$$\text{FWHM}_{\text{diffusion}} = (17.9 \pm 1.0) \mu\text{m}. \quad (9.3)$$

For a sensor with n-strips in p-bulk material and a negative voltage applied at the back-plane, most of the signal measured by the readout chip is induced by electrons. The maximum drift time for electrons or holes $t_{d,n/p}$ is for the sensor with $d = 200 \mu\text{m}$ and $V_b = 100 \text{V}$ thickness is estimated with the average field approximation $\bar{E} = V_b/d$ as

$$t_{d,n} = d^2/(\mu_n V_b) = 2.76 \text{ ns}, \quad (9.4)$$

$$t_{d,p} = d^2/(\mu_p V_b) = 8 \text{ ns} \quad (9.5)$$

In equation (9.4) the assumption of a constant mobility is a simplification of the real situation for a biased sensor. In the bulk the most important effect for mobility variation is the electric field, which depends on doping concentration and bias voltage. For the unirradiated sensor a constant doping concentration in the bulk is expected and the mobility therefore only deviates from the mobility in the bulk close to the surface and close to the back plane of the sensor.

For the laser focus adjusted to the metal layer covering the back plane, most of the charges are generated near the back-plane as in figure 3.6c. For a point like charge cloud the spread during drift, due to diffusion and the width at 300 K is estimated [88, p. 21]

$$\sigma_{x/y,n/p} = \left(2D_{n/p}t_{d,n/p}\right)^{1/2} \quad (9.6)$$

$$= \left(\frac{2kT}{q}\mu_n t_{d,n}\right)^{1/2} \quad (9.7)$$

$$= \left(\frac{2kT}{q}\frac{d^2}{V_b}\right)^{1/2} \quad (9.8)$$

$$\text{FWHM}_{x/y,n} = 2\sqrt{2 \ln 2}\sigma_{x/y,n} = 10.7 \mu\text{m}. \quad (9.9)$$

The discrepancy with the value obtained in the measurement (see equation (9.3)) is most probably due to the not perfectly aligned laser beam and the effect of the p-stop implantation. Furthermore this simple model assumes a point like charge generation, which does not account for the real distribution of the generation rate from a laser beam as shown in figure 3.6c. Equations (9.4) and (9.8) show the effect of bias voltage on charge sharing due to diffusion [93]. For higher bias voltage a smaller σ is obtained, which deteriorates the spacial resolution for clusters of a size greater than two. The beneficial effect is a faster charge collection due to reduced drift time.

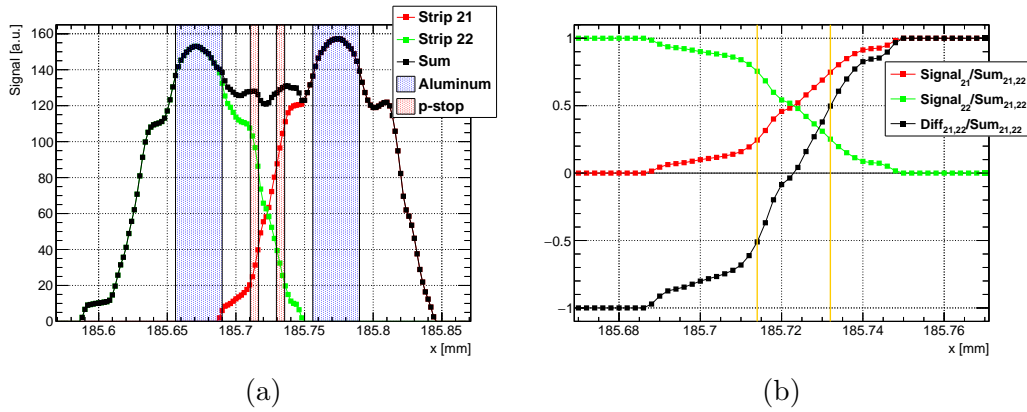


Figure 9.5: (a) A scan in $1\ \mu\text{m}$ steps along x of adjacent channels near the laser focus for studies of charge sharing. The overlay of the sensor geometry is centered with the interpolated point of equal shared charge. (b) Unbiased measures of charge sharing along x are obtained by dividing the difference of signals by the sum of signals. The FWHM $(18 \pm 2)\ \mu\text{m}$ of the distribution charge cloud is indicated by the orange lines.

9.3 Tests with synchronized laser pulses

Analog pulse shape reconstruction with a binary readout chip is achieved with synchronization of the laser pulses with the chip clock, as shown in figure 9.6a. The analog pulse shape reconstruction allows measurement of the performance of the analog front-end of the chip at the nominal working point, regarding signal peaking time and signal decay time, electronic efficiency and allows to discover unwanted dead-time introduced in the digital domain.

As clock source for the readout chip, the Agilent 8110A pattern generator was used. A second synchronized probe signal probes busy state at 400 kHz in the coincidence unit. With this technique, a synchronized trigger signal and a laser pulse is generated, if the chip is ready for data acquisition. For pulse shape sampling, the closing of the shutter upon receipt of a trigger signal is delayed up to 200 ns in steps of 6.125 ns. This is realized as a programmable shift register in the **GLIB**.

The jitter of the trigger with respect to the clock at the input terminals of the **GLIB** was measured at (300 ± 100) ps with a high bandwidth oscilloscope and this puts an upper limit to the accuracy of the time measurement. The NIM-coincidence logic ensures that triggers are asserted within $2.5 \mu\text{s}$, when the busy signal is low and the shutter is open. The full range of **THDAC** and the full range of the delay was scanned with statistics of 1000 laser pulses at each point. In the so called no-processing mode memories and the counter data were readout simultaneously.

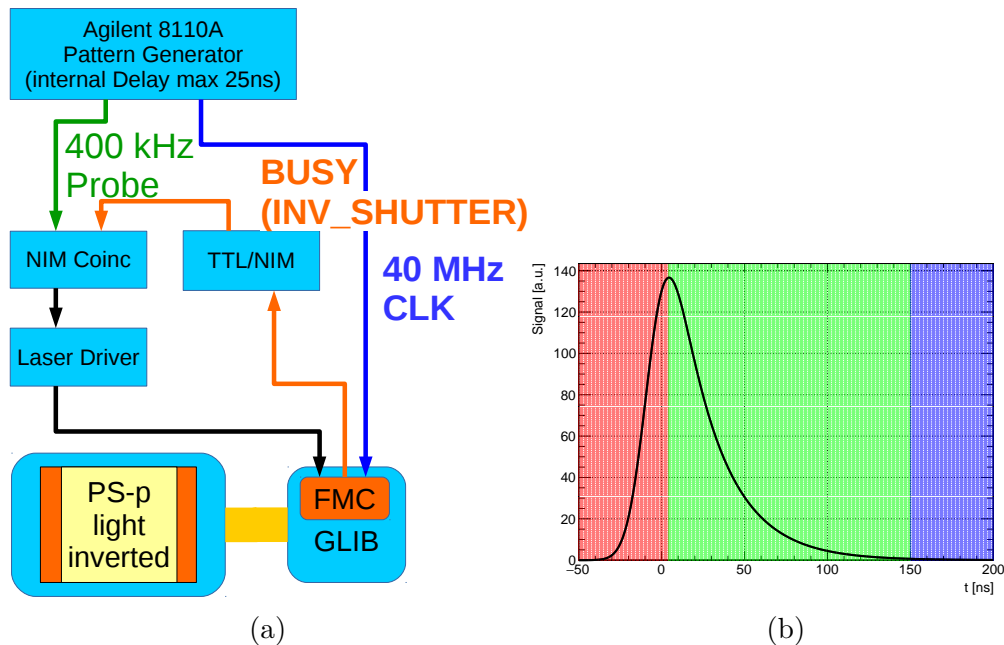


Figure 9.6: (a) A simplified sketch of synchronization scheme. (b) The different situations, which occur during pulse shape sampling.

When a trigger is asserted different situations are possible (sorted by increasing delay):

- Due to the difference of the optical path length and the trigger path length it is possible, that the laser pulse has hit the sensor and the signal has decayed, while the shutter is still closed. The chip is still busy sending the data and the ripple counter are not active. In this case no pulses are counted with the ripple counter, which corresponds to 0 ns in figure 9.7 or the red region in figure 9.6b.
- The laser pulse hits the sensor and the shutter is closed at t_1 before the signal has fully decayed. If the pulse is above threshold at $t_0 < t_1$, the counter does not detect it. If the pulse height is below threshold at t_1 the counter increments. For a fixed delay setting the counter spectrum has a rising and a falling edge. Only the rising edge defines the pulse height at t_1 . This is true for delays from 6.25 ns to 100 ns in figure 9.7 or the green region in figure 9.6b.
- If the pulse has fully decayed, before the shutter is closed, additional delay of the shutter closing has no effect on the recorded data and the counter increments always, if the maximum of the pulse is above threshold, which is the case for delays more than 100 ns figure 9.7 or the blue region in figure 9.6b.

For all recorded curves a total variation of the pulse height of 0.67 **LSB(THDAC)**, which corresponds to approx. 71 e , was found, which shows the excellent long term stability ($\mathcal{O}(10\text{ h})$) of the laser system.

The following fit function was used to extract the pulse height from the counter data:

$$\text{Counts}(x) = 1/2(\text{erf}(\frac{p_1 - x}{p_2})) - \text{erf}(\frac{p_3 - x}{p_4}) + p_5\mathcal{N}(x, p_6, p_7), \quad (9.10)$$

where x denotes the **THDAC** value. The fit function is the difference of two error functions with mean p_1 and p_3 and width p_2 and p_4 added to a Gaussian with mean p_6 , and width p_7 . In this model the single channel pulse detection

efficiency is fixed at 1 in order to obtain more robust results. The obtained pulse shape of the falling edge of the signal reconstructed with fit result from the difference of $(p_3 - p_6)$ as a function of the delay is shown in figure 9.9a.

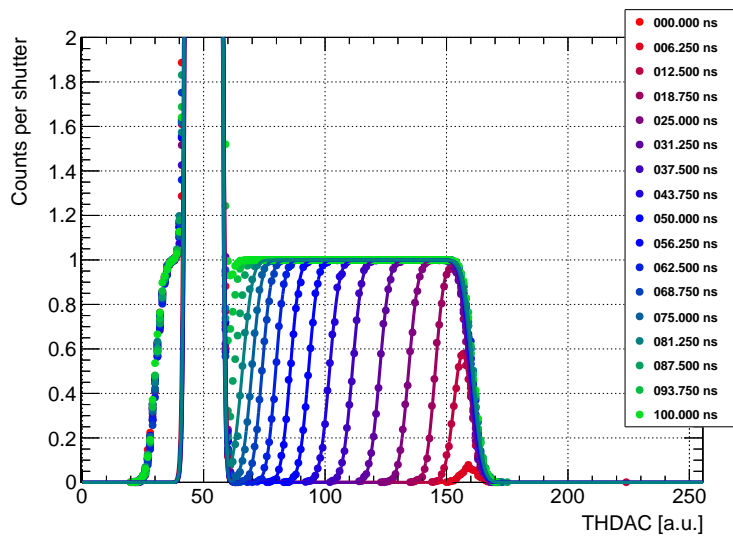


Figure 9.7: Shows the counter contents for the synchronized laser tests, with the pedestal peak out of scale, for different delay settings. In case the algorithm finds rising and falling edge over noise, the line indicates the fit function.

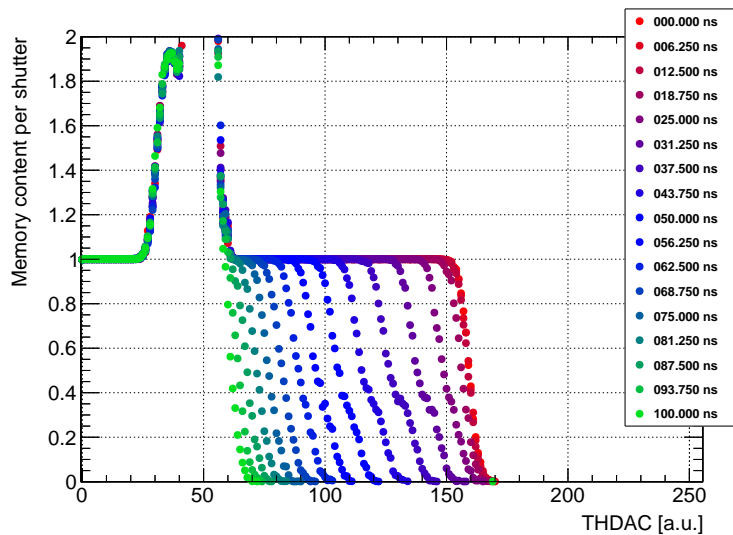


Figure 9.8: The content of 96 memory cells for the synchronized laser tests. The data was taken simultaneously with counters (see figure 9.7).

For pulse shape reconstruction of the rising edge of the pulse a similar reasoning is possible. However the technique relies on the no-processing mode (see section 6.2.3, figure 6.10) readout, which works slightly different. An edge detector detects the rising edge of the signal, if the shutter is open. If a single channel fires, the binary hit information for all channels is written with a time-stamp counting in 25 ns intervals to one of the 96 memory cells. In this version of the **MPA-light** chip a 3.125 ns strobe signal resets the edge detector every clock cycle, which prevents the edge detector to change state and dead time is introduced. The data in figure 9.8 shows, that a laser pulse is detected efficiently with full pulse height at 0 ns. Considering, that in the counter data no pulse is detected at all, even, if the full rising edge is detected, there must be an additional delay in the chip logic, between the two data paths. For increasing delay however the dead time window changes the phase, which leads to additional kinks in the s-curves. With proper synchronization the dead time effects are not seen in the maximum value of efficiency, which is exactly 1. However the shape of the s-curves is affected, because the change of state of the edge detector happens at different phases. In case the dead time window is hit, but the shutter is not yet closed, the edge detector may change state delayed, which results in a kink in the s-curve.

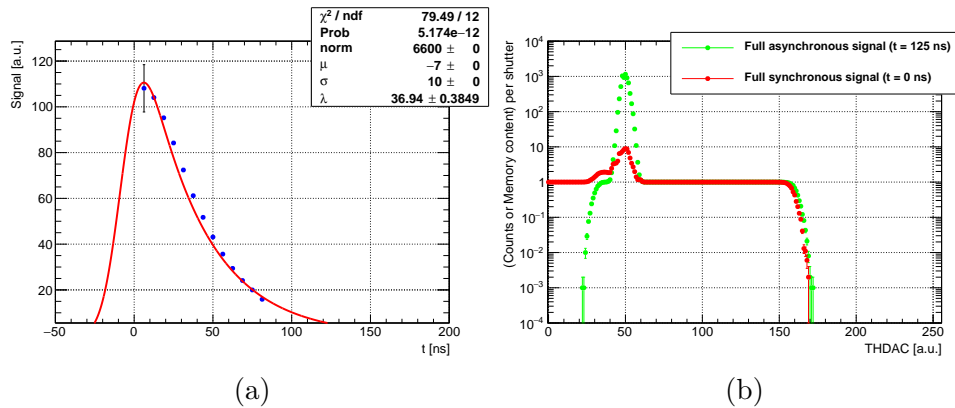


Figure 9.9: The reconstructed pedestal subtracted pulse shape from the curve fits to the counter data. The fit function is to guide the eye and indicates the rising edge of the signal, with time constants given in the **MPA-light** specifications (a). (b) The comparison of counter and memory data

Due to the time difference in the data path, synchronous and asynchronous signal are compared for different delays, such that the real pulse height is

measured (see figure 9.9b). The no-processing mode data is the superposition of all 96 memory cells for the selected channel. The no-processing mode noise peak has a different shape, because unlike in the ripple counters, only rising or falling edges are detected and every acquisition cycle an edge detector reset is performed, which is different from the Schmidt trigger like behaviour of the ripple counter data. The no-processing mode noise peak is much smaller, due to the synchronization of the discriminated signal with the system clock, which is similar to a low pass filter. In the signal shape, however, no differences were observed between the two different readout modes.

9.4 Summary

The measurements with short infrared laser pulses were conducted for the inverted **MaPSA** prototype. The detector shows good position sensitivity and very low crosstalk in the regular region of the sensor. Excellent electronic efficiency of 1 is found, if the laser pulses are synchronized with the chip system clock in a certain clock phase interval. No other reason for inefficiencies, than the dead time of the edge detector, were found, which additionally causes deviation from the ideal s-curve behaviour. The observed width of the charge-cloud is close to the expected value, caused by drift and diffusion only. The observed channel-to-channel variation in the detector response is well explained by gain variations according to the specifications of the readout chip. A method to reconstruct the analog pulse shape in a binary readout chip was developed, which may facilitate future studies on the efficiency of the stub correlation logic possibly with two side illumination of the full **PS** module.

Chapter 10

Test Beams at the DESY-II Synchrotron

The performance of the **Inverted MaPSA** prototype module is characterized at DESY-II synchrotron with a particle beam of 5.6 GeV electrons. The DESY-II synchrotron electron bunches interact with a carbon fiber and generate Bremsstrahlung photons with a broad energy spectrum as shown in figure 10.1. A converter target is used to generate $e^- e^+$ pairs. A dipole magnet and a collimator allow the selection of the particle energy and the particle type, electrons in this case.

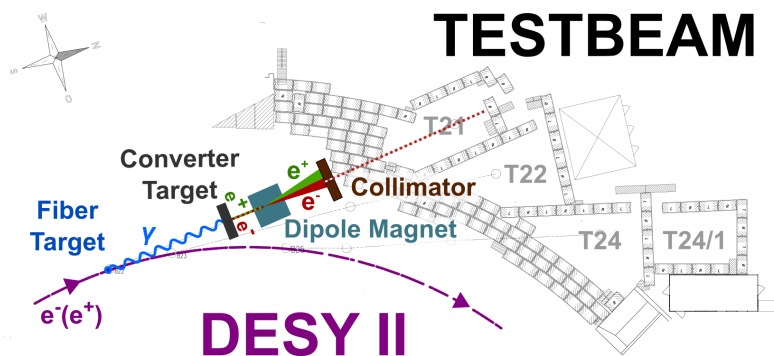


Figure 10.1: The beam generation at DESY from [94]. Gammas originating from a fiber target produce $e^- e^+$ pairs in a converter target. Particle energy selection via magnet and collimator is possible.

10.1 Test Beam Setup, Trigger and DAQ

For the characterization of the **Device Under Test (DUT)** the EUDET telescope [95, 96] is used, which combines three **Minimum Ionizing MOS Active pixel sensor (MIMOSA)** planes in two triplets and one timing reference plane. The reference is necessary due to the rolling shutter readout of the **MIMOSA** sensors, which have an integration time of $115.2\mu\text{s}$. A picture and a schematic of the setup is shown in figures 10.2 and 10.3.

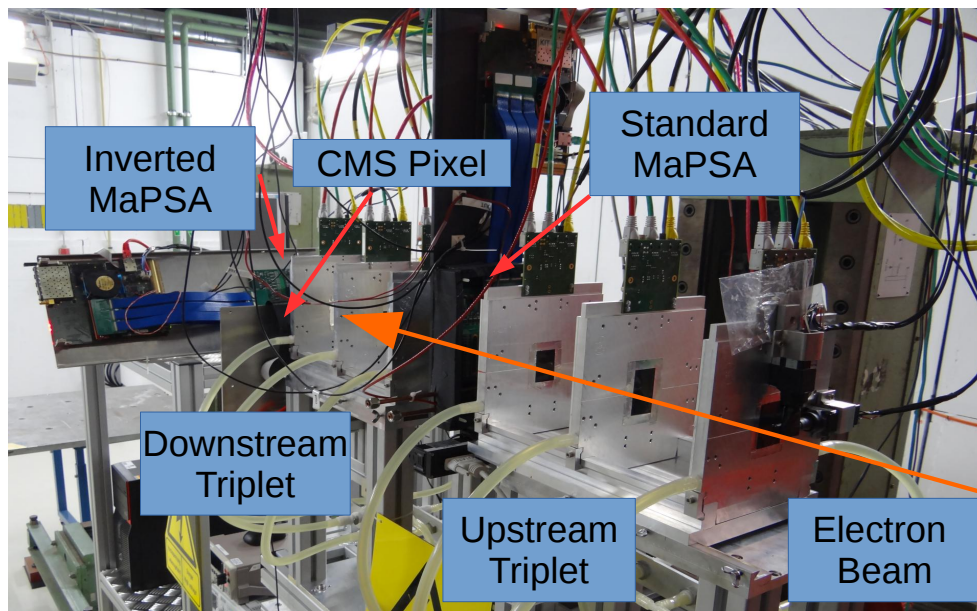


Figure 10.2: The setup during the TB at DESY has 6 **MIMOSA** planes, the CMS timing reference plane, one **MaPSA-Light** and one **Inverted MaPSA-light**.

For triggering purpose a scintillator cross is placed upstream and another cross placed downstream after the last **MIMOSA** plane. Upstream and downstream refers to the position near and far from the collimator. The z-positions and fundamental detector data of all planes in the setup are shown in table 10.1.

Different fixtures for the **DUTs** were used. For the standard **MaPSA-Light** the fixture has an additional copper block and allows cooling of the chips, in case irradiated sensors are investigated. In this work only, the data from the

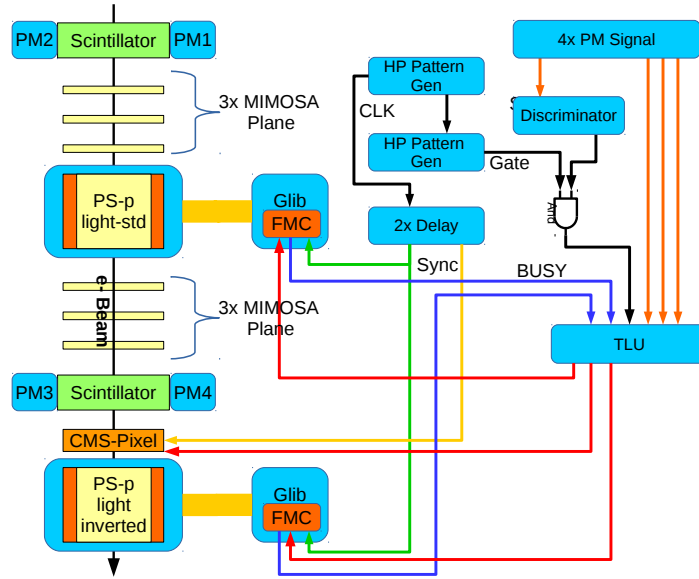


Figure 10.3: The schematic of the setup with trigger and busy logic and clock synchronization scheme. The trigger signal in red is omitted for the **MIMOSA** planes. In green and orange is the 40 MHz clock signal with different delay for CMS-pixel and **DUT**. In blue the busy signal is shown.

inverted **MaPSA-Light** is presented, which is in the following referred to as the **DUT**.

The trigger window of about $10 \text{ mm} \times 10 \text{ mm}$ is realized as a cross of two optically insulated, 6 mm thick scintillators, one in front of the **MIMOSA** upstream triplet, and one between the downstream triplet and CMS reference plane. The BC-408 scintillator Polyvinyltoluene base material has a radiation length of 42.54 cm. In addition the scintillator modules comprise vinyl tape for optical insulation and a PET radiant light film, of a thickness of 0.42 mm with a radiation length of 19.63 cm. In total, four photomultipliers are used, which produce a coincident signal, if a track passes through all telescope planes.

In the following more details about the trigger and data acquisition system of telescope and **DUT** are given. A configurable **Trigger/Timing Logic Unit (TLU)** is responsible for the trigger and busy logic [97].

For synchronization purpose a pattern generator generating a 40 MHz clock is used to drive the CMS timing reference plane and the **MPA-light**. The

trigger is given by the coincidence of the three discriminated photomultiplier signals and the coincidence of a fourth photomultiplier signal with a clock-synchronous 10 ns gate, which is generated by a second synchronized HP pattern generator. This is necessary to achieve good efficiency in the CMS-reference plane and provides a possibility to test the synchronous readout of the **MPA-light**. This technique should optimize the phase-dependent efficiency of the CMS-reference plane and possibly avoid the dead time in the synchronous data acquisition of the **MPA-light**.

The **MPA-light** uses the inverted shutter signal, for the realization of a busy logic, which is necessary to synchronize all subsystems. The inverted shutter signal is generated in the **FPGA** of the **GLIB** and mirrors the state of the data acquisition cycle of the test board. The busy logic inhibits further triggers, if one of the subsystems is currently readout. Ideally the busy logic ensures, that the number of triggers accepted by each of the three different subsystems matches exactly and, that the three independent datastreams have constant shift with respect to each other. This is also referred as simple handshake mode.

The **MPA-light** interfaces to the **GLIB**, which is connected to a DAQ-PC. The IP-Bus protocol is used to communicate with the **GLIB**. Upon arrival of a trigger, the **MPA** shutter is closed for 0.446 ms during the readout of the **MPA**. The total delay of the trigger is greater than the decay time of the analog signal (see section 9.3), which ensures that the counters detect the pulse. The same shutter signal is used as busy signal. This readout mode is chosen to be able use the asynchronous counter data for tracking, with the expectation to observe in maximum one particle hit in one pixel during one acquisition cycle. A busy signal is only necessary for the **DUTs**, for being the slowest system readout. The timing of all signals important for the trigger gating and busy logic for one acquisition cycle are depicted in figure 10.4. Coincidence to **TLU** refers to the signal generated by an external coincidence logic from one of the photomultiplier signal and the gate signal (see figure 10.3). The signal is a prototype for the trigger signal, which is generated, when a four-fold coincidence together with the three other photo-

multipliers is detected in the **TLU**. The signal length of 100 ns ensures, that the busy signal is asserted at **TLU**, before the trigger signal drops.



Figure 10.4: The timing of signals important for the trigger gating and busy logic used throughout the test beam. CLK refers to the 40 MHz clock. The coincidence to **TLU** signal is used with the coincidence of three other PMs to provide the trigger.

The **MIMOSA** 26 sensors are produced in AMS 350 nm CMOS technology [98]. The sensors have pixel of size $18.4\ \mu\text{m} \times 18.4\ \mu\text{m}$ in 1152 columns and 576 rows. The sensors have a quoted thickness of $50\ \mu\text{m}$ and cover an active area of $21.1\ \text{mm} \times 10.6\ \text{mm}$. The intrinsic telescope plane resolution at the used threshold setting of 6 times the noise **RMS** is quoted to be $\sigma_{tel} = 3.4\ \mu\text{m}$ [95]. $25\ \mu\text{m}$ thin kapton foils ensure light-tight enclosure of the **MIMOSA** sensors.

The sensor currents were monitor throughout the data taking period with a Keithley 2410 **SMU**. A PT-100 sensor was used to measure the temperature in the vicinity of the assembly and showed constant readings around $22\ ^\circ\text{C}$. Around 54 GB of telescope data and 1 GB of **DUT** data were recorded.

Table 10.1: The fundamental specifications of the telescope setup. The data includes the z-position, the thickness of the scatterers in units of radiation length as used in **General Broken Lines (GBL)** track model, the active sensor area, the pixel geometry and the specified intrinsic resolution. For the alignment procedure all planes are considered. Final track reconstruction and pull analysis is performed with plane 4 to 8. The standard **MaPSA** module has a 4 layers of $35\ \mu\text{m}$ copper in the carrier PCB. The carrier PCB has no cutout and therefore additional scattering material is introduced. The total material budget includes the air volume between the planes.

| Plane No. | Type | z Position [mm] | $x_i/X_0 = \epsilon_i$ 1×10^{-3} | ϵ_i/ϵ 1×10^{-2} | Active Area | | Pixel Pitch | | Intrinsic Resol. | |
|-------------------|---------------------|--------------------|--|---|-------------|-----------|------------------------|------------------------|------------------------|------------------------|
| | | | | | x [mm] | y [mm] | x [μm] | y [μm] | x [μm] | y [μm] |
| 1 | MIMOSA | 0 | 0.76 | 1.44 | 21.2 | 10.6 | 18.4 | 18.4 | 3.4 | 3.4 |
| 2 | MIMOSA | 150 | 0.76 | 1.44 | 21.2 | 10.6 | 18.4 | 18.4 | 3.4 | 3.4 |
| 3 | MIMOSA | 305 | 0.76 | 1.44 | 21.2 | 10.6 | 18.4 | 18.4 | 3.4 | 3.4 |
| - | Std. MaPSA/PCB | 386 | 23.11 | 43.74 | - | - | - | - | - | - |
| 4 | MIMOSA | 503 | 0.76 | 1.44 | 21.2 | 10.6 | 18.4 | 18.4 | 3.4 | 3.4 |
| 5 | MIMOSA | 655 | 0.76 | 1.44 | 21.2 | 10.6 | 18.4 | 18.4 | 3.4 | 3.4 |
| 6 | MIMOSA | 808 | 0.76 | 1.44 | 21.2 | 10.6 | 18.4 | 18.4 | 3.4 | 3.4 |
| - | Scintillator | 811.5 | 14.11 | 26.71 | 10.0 | 10.0 | - | - | - | - |
| 7 | CMS Pixel Reference | 815 | 5.49 | 10.39 | 7.8 | 8 | 150 | 100 | 43.3 | 28.9 |
| 8 | Inverted MaPSA | 825 | 2.83 | 5.36 | 1.8 | 9.3 | 100 | 1446 | 28.9 | 417.4 |
| Total Mat. Budget | | | 52.84 | | | | | | | |

10.2 Offline data analysis

In the following data processing and data quality cuts for the data of the **MaPSA-Light** prototype module, CMS reference and telescope are introduced. The available processed **MPA-light** raw data acquired during the test, comprises the ripple counter data, with a dedicated deserialization rule and of the no-processing mode data. A detailed description of the data format is given in [99]. A general overview of the complete analysis chain is shown in figure 10.5. The single processing steps for the different subsystems are deserialization, clustering, assignment of hit in a global coordinate system, datastream realignment, alignment and track fit, in order to finally produce the analysis results.

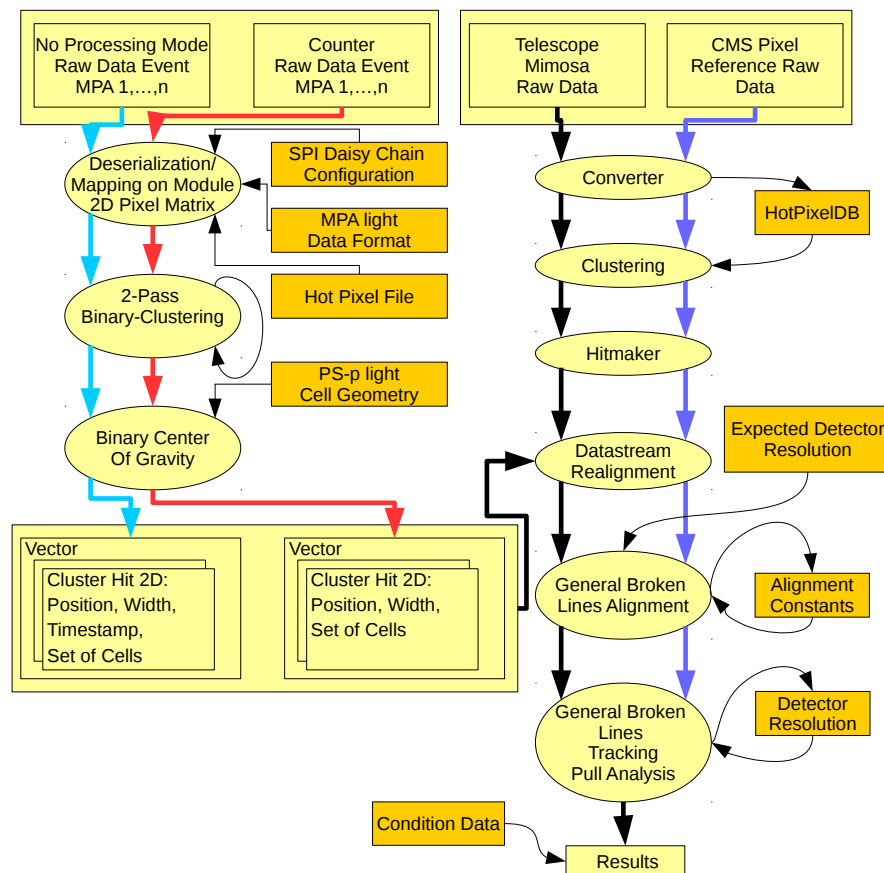


Figure 10.5: The complete analysis chain for the Testbeam data with all processor steps and the necessary additional alignment and geometry constants included.

10.2.1 Clustering and hit generation

The signal of an ionizing particle is possibly shared among several adjacent pixels, which is either due to the incident angle of the particle, delta electrons, Lorentz drift and diffusion or by resistive or capacitive effects. Clustering refers to the procedure of grouping the pixels together. For each cluster, a first estimator of the real particle impact point is interpolated. In the following the clustering procedure for the **MPA-light** is described in detail. For the telescope data and the CMS-pixel reference data the existing EU-Telescope framework with the sparse clustering procedure requiring adjacent pixel above a preset threshold was used [100]. However for the CMS-pixel reference only binary hit information is used, limiting the obtained position resolution.

For readout chips with binary readout, such as the **MPA-light**, no sophisticated algorithms like center-of-gravity method (described in [101]) are possible to improve the impact point estimate. Instead binary readout allows high readout rates and further on-chip data reduction maintaining an acceptable power consumption of the chip.

In the applied offline clustering procedure, the deserialized event of the **MPA-light** chips is mapped to a 2D pixel frame on module-level. For this it is necessary to account for the position of the chip on the module and the internal ordering of the MPA-light data. Additional offline pixel masking is achieved via a configuration file, however in this particular inverted MaPSA module there was no necessity to do so. Masking suppresses noisy pixels, which could have effect on the cluster width distributions and position resolution.

The masked, reordered and mapped binary data is clustered with a binary, two pass connected components labeling [102] algorithm. The algorithm uses 8-connectivity. This means a cluster is formed by horizontal, vertical and diagonal connection of firing pixels and distinct clusters do not have any neighbouring pixels.

For a recognized cluster the binary center of gravity $\mathbf{r}_{\text{Cluster}}$ is produced in the local frame of reference, using the cell position \mathbf{r}_i , the corresponding cell type area A_i as weighting factor and the total cluster area A_{tot}

$$\mathbf{r}_{\text{Cluster}} = \frac{1}{A_{\text{tot}}} \sum_i A_i \mathbf{r}_i \quad . \quad (10.1)$$

This binary center-of-gravity algorithm is slightly different from the so called centroid extraction method, which is used in the on-chip, real time data sparsification logic, which does not account for the different cell geometries. In the offline analysis for each cluster a bit mask is used to store additional information on position of the involved pixels and pixel geometry according to table 6.1, for subsequent analysis. E.g. this allows to differentiate clusters with edge or corner pixel from clusters with regular cells only.

The set of positions for the clustering with half-strip resolution is discrete by construction (see figure 10.6). This procedure improves slightly the position resolution with respect to a binary 1-strip resolution [41, chap. 8.1]. Assuming equal weight for each pixel, for even cluster width the position is always in between the two pixel, while for odd cluster the cluster hit position is assigned to an integer strip coordinate. Consequently, in the online zero-suppression of the readout chip in the region with regular cells, one additional bit with half-strip information is sufficient to cover all cases without loss of precision. The full binary cluster hit contains the pixel coordinates in half strip resolution and the cluster width. In the **MPA** the reserved number of bits for the transmission of the cluster size is reduced by rejection of wide clusters, which correspond to particles with low p_T or common mode noise. In the clusterwidth distribution for a sensor with 100 μm pitch a steep drop is expected for increasing clusterwidth. In the **MPA** the cut on the clusterwidth in x is adjustable for achieving a homogeneous p_T discrimination. The long edge of the macro-pixel is about 1.4 mm and therefore the rejection of clusters sizes greater two [66, chap. 4.6] is sensible. Figure 10.6 shows an example for the map of reconstructed on-track cluster hit positions in the local frame of reference of the module. The dark spots correspond to clustersize odd, while the light spots correspond to clustersize even.

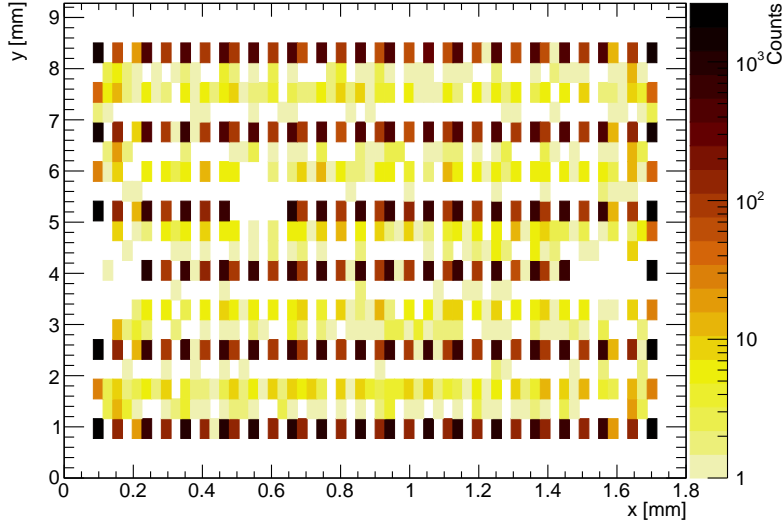


Figure 10.6: The reconstructed discrete hit positions after clustering for on-track hits in the **MaPSA** frame of reference. Binary readout prefers hit positions at the cell center and the intermediate hit positions are naturally suppressed. The data in this plot contains three pixels, which are masked due to calibration issues. The data was acquired at $\mathbf{THDAC} = 100$, $V_b = 100$ V with 5.6 GeV electrons with the beam perpendicular to the sensor.

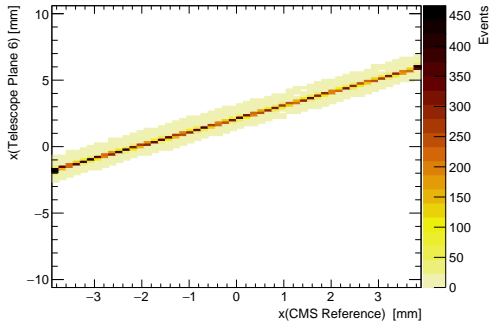
Merging of the data streams

Three different data streams from telescope, inverted **MaPSA-Light**, and CMS-timing reference planes were recorded with the simple handshake mode. Due to electronic noise not all subsystems register the trigger correctly and in 1×10^6 events about 0 to 5 times either triggers are omitted or noise causes an event in the CMS reference plane with extreme high occupancy. These type of events are usually caused by beam-background in the **LHC** and result in a timeout in the **DAQ**. However those events are not expected to occur in the DESY-II electron beam and indicate the high level of noise caused by the surrounding in the electronic systems, such as the chiller, which is responsible for cooling of the telescope. Both effects result in desynchronization of the datastreams.

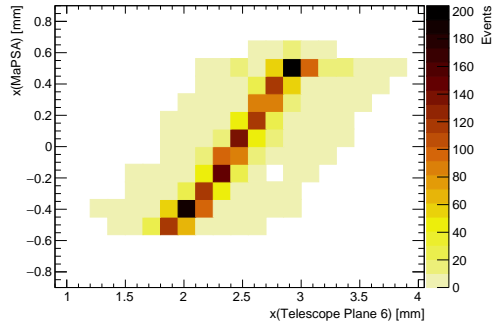
Therefore, in the offline reconstruction the data streams are realigned. The realignment procedure is based on the correlation of the different data streams.

For good signal to noise ratio a statistic over 1000 events are aggregated in one run segment to scan the shifts of the data streams as shown in figures 10.7c and 10.7d. A bin is filled, correlating spatially in x and y the reconstructed hits in the **MaPSA** module with the hits in the last telescope plane and the hits in the CMS-Reference plane as shown in figures 10.7a and 10.7b. The expected mean number of spatially correlated hits in two coordinates drops, if the shift of the data stream changes. However there is a small background due to noisy pixels. For realignment the correct shift is determined by the searching for the bin with the highest signal over a predetermined threshold times the median of the bin contents from the same run segment, which is a robust outlier detection mechanism. Finally, when a discontinuity in the shift is detected from run segment i to run segment $i + 1$ the events in run segments i and $i + 1$ are excluded for further analysis.

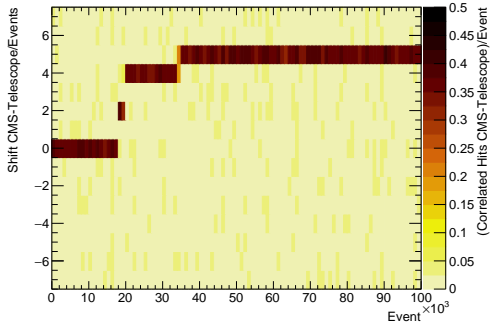
This method allows to detect and correct changes in the shift of the data streams. However it requires a medium to good overall detector efficiency in order to work reliable and assumes seldom occurrence of the shifts. The number of hits per event in the correlation of CMS reference plane and the telescope plane is less than 0.4, which is a result of geometrical acceptance and the imperfections in the trigger gating technique. The mean number of hits in the correlation on **MaPSA** and telescope plane 6 is not exceeding a few percent, which is mainly due to the small active area and the missing possibility to restrict the trigger area to the active area by the time of data taking. This affects the alignment of the **DUT** and the measurement precision.



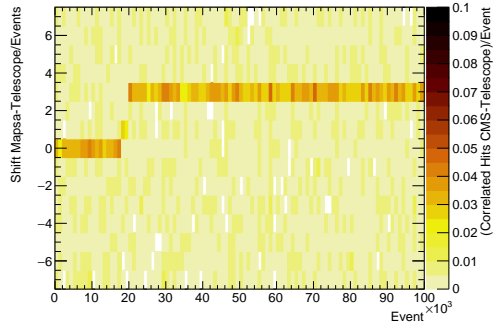
(a) The correlation for the x-coordinates of telescope plane 6 and the CMS reference plane hits at fixed shift of 5 Events.



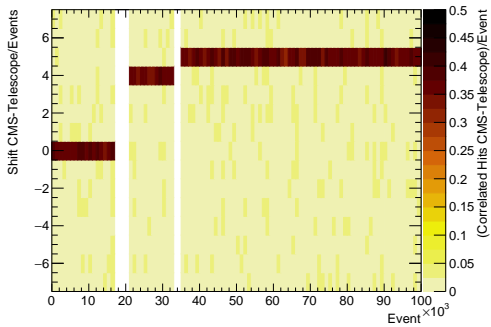
(b) The correlation for the x-coordinates of the telescope plane 6 and the inverted MaPSA hits excluding the noisy edge pixel of the MaPSA.



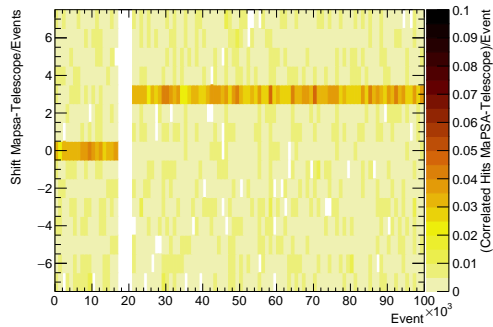
(c) The mean number of hits in the correlation CMS Reference and telescope plane 6 per event for different shifts in the data streams.



(d) The mean number of hits in the correlation for the inverted MaPSA and the telescope plane 6 per event for different shifts in the data streams.



(e) The correlation plot CMS-reference with telescope plane 6 with the data quality cuts applied.



(f) The correlation plot inverted MaPSA with telescope plane 6 with the data quality cuts applied.

Figure 10.7: (a-f) The method of realigning the data streams for a run with 1×10^6 events. Note the different z-axis range for the plots containing MaPSA data.

10.2.2 Pattern recognition and tracking

Pattern recognition and tracking refers to the reconstruction of the particle trajectory. One simple algorithm applied in tracking is the triplet method. A triplet is formed in three detector layers, if for a combination of hits in the two outer layers a compatible hit in the middle layer is found. Compatible means the triplet residual of the interpolated hit position \mathbf{r}_{int} with the measured hit position \mathbf{r}_{meas}

$$|\Delta\mathbf{r}| = \mathbf{r}_{\text{int}} - \mathbf{r}_{\text{meas}} \quad (10.2)$$

is in the range allowed by the detector resolution and expected multiple scattering. One additional criterion for construction of a valid triplet is the allowed track slope. The cut is constrained by the assumption, that the tracks originate from the beam axis and by the amount of scattering material, which leads to deflection of the particle. In this analysis two triplets are built by hits from the six telescope planes, one triplet by hits from telescope plane 5, 6 and the CMS reference plane and one additional triplet built in the telescope plane 5, 6 and the **MPA-light**.

A track candidate is formed by merging one or more triplets and a fit with a sophisticated algorithm is performed. In this analysis for reasons of simplicity only tracks with exactly one reconstructed triplet in the upstream and downstream telescope arm and exactly one hit in the DUT Plane and CMS reference plane are used. This reduces the effects from combinatorial background to a minimum. Only for global alignment the upstream telescope triplet is also included. For track fitting and alignment the **GBL** method is used [103, 104], which has several advantages with respect to other methods such as the Kalman filter or a simple straight line fit. The track model accounts for the possibility of the deflection of the particle in scattering material due to **MCS** and improves the precision of the fit especially for medium and low-energy beam lines, like DESY-II test beam [95]. The variance θ_0 of the distribution of the scattering angles is well described by the Highland formula [105]

$$\theta_0 = \frac{13.6 \text{ MeV } c_0^{-1}}{p\beta} z\sqrt{\epsilon}(1 + 0.038 \ln \epsilon) \quad , \quad (10.3)$$

which accounts for the particle momentum p , β , and the thickness of the scattering material in units of the radiation length $\epsilon = \frac{x}{X_0}$. For a **GBL** fit the variance of the single scatterer ϵ_i is distributed along the individual scatterers

$$\theta_{0,i}^2 = \frac{\epsilon_i}{\epsilon} \theta_0^2 = \left(\frac{13.6 \text{ MeV } c_0^{-1}}{p\beta} z \right)^2 \epsilon_i (1 + 0.038 \ln(\epsilon))^2 \quad , \quad (10.4)$$

as given in [95].

For this analysis a flexible, configurable implementation of an arbitrary material slab was developed in order to use the **GBL** fit for the non-standard telescope configuration and more complicated scattering layer stacks, such as a multi-layer PCB.

The figure of merit of the telescope is the biased track resolution $\sigma_{t,b}(\sigma_{t,u})$. The biased residual width $r_b^2(z)$ is the standard deviation of the distance between the measured hit and the track fit and is defined as

$$r_b^2(z) = \sigma_{int}^2(z) - \sigma_{t,b}^2(z) \quad , \quad (10.5)$$

where $\sigma_{int}(z)$ is the intrinsic resolution of the detector at position z . In addition, the biased pull of a track is given by the ratio of the biased residual over the predicted residual width,

$$pull_b = p_b = \frac{r_b}{\sqrt{\sigma_{int}^2(z) - \sigma_{t,b}^2(z)}} \quad . \quad (10.6)$$

For correct inputs regarding the variance of the scattering angles and the intrinsic resolutions and track resolution the distribution of p_b follows a normal distribution $N(0, 1)$.

The result of a track fit with NDF degrees of freedom is characterized by the value χ . From the set of all tracks the distribution for the probability of the observed χ^2 to exceed the value of $\langle \chi^2 \rangle$ by chance is obtained. A cut value of 0.01 for this probability is chosen to discriminate tracks, which are badly described by the track model for alignment and tracking. An exemplary fit probability distribution as obtained after the final track fit iteration is shown

in figure 10.8a. The obtained distribution is similar to distributions obtained in previous analysis, where this particular telescope plane spacing was used.

10.2.3 Alignment

The general principle for the track-based alignment of a particle detector, according to [106], exploits the fact, that for a given track-fit, the quality of the fit worsens for a misaligned detector, e.g. χ^2 increases.

$$\chi^2 = \sum_{\text{Hits on Track}} \left(\frac{\text{Track-To-Hit-Distance}(\mathbf{a})}{\text{Resolution}} \right)^2 \quad (10.7)$$

where \mathbf{a} is a vector with the alignment parameters, which are corrections on the initial measured detector positions. The goal of the alignment procedure is to find the minimum value of χ^2 , as a function of the alignment parameters. However for a single track there are many detector configurations possible, which result in the minimum value of χ^2 . Therefore, averaging over a greater set of tracks is necessary to improve the estimate of the alignment parameters. More formal the alignment equation of the multidimensional χ^2 is given by:

$$\chi^2 = \sum_{\text{Hits}} \left(\frac{m_i(\mathbf{a}) - h_i(\mathbf{a})}{\sigma_{i,\text{int}}} \right)^2, \quad (10.8)$$

where $m_i(\mathbf{a})$ is the measured hit position, $h_i(\mathbf{a})$ is the position of the track fit closest to m_i , \mathbf{a} is the vector of alignment parameters, and $\sigma_{i,\text{int}}$ the intrinsic resolution of the i th detector. The minimization of χ^2 involves the iterative inversion of a $N \times N$ matrix, where N is the number of free alignment parameters, which is performed by dedicated software packages. In this analysis for the alignment of the 6 telescope planes, the CMS reference plane and the inverted **MaPSA-Light** a **GBL** refit in combination with Millepede-II is used [107]. For each telescope plane, shifts in x,y and a rotation around the z-axis are defined as global free parameters. **GBL** is used for the initial track fit with primary resolution estimates, and tracks with a χ^2/NDF value smaller than a predefined cut are fed into Millepede-II, which performs a simultaneous fit of all global alignment parameters and all local track parameters

and the matrix inversion. The alignment of the detectors improves, when the procedure of track refit with **GBL** and solving for the alignment parameters is iterated, simultaneously adjusting the guess on intrinsic resolution and the tightening the χ^2/NDF cut and the cut on the track slopes in the upstream and downstream triplets. The results of the alignment procedure would be distorted by tracks not following the predicted material composition. For the correct treatment, this would require a full 3D-model of the detector material and the calculation of ϵ and ϵ_i for each track. The simplification, used in this work, is to assume, each track passes the same slab of material. Therefore tracks with high scattering angles deflected at the copper block of the module placed in between the two telescope triplets are excluded from analysis. In order to constrain weak modes in the alignment the first and the last plane in the setup are fixed. A weak mode is a coherent detector misalignment, which has physically little or no effect on χ^2 . Formally weak modes correspond to eigenvectors with small eigenvalues in the covariance matrix of the alignment parameters, which is a measure of the uncertainty of the alignment parameters [106]. Furthermore the y-coordinate of the inverted **MaPSA** module is fixed, because in this direction the expected **DUT** position resolution is 0.42 mm for the regular and 0.50 mm for the edge cells for clustersize one in y. However alignment of the **DUT** module in y could in principle be improved using the clusters of size two in y, if enough statistics is available.

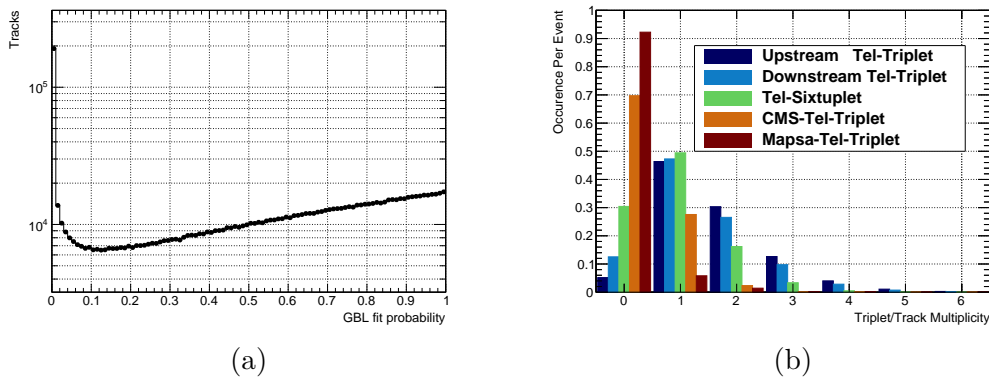


Figure 10.8: (a) GBL-fit probability after alignment and iterative pull analysis for an exemplary run. The tracks not passing the cut at 0.01 are not used for analysis. (b) The triplet-track multiplicity per event.

10.2.4 Iterative pull analysis

In this analysis the biased residual width r_b is determined from the statistical standard deviation of the biased residual distribution. This procedure is preceded by a number of refit iterations, where the predicted intrinsic resolution is adapted according to a correction factor obtained from the Gaussian fit of the pull distribution in the region of one standard deviation around the maximum value. In this way the Gaussian standard deviation of the pull distribution converges to 1 and r_b to the real value. For the first estimate of the r_b an educated guess is necessary.

10.2.5 Measurement of DUT efficiency and noise occupancy

The **DUT** tracking efficiency ϵ (see equation (10.9)) is determined by requiring exactly one downstream telescope triplet and exactly one compatible hit in the CMS-reference plane with a probability of the observed χ^2 exceeding $\langle \chi^2 \rangle$ by chance smaller than 1%. The χ^2 -cut ensures only tracks classified as good including the **DUT** measurement are accepted.

$$\epsilon = \frac{\text{Isolated Track} \in (\text{DUT} \cap \text{CMS Ref.} \cap \text{Downstream Tel. Triplet} \cap \chi^2\text{-Passed})}{\text{Isolated track} \in (\text{CMS Ref.} \cap \text{Downstream Tel. Triplet})} \quad (10.9)$$

Similar the noise occupancy p_{FH} (see equation (10.10)) is defined using the events with exactly one track in telescope and CMS reference plane not pointing to the **DUT** active region and one or more hits in the **DUT**.

$$p_{\text{FH}} = \frac{\text{Iso. Track} \in (\overline{\text{DUT Active Area}}) \cap (\text{CMS Ref.} \cap \text{Tel. Triplet} \cap (\text{Reco Hit DUT}))}{\text{Iso. Track} \in (\overline{\text{DUT Active Area}}) \cap (\text{CMS Ref.} \cap \text{Tel. Triplet})} \quad (10.10)$$

p_{FH} comprises the intrinsic electronic noise from the analog front-end and a digital component mainly from the periphery of the readout chip, which is independent of the **MPA-light** threshold setting.

10.3 Results and conclusion

The results of the test with particles are presented in the following section. In table 10.2 the final result of alignment and measurement of the position resolution of all planes is shown. The corresponding distributions are found in figures 10.9 and 10.10. It is remarkable, that despite the correct implementation of the scattering material in the **GBL** fit the predicted intrinsic resolution for the telescope planes after the final iteration of the pull analysis is underestimated. This behavior was observed before, and a tuning parameter $\kappa(E)$ depending on the incident particle energy was proposed in [95], which is not applied in this analysis. Deviations from the ideal **GBL** track model occur for the telescope configuration with the large 150 mm plane spacing, at low energies or for high amount of scattering material.

The achieved width of the biased residual distribution at the inverted **MaPSA** is perfectly explained by **MCS** in the downstream scintillator cross and CMS reference plane. Only for the scintillator scatterer $\epsilon_{\text{scint}} = 0.0141$. At the DUT distance of 13.5 cm from the scintillator the expected standard deviation of the distribution of deflection is at least 46 μm . Taking this contribution into account the upper limit for the position resolution of the inverted **MaPSA** in x and in y is in accordance with the theoretically expected value of $p_x/\sqrt{12} = 28.9 \mu\text{m}$ and $p_y/\sqrt{12} = 417 \mu\text{m}$ (see figure 10.10).

$\mathcal{O}(0.1 \mu\text{m})$ alignment precision is achieved for the telescope planes 4,5,6, however for the **DUT** the quality of alignment is affected by low statistics and **MCS**.

The measurement of the **DUT** efficiency is biased by the extrapolation of the tracks. Due to the **MCS** a significant amount of reconstructed telescope tracks at the edges of the region of interest do not hit the **DUT**, which results in a lower measured efficiency. Due to **MCS** inefficient structures inside the active area of the **DUT** are not resolved. In figure 10.11a the **DUT** efficiency according to section 10.2.5 as a function of the extrapolated track position in the **DUT** plane is shown. The inefficiency in the **DUT** region is caused by a pixel, which was switched off due to calibration problems. Outside the **DUT** region a background is visible, which is caused by noisy pixel in both

Table 10.2: The table shows the measured width of the pull distribution from a Gaussian fit in an interval of one standard deviation around the peak, the predicted residuals used as input for the **GBL** fit, the **RMS** width of the biased residual distributions, all after the final iteration of the iterative pull analysis.

| Plane No. | Pull | | Pred. Res. | | RMS Biased Track Res. | |
|-----------|---------------------------|---------------------------|----------------------------------|----------------------------------|--------------------------------|--------------------------------|
| | $p_{b,x}$ [σ] | $p_{b,y}$ [σ] | $r_{int,x}$ [μm] | $r_{int,y}$ [μm] | $r_{b,x}$ [μm] | $r_{b,y}$ [μm] |
| 4 | 0.96 | 0.95 | 2.8 | 3.2 | 1.3 | 1.5 |
| 5 | 0.96 | 0.95 | 3.1 | 3.1 | 2.1 | 2.1 |
| 6 | 0.95 | 0.95 | 3.7 | 3.2 | 1.8 | 1.7 |
| 7 | 0.99 | 1.00 | 58.5 | 41.4 | 63.3 | 54.4 |
| 8 | 1.00 | 1.8 | 89.3 | 444 | 96.7 | 448 |

DUT and CMS reference plane. In the region of interest on the **DUT** (see figure 10.11b) an efficiency of $\epsilon_{\text{DUT}} = .959_{-0.002}^{+0.001}(\text{stat})$ is measured at 95 % confidence level of the Clopper-Pearson interval at a **THDAC** threshold setting of 90, which corresponds to approximately $4.15 \times 10^3 e$.

According to the [18] the collisional stopping power in silicon for 5.6 GeV electrons is $2.231 \text{ MeV cm}^2 \text{ g}^{-1}$ ($1.34 \times dE/dx|_{\text{min}}$, see 3.1), which is equivalent to an expected mean value of 28.5×10^3 **EHPs** in the **PS-p light** sensor. However the available dynamic range of the **MPA-light** readout chip is limited by design to a maximum of $27.2 \times 10^3 e$ and by the achievable pedestal value after calibration, which in this case reduces the total available dynamic range of the readout chip to $21.6 \times 10^3 e$. Therefore a flat efficiency curve is expected for a threshold scan covering the full dynamic range. The observed efficiency together with the fake rate, depending on the **MPA-light** threshold is shown in figure 10.11c. Only at the very high threshold values a slight drop in efficiency is observed, which demonstrates the good charge collection efficiency for the inverted **MaPSA** module. The fake hit rate as defined in section 10.2.5 shows little dependency on the applied threshold. Due to the special readout mode used during the beam test, which is similar to a rolling shutter readout, nevertheless, the fake hit rate is a function of the trigger rate, which explains the small fluctuations. The measured trigger rate was about $\mathcal{O}(500 \text{ Hz})$, resulting in a integration time of $\langle t_{\text{shutter}} \rangle = 1.5 \text{ ms}$, but

the beam conditions were not fully constant during the period of data taking. The small influence of the threshold on the fake rate indicates a correlated noise phenomenon in the digital part of the chip. However this behavior was observed during module pretests and tests with the laser system both for the inverted and the standard module prototypes. In the experiment less than 100 ns integration time are expected and therefore the real fake hit rate is expected to be far lower.

The clustersize distribution as shown in figure 10.11d is sensitive to distortions due to correlated noise. For increasing clustersize a steep drop in the observed frequency is expected. On-track clustersize distribution and total clustersize distribution are only slightly different. This is a hint for low noise and good quality of the inverted module. The green hatched area is the acceptance region of the on-chip data reduction logic for the size of the clusters in y . For vertical incidence of the beam about 0.06% of all tracks will be rejected by the digital logic, for exceeding the cluster size in y .

The on-track mean clustersize as a function of the applied threshold is shown in figure 10.11e. The observed mean value for the clustersize in y is almost constant for the whole threshold range, which is the expected behavior, due to the highly asymmetric cell geometry. In x direction charge-sharing among the adjacent cells is far more probable and in the low threshold regime up to $140 \text{ LSB}_{\text{THDAC}}$ the cluster size strongly decreases. In comparison to pure binary resolution only, the foreseen binary readout with half-strip resolution improves the position resolution only in the region, where the mean clustersize is different from 1. If the clustersize has no dependence from the set threshold value and is different from 1, this would be an indicator for correlated noise in the digital domain.

In total for the inverted module a good efficiency at acceptable fake hit rate is observed. Due to the inevitable large amount of scattering material of the downstream scintillator cross only an upper estimate for the position resolution is obtained. Different factors have negative impact on this analysis. Firstly the trigger window covers a much larger area than the **DUT** active area, which results in lower statistics for a fixed data taking time. In addition, the long cables for the trigger gating technique produce a large amount of

jitter, which leads to reduced trigger efficiency in the CMS-reference plane and in the synchronized data path of the **MPA**. Finally, for a better track pointing resolution, the inverted module should be placed in between the telescope arms.

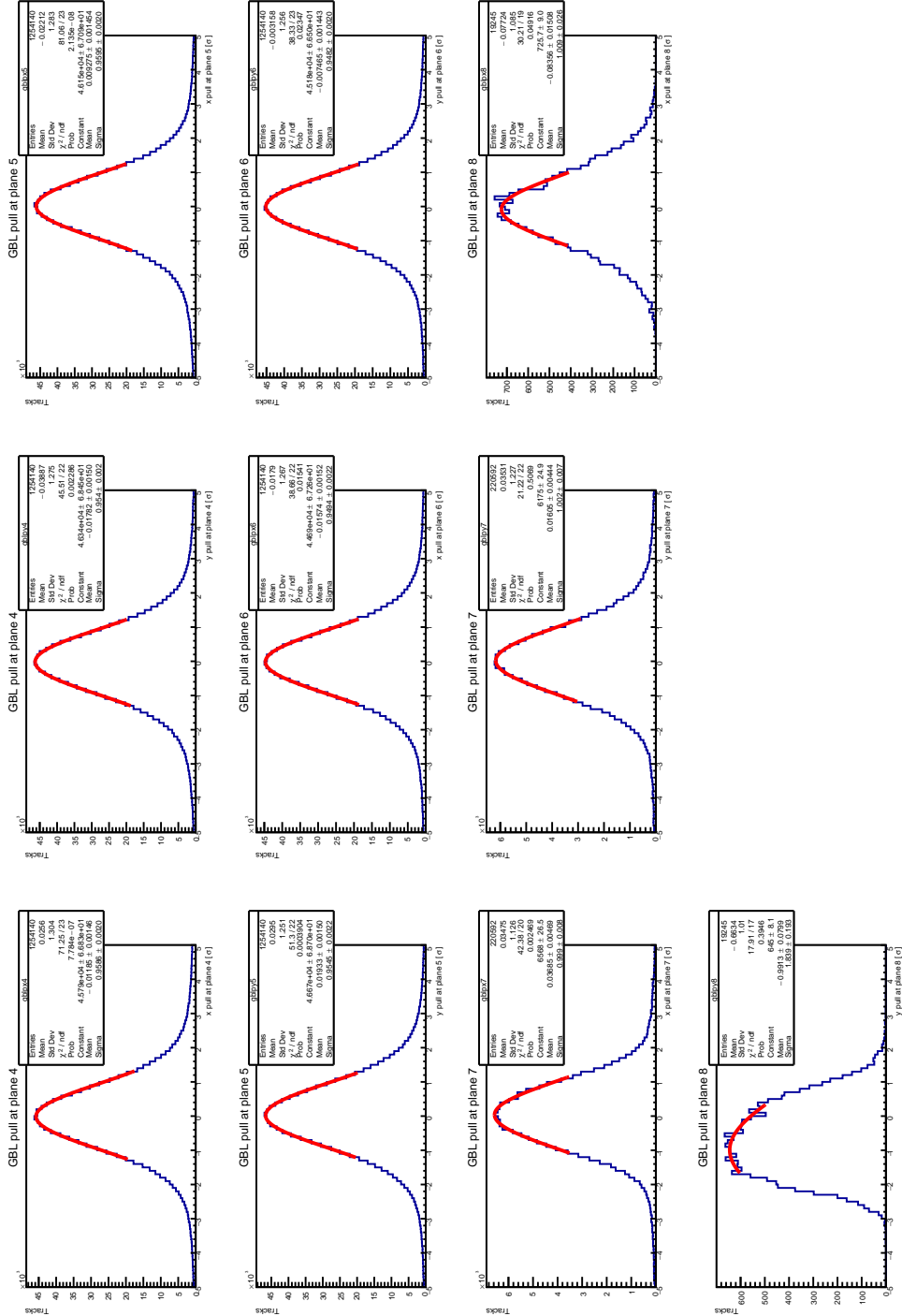


Figure 10.9: The pull distributions the telescope plane 4, 5 and 6, the CMS-Reference plane and the inverted MaPSA.

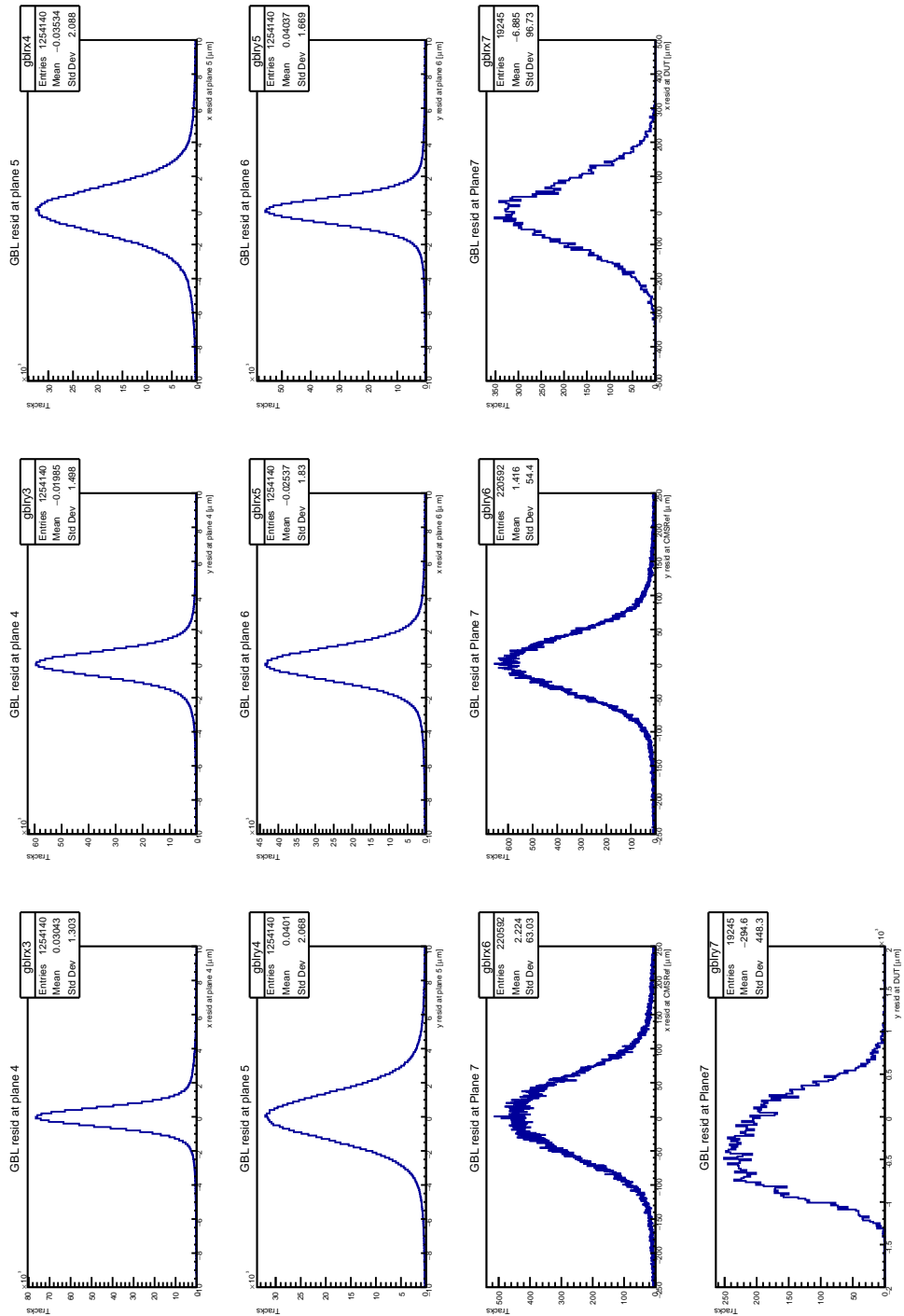


Figure 10.10: The biased residual distributions the telescope plane 4, 5 and 6, the CMS-Reference plane and the inverted MaPSA.

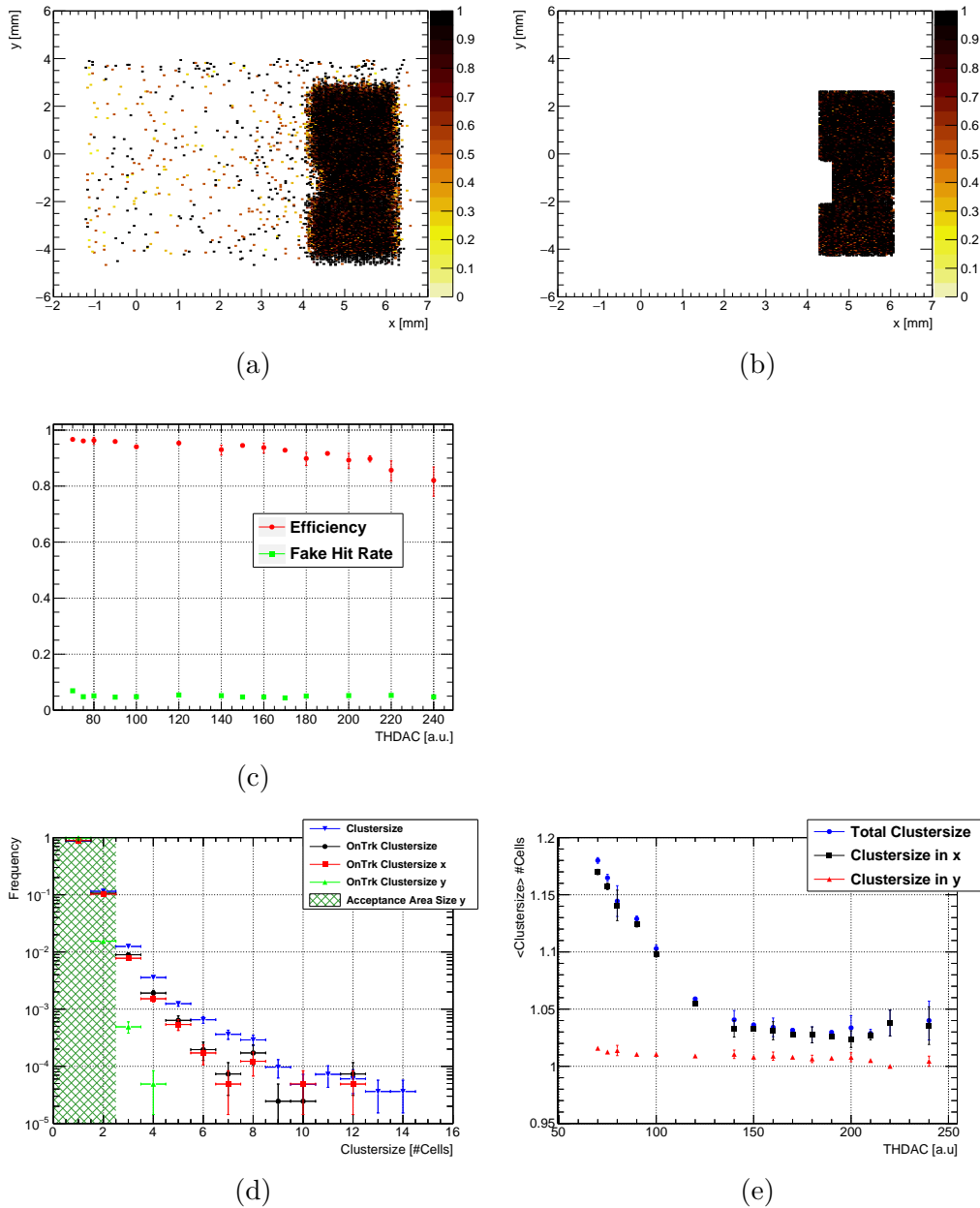


Figure 10.11: (a) The efficiency in the frame of reference of the telescope. (b) The cut applied in order to select a homogeneous region for the efficiency measurement. (c) The efficiency and fake hit rate as a function of the threshold voltage. Statistical error bars are calculated with Clopper-Pearson interval at 95% confidence level. (d) The normalized cluster size distribution for clusters containing regular pixel only at **THDAC** of 90. (e) The mean on-track cluster size depending on the set threshold value.

Chapter 11

Summary and conclusion

This thesis is dedicated to the technology of a tracking detector, which copes with the challenging beam conditions in the **HL-LHC**-era. During the **LS3** of the **LHC**, the **CMS Tracker Detector** will be replaced by a completely new device. Different strategies and options are studied, in order to select the best available silicon sensor technology and module concept. The unique feature of the upgraded tracker is the excellent on-module data reduction and triggering capability, which allows to perform on-module p_T -discrimination at bunch-crossing frequency.

In this thesis the focus is on the prototype sensors of the **PS** module and two different module concepts. The **PS-p** macro-pixel sensors are produced in single sided process and directly connected to the **MPA** readout chips. Furthermore the functionality of the new readout chip from the first prototype run is tested.

The features of four different sensor variants, which mainly differ in the strip isolation properties, are explored and the impact of different edge geometries on the sensor quality is shown. The sensors dark-current dependence on temperature is measured and the characteristic effective energies are extracted. A TCAD simulation complements the understanding of the behaviour of the unirradiated bias dot structure and shows the impact of the different strip isolation techniques on the bias resistor. During the electrical testing of the sensors mainly scratches on the **PTP** structures lead to defective pixels. Elec-

trical measurements on the prototype sensors indicate, that the inter-pixel resistance is slightly too low. However this is attributed mostly to the very high oxide-charge concentration. The punch-through resistor of the bias grid, which is the smallest feature on the sensor, could be slightly increased in size, which would allow a higher sensor production yield. A slightly higher distance of the bias dot n-implant to the pixel n-implant should further increase the off-state resistance and the threshold voltage, with only little impact on the other sensor parameters. The same effect is achieved with increased width of the p-stop implant. This is favourable, because the inter-strip resistance measured on the prototype sensors is in the lower edge of the acceptable region and during irradiation the inter-strip resistance is expected to decrease. Variant 1 and 2 sensors with low p-stop depth and low p-stop concentration have shown the best unirradiated sensor quality, whereas the p-spray variant suffers from strip isolation issues. In general the geometry is susceptible to recoverable charge-up effects, which lead to loss of strip-isolation for variant 1 and 2. Charge-up effects are avoided by the use of ionizing blower and by testing under relative humidity above 20 %.

The **ENC** of two different module types is measured and 237.4 e and 243.8 e is found. The functionality of the prototype modules is demonstrated with tests using a pulsed laser beam. For the synchronous and asynchronous readout modes excellent electronic efficiency is achieved. A dead time introduced by a 3.125 ns reset signal in the digital domain of the chip is identified and a correction will be implemented in the next version of the chip. Good channel-to-channel homogeneity regarding the achieved **ENC** and the detector response is observed. The scan perpendicular to the long side of the macro-pixel shows the pronounced peaks and negligible capacitive coupling of the signal to cells, not hit by the laser beam.

A test with 5.6 GeV electrons at DESY-II complements the performance studies for the inverted module concept. No major drawbacks could be identified regarding the lower limit of the measured efficiency of $\epsilon_{\text{DUT}} = .959^{+.001}_{-.002}(\text{stat})$ and measured upper limit of the position resolution.

The inverted module concept has shown promising results. The advantage of the inverted concept for the p_{T} -modules, are the possibility of direct cooling

of the readout chip. In addition, the high-resistive underfill, which prevents sparking between sensor edge and readout chip in the baseline design, is not necessary in the inverted concept, which reduces the required number of processing steps. The clearance to avoid sparking is achieved more easily in the inverted concept and only a question of the chosen wire bond geometry and eventually wire bond encapsulation. Besides, the requirements for the minimum distance of readout chip and sensor are relaxed and no special bump bonding process is needed. Furthermore, in the **PS** module the flipped design has the advantage, that the backplanes of **PS-p** and **PS-s** sensor face each other, which facilitates the module construction due to vanishing probability of sparking in the region of the high voltage tap, which is the most critical region for the modules with small distance between the sensors.

Due to the need for a fast decision about the module design due to tight time constraints the collaboration has chosen the baseline design over the flipped-one. Nonetheless, the inverted concept may be further pursued in other future silicon trackers, if modules in flip-chip technology are foreseen.

Appendix A

Acknowledgements

The work of this thesis would not have been possible without those, who supported me with fruitful discussions and advice.

Especially I would like to thank my doctoral supervisor Manfred Krammer, my local supervisor, Marco Dragicevic and Thomas Bergauer, who gave me the opportunity to conduct the thesis at HEPHY, for their patience and the trust they placed in me.

Furthermore I would like to thank Axel König, Elias Pree, Victoria Hinger, Dominic Blöch and Peter Paulitsch for their friendship and their support.

I would like to thank Wolfgang Brandner, for the help with the assembly of the laser-setup and all the work that took place during the beam-tests during commissioning.

For the module assembly I am thankful to Andi Bauer for the wire bonding and KIT for providing the bump bonded assemblies. I appreciate the advice from Helmut Steiniger for the deeper insights in the firmware functionality and the discussions with Davide Ceresa, concerning doubts about the readout chip.

My thanks go to my parents and Axel and Regina for your patience and unconditional trust. My gratitude goes to Karen for her support and patience during the work on this thesis.



This project has received funding from the European Union's Horizon 2020 research and innovation programme under grant agreement No 654168

List of Tables

| | | |
|-----|---|----|
| 2.1 | Symbols and constants for the instantaneous luminosity with numbers for the HL-LHC from equation (2.1) | 7 |
| 3.1 | Symbols and constants for the Bethe-Bloch energy loss from [14, p. 441] | 16 |
| 3.2 | Symbols and constants for gaussian beam optics energy [21, chap. 3] | 25 |
| 4.1 | Symbols and constants for equation (4.15) | 33 |
| 4.2 | Material constants for intrinsic silicon at 300 K. | 35 |
| 6.1 | Cell types and geometry parameters for the PS-p-light prototype sensors. | 66 |
| 6.2 | Comparison of the active area to total area ratio for inverted and standard prototype sensor design. | 66 |
| 6.3 | MPA-light specifications from simulation. | 68 |
| 7.1 | Sensor variants for the PS-p light prototypes and their target process parameters. Only measured wafers are presented. | 69 |

| | | |
|-----|--|-----|
| 7.2 | The full depletion voltages extracted from the the intersection of a fit of two linear functions to the $C^{-2}V$ -characteristics and the estimate of the bulk doping concentration extracted using equation (7.9) under the assumption of an area of $A_{eff} = 0.48 \text{ cm}^2$. The values are mean and standard deviation with statistic of 5 sensors per wafer. | 73 |
| 7.3 | Effective energies and errors at $V_b = 130 \text{ V}$ from the fit with the temperature dependent dark current model. Note that the values for variant 3 sensors are not comparable due to insufficiencies in the used model. | 80 |
| 7.4 | The flat-band voltage and oxide charge concentration calculated with the measured bulk doping concentration and the effective gate area of 0.2809 cm^{-2} at 22°C . The model does not apply for the p-spray variant. | 82 |
| 7.5 | The nominal input parameters and mesh parameters for the simulation. | 85 |
| 7.6 | The Median cell current for batch 5 PS-p light sensors and the MAD . Defective cells are defined as cells exceeding the median cell current the corresponding cell type by $50 * \text{MAD}$ | 98 |
| 9.1 | Specifications of the laser system | 109 |

-
- 10.1 The fundamental specifications of the telescope setup. The data includes the z-position, the thickness of the scatterers in units of radiation length as used in **GBL** track model, the active sensor area, the pixel geometry and the specified intrinsic resolution. For the alignment procedure all planes are considered. Final track reconstruction and pull analysis is performed with plane 4 to 8. The standard **MaPSA** module has a 4 layers of 35 μm copper in the carrier PCB. The carrier PCB has no cutout and therefore additional scattering material is introduced. The total material budget includes the air volume between the planes. 127
- 10.2 The table shows the measured width of the pull distribution from a Gaussian fit in an interval of one standard deviation around the peak, the predicted residuals used as input for the **GBL** fit, the **RMS** width of the biased residual distributions, all after the final iteration of the iterative pull analysis. . . . 140

List of Figures

| | | |
|-----|--|----|
| 2.1 | A slice of the CMS experiment from the interaction point to the outer perimeter taken from [2]. | 4 |
| 2.2 | The LHC accelerator complex from [6] with the major four experiments CMS , ATLAS , ALICE and LHCb and the preaccelerators. | 8 |
| 2.3 | The schedule for the upgrade of LHC to HL-LHC from [7, chap. 1]. Data taking periods are indicated in green. The CMS Tracker Detector will be replaced during LS3 | 9 |
| 2.4 | (a) The Higgs production cross sections for the different production channels from [9]. For increased centre of mass energy only small changes are expected. (b) The branching ratios of the Higgs decay channels as function of the Higgs mass from [10]. | 11 |
| 2.5 | (a-e) Different Feynman diagrams for the Higgs production channels. | 12 |
| 3.1 | The stopping power in silicon for electrons in red with radiative corrections (dotted) and collision contribution (dashed). The stopping power in silicon for protons in blue with nuclear (dotted) and electronic contribution (dashed), with data from [18]. The orange line indicates $\left. \frac{dE}{dx} \right _{min}$ for a MIP . For electrons the minimum is slightly lower than the minimum for other heavy particles. | 17 |

| | | |
|-----|---|----|
| 3.2 | Comparison of Bethe theory, with restricted energy loss and Landau MPV of different thickness for muons in silicon from [14, p. 445]. | 19 |
| 3.3 | The mass attenuation coefficient in silicon with contributions from photoelectric effect (p.e.), Rayleigh scattering, Compton scattering, nuclear and electronic pair production. Data taken from [20]. | 21 |
| 3.4 | The inverse absorption coefficient for intrinsic silicon at 300 K, the wavelength of the infrared laser used and the absorption edge for silicon. Data taken from [22]. | 23 |
| 3.5 | $I(z, x)/I_0$ of an ideal gaussian beam in intrinsic silicon without absorption. The beam parameters are $2W_0 = 3.6 \mu\text{m}$, $\lambda = 1056 \text{ nm}$, $n_{\text{Si}} = 3.554$. The red lines indicate, where $I(x, z)/I(x = 0, z) = 1/e^2$ | 26 |
| 3.6 | Relative EHP generation rate in silicon with silicon surface at $z = 0$ and beam waist at different z-positions absorption included (a-e). | 28 |
| 4.1 | (a) The bandstructure of silicon from [31, p. 14].(b) The electron ionization rates for different temperatures for silicon from [32]. | 30 |
| 4.2 | The function $f(w/p)$ from [35]. | 39 |
| 5.1 | (a) shows a unit cell of the PS-p light prototype sensor (see 6.3) with bias ring with n-implant below, metal bias rail and PTP structures. In (b) the important PTP design parameters, the width of p-stop implant (red) and distance between the n-implants (green) are introduced. The lightning shows critical points for HV-stability of the structure, which depend also on the quality and thickness of the silicon dioxide layer on top. | 43 |

-
- 5.2 The periphery of a macro-pixel sensor has a bias ring surrounding the active area, a guard ring and p-implanted edge region. 45
- 5.3 The punch through mechanism for a box charge concentration in the 1D case, when a bias voltage is applied. Left column shows the charge concentration depending on the x coordinate, the middle column the electric field, and the right column the electrostatic potential. Arbitrary units are used. 50
- 6.1 (a) Shows the principle of p_T -discrimination. A coincidence of two hits in closely spaced sensors is accepted, if inside the programmable correlation window (green). (b) For fixed sensor distance the distance in x of the hits forming a stub increases with distance from the interaction point (I.P.). (c) In order to have a homogeneous discriminating power in all tracker partitions, a set of sensor spacings is foreseen. E.g. for the same discriminating power a larger spacing is necessary in the endcaps. The picture is taken from [7, p. 24]. 52
- 6.2 The layout of the upgraded tracker. PS-modules are shown in blue, 2S-modules are shown in red, pixel modules in green and yellow. A part of PS-modules in the barrel region is tilted. The picture is taken from [7, p. 22]. 53
- 6.3 (a-b)The mechanical view of the **PS Module** from [7, chap. 3.1.2]. 54
- 6.4 A cut, not to scale, through the hybrid pixel cell shows the connection of **MPA** readout chip and silicon sensor with a bump bond. In the baseline design of the module an additional high resistive underfill is placed in the voids between sensor and chip as spark protection. The foreseen distance of sensor and chip is $80\ \mu\text{m}$ [7, chap. 9.2.2.5]. 56

- 6.5 Side view of the **PS** module for the baseline concept (a) from [7, chap. 3.1.2] and the inverted concept (b). The olive circles represent the bump bond connections. A high resistive underfill avoids possible sparking (lightning symbol) in the edge region in (a). The critical region for sparks in (b) is near the wire bonds. 57
- 6.6 (a) A simplified sketch (Top view) of the **MaPSA** in the baseline design. The p-type edge implant in red is at backplane potential. The potential drops from bias ring (yellow) to edge ring. A floating guard ring (black) improves HV-stability and field homogeneity at the edge of the active region. 2 x 8 **MPA** chips are bump bonded to the sensor in the final version. (b) In the inverted concept a routing area connects the **MPA** to the **FE hybrid**. Active area and routing have separate guard rings. The lightning symbol indicates critical regions for sparking in (a,b). 58
- 6.7 A cut through the wafer. P-stop implant red, strip implant green, metal light blue, thin dielectric brown, passivation oxide orange. (a) shows the edge of the routing area with guard ring and one signal trace. The implant below is kept at 0 V (ground plane). (b) shows two macro pixel cells with p-stop isolation in between. Strip implant and metal strip is connected. 59
- 6.8 Noise in a charge sensitive amplifier from [64, chap. 3.3.2]. . . 60
- 6.9 The data path for the **PS Module** from [7]. In the **L1** data path the zero-suppressed data is stored in a FIFO pipeline and transmitted to the back-end via a serializer, when the trigger signal arrives. The trigger path exploits real-time coincidence logic and data reduction steps in order to finally transmit the data to the **CIC** at bunch-crossing frequency. 63
- 6.10 The pixel front end of the **MPA** from [66, p. 88]. 64

-
- 6.11 The different cell types with geometry parameters from table 6.1 are depicted on the PS-p light standard sensor. Type 1 refers to standard cell geometry and has no extra colored box. The black line indicates the needle movement during the electrical characterization. The column and row numbering scheme is introduced. 67
- 7.1 The $1/C^2V$ characteristic for samples of variant 1 and 2 with the standard geometry and scaled simulated curves for different p-stop concentrations and p-stop depth, for the nominal **PTP** geometry and nominal conditions. 74
- 7.2 The IV characteristic for variant 1, 2, 3 and 4 with the standard geometry in (a). The inverted geometry was measured contacting the bias ring of the sensor active area only (b) . . . 76
- 7.3 The IV characteristic for variant 1, 2, 3 and 4 in (a,b,c,d) . . . 77
- 7.4 The $1/C^2V$ characteristic for variant 1, 2, 3 and 4 with the standard geometry in (a). The inverted geometry was measured contacting the bias ring of the sensor active area only (b) 78
- 7.5 The logarithm of the sensor currents vs $1/kT$ for in total 8 samples from variant 1, 2 and 3. Sensors from the variant 1, 2 and 3 are shown in different gray, red and green colors. 79
- 7.6 The temperature and humidity during the recording of the Arrhenius curves from figure 7.5. A low temperature ramp rate is necessary to keep the sensors in thermal equilibrium with the surrounding environment. A constant low relative humidity reduces effects due to varying surface current contribution. . . 80
- 7.7 The test structure design of the $7\text{ mm} \times 7\text{ mm}$ MOS. 82

- 7.8 The capacitance of the P-MOS structure for a sweep of the gate voltage. From negative to positive gate voltages three different regimes, accumulation, depletion and inversion are visible. 83
- 7.9 The IV characteristic of the **PTP** resistor for different backplane voltages V_{bp} in (a) and the differential resistance in (b). Zero potential is at bias ring, while a constant negative bias V_{bp} is applied to the backplane. A negative voltage sweep is conducted on the DC-pad with a second SMU. 84
- 7.10 (a) The density of free electrons at backplane voltage of 300 V. X/Y axis in μm . Source refers to the bias grid contact and drain to the pixel. The cylinder rotation axis is at 50 μm .(b) The absolute value of the nominal doping concentration. A cut through the cell implant, p-stop region and backplane is shown. The dots represent the sampling points of the analytic Gaussian and Error function profiles after the mesh is created. 86
- 7.11 (a)The electric field in the **PTP** at -300 V backplane voltage peaks at the edge of the implant of the bias dot. A second point where the critical electric field E_{bd} is reached for some parameter configurations is below the edge of the metal overhang of the bias dot. (b) The ionization integral for a standard round **PTP**, a linear **PTP**, and the pixel geometry for nominal parameters. The top view for a traditional linear punch through geometry without p-stops is shown in (c) 88
- 7.12 The extracted breakdown voltage V_{bd} depending on p-stop width (a), p-stop depth (b), p-stop concentration (c), and oxide thickness (d). 89
- 7.13 The extraction of V_{th} from the $I_d V_{sd}$ characteristic in (a). In (b) the absolute value of the drain current vs V_{sd} is shown. The effect of the p-stop width on V_{th} and R_{diff} is visible. . . 91

| | | |
|------|--|-----|
| 7.14 | The extracted threshold voltage V_{th} depending on p-stop width (a), p-stop depth (b), p-stop concentration (c), and oxide thickness (d). | 92 |
| 7.15 | The extracted differential resistance $R_{diff}(V_{sd} = 0\text{ V})$ depending on p-stop width (a), p-stop depth (b), p-stop concentration (c), and oxide thickness (d). | 93 |
| 7.16 | (a) The measurement schematic for the strip current and for the characterization of the PTP | 94 |
| 7.17 | (a) The measured pixel current for a variant 1, batch 5, wafer 2 sensor, with red lines as row separators. In (b) the current mapped to the sensor geometry is shown. The cell geometry affects the current. In (c) the current is shown normalized per cell area. The tentative, maximum allowed cell current from [7, p. 143] is 0.3 nA mm^{-2} for $p_x = 100\text{ }\mu\text{m}$. (d) shows the cumulative sum of the single pixel current and the total dark current of the device measured at each measurement step. | 96 |
| 7.18 | (a) shows the effects of charge up on the pixel current. (b-d) The normalized single strip currents for the measured devices from different variants (Batch 5). | 97 |
| 7.19 | Pictures from optical inspection of the PTP structures: (a) A regular PTP structure, where mask misalignment between metal and n-implant is visible. (b,c) Observed irregularities corresponding to strips with high pixel dark current. | 99 |
| 7.20 | (a) shows the absolute current measured with SMU2, when a voltage is applied across the PTP for a PS-p light sensor of batch 5, wafer 2. The corresponding current measured on the DC-pad of the neighbor strip is shown in (b). (c) and (d) show a measurement for a sensor affected by charge up from the same wafer. | 101 |
| 7.21 | The differential resistance of the PTP at 0 V (a). (b) The interpixel resistance extracted from the linear fits. | 101 |

- 8.1 (a) Shows one inverted module with two readout chips connected to the sensor after connecting the routing area to the carrier PCB with wire bonds. Due to limitations in the chosen low-cost PCB technology a maximum of two MPA-lights can be used. (b) Tight tolerances together with insufficient mechanical alignment result in wire bonds touching the sensor edge. 105
- 8.2 (a-b) Shows the data from a threshold scan for the inverted **MaPSA-Light** (left) and the a standard **MaPSA-Light** (right) assembled by KIT with in total 96 channels readout at 100 V after calibration. In (c) the single channel counter data is added and normalized to the number of channels. The extracted total noise figure is taken from a Gaussian fit. In (d) the distribution of the predicted **TRIMDAC** values after the last calibration step is shown. The blue lines indicate the maximum and minimum possible register values. One of the channels is outside the dynamic range and therefore switched off during the operation. 107
- 9.1 A simplified sketch of the laser test setup. 110
- 9.2 (a) A single channel spectrum normalized to the pulse repetition rate contains the noise peak and a signal s-curve. (b) The **LoG** kernel with $\sigma = 7$ used for the convolution. (c) The signal may be extracted directly from the filtered spectrum. A scaled version is overlaid. 111
- 9.3 (a) Coordinate system for the laser tests. The red square is the test region. x defined perpendicular to long edge of cells, y perpendicular to metal opening. (b) The YZ-scan shows the signal of a single channel and the signal drop at the metal edge at $y \approx 66.6$ mm 112

- 9.4 The response of the single channels to the laser pulses moving perpendicular to the long edge of the cells (a). The sum signal of all channels shows good uniformity across the channels(b) . 114
- 9.5 (a) A scan in $1\ \mu\text{m}$ steps along x of adjacent channels near the laser focus for studies of charge sharing. The overlay of the sensor geometry is centered with the interpolated point of equal shared charge. (b) Unbiased measures of charge sharing along x are obtained by dividing the difference of signals by the sum of signals. The FWHM (18 ± 2) μm of the distribution charge cloud is indicated by the orange lines. 116
- 9.6 (a) A simplified sketch of synchronization scheme. (b) The different situations, which occur during pulse shape sampling. . 117
- 9.7 Shows the counter contents for the synchronized laser tests, with the pedestal peak out of scale, for different delay settings. In case the algorithm finds rising and falling edge over noise, the line indicates the fit function. 119
- 9.8 The content of 96 memory cells for the synchronized laser tests. The data was taken simultaneously with counters (see figure 9.7.119
- 9.9 The reconstructed pedestal subtracted pulse shape from the curve fits to the counter data. The fit function is to guide the eye and indicates the rising edge of the signal, with time constants given in the **MPA-light** specifications (a). (b) The comparison of counter and memory data 120
- 10.1 The beam generation at DESY from [94]. Gammas originating from a fiber target produce $e^- e^+$ pairs in a converter target. Particle energy selection via magnet and collimator is possible. 122
- 10.2 The setup during the TB at DESY has 6 **MIMOSA** planes, the CMS timing reference plane, one **MaPSA-Light** and one **Inverted MaPSA-light**. 123

-
- 10.3 The schematic of the setup with trigger and busy logic and clock synchronization scheme. The trigger signal in red is omitted for the **MIMOSA** planes. In green and orange is the 40 MHz clock signal with different delay for CMS-pixel and **DUT**. In blue the busy signal is shown. 124
- 10.4 The timing of signals important for the trigger gating and busy logic used throughout the test beam. CLK refers to the 40 MHz clock. The coincidence to **TLU** signal is used with the coincidence of three other PMs to provide the trigger. 126
- 10.5 The complete analysis chain for the Testbeam data with all processor steps and the necessary additional alignment and geometry constants included. 128
- 10.6 The reconstructed discrete hit positions after clustering for on-track hits in the **MaPSA** frame of reference. Binary readout prefers hit positions at the cell center and the intermediate hit positions are naturally suppressed. The data in this plot contains three pixels, which are masked due to calibration issues. The data was acquired at **THDAC** = 100, $V_b = 100$ V with 5.6 GeV electrons with the beam perpendicular to the sensor. . 131
- 10.7 (a-f) The method of realigning the data streams for a run with 1×10^6 events. Note the different z-axis range for the plots containing **MaPSA** data. 133
- 10.8 (a) GBL-fit probability after alignment and iterative pull analysis for an exemplary run. The tracks not passing the cut at 0.01 are not used for analysis. (b) The triplet-track multiplicity per event. 137
- 10.9 The pull distributions the telescope plane 4, 5 and 6, the CMS-Reference plane and the inverted **MaPSA**. 143
- 10.10 The biased residual distributions the telescope plane 4, 5 and 6, the CMS-Reference plane and the inverted **MaPSA**. 144

- 10.11(a) The efficiency in the frame of reference of the telescope. (b) The cut applied in order to select a homogeneous region for the efficiency measurement. (c) The efficiency and fake hit rate as a function of the threshold voltage. Statistical error bars are calculated with Clopper-Pearson interval at 95 % confidence level. (d) The normalized clustersize distribution for clusters containing regular pixel only at **THDAC** of 90. (e) The mean on-track clustersize depending on the set threshold value. . . 145

Bibliography

- [1] CMS Collaboration. “The CMS Experiment at the CERN LHC”. In: *JINST* 3 (2008), S08004. DOI: [10.1088/1748-0221/3/08/S08004](https://doi.org/10.1088/1748-0221/3/08/S08004) (cit. on pp. 3, 6).
- [2] CMS Collaboration. “Particle-Flow Reconstruction and Global Event Description with the CMS Detector”. In: *JINST* 12.10 (2017), P10003. DOI: [10.1088/1748-0221/12/10/P10003](https://doi.org/10.1088/1748-0221/12/10/P10003). arXiv: [1706.04965](https://arxiv.org/abs/1706.04965) (cit. on p. 4).
- [3] CMS Collaboration. “CMS Technical Design Report for the Pixel Detector Upgrade”. In: (2012). DOI: [10.2172/1151650](https://doi.org/10.2172/1151650) (cit. on p. 5).
- [4] CMS Collaboration. “The CMS Trigger System”. In: *JINST* 12.01 (2017), P01020. DOI: [10.1088/1748-0221/12/01/P01020](https://doi.org/10.1088/1748-0221/12/01/P01020). arXiv: [1609.02366](https://arxiv.org/abs/1609.02366) [[physics.ins-det](https://arxiv.org/abs/1609.02366)] (cit. on p. 6).
- [5] G Apollinari et al. “High-Luminosity Large Hadron Collider (HL-LHC) : Preliminary Design Report”. In: (2015). DOI: [10.5170/CERN-2015-005](https://doi.org/10.5170/CERN-2015-005) (cit. on pp. 7, 8).
- [6] Esma Mobs. “The CERN Accelerator Complex. Complexe Des Accélérateurs Du CERN”. In: (July 2016). General Photo. URL: <https://cds.cern.ch/record/2197559> (cit. on p. 8).
- [7] CMS Collaboration. *The Phase-2 Upgrade of the CMS Tracker*. Geneva: CERN, June 2017. URL: <https://cds.cern.ch/record/2272264> (cit. on pp. 7, 9, 13, 42, 52–57, 63, 86, 90, 94, 96).

- [8] ATLAS, CMS Collaboration. “Measurements of the Higgs Boson Production and Decay Rates and Constraints on Its Couplings from a Combined ATLAS and CMS Analysis of the LHC Pp Collision Data at S=7 and 8 TeV”. In: *JHEP* 08 (2016), p. 045. DOI: [10.1007/JHEP08\(2016\)045](https://doi.org/10.1007/JHEP08(2016)045). arXiv: [1606.02266](https://arxiv.org/abs/1606.02266) [[hep-ex](#)] (cit. on p. 10).
- [9] Julien Baglio and Abdelhak Djouadi. “Higgs Production at the LHC”. In: *JHEP* 03 (2011), p. 055. DOI: [10.1007/JHEP03\(2011\)055](https://doi.org/10.1007/JHEP03(2011)055). arXiv: [1012.0530](https://arxiv.org/abs/1012.0530) [[hep-ph](#)] (cit. on p. 11).
- [10] LHC Higgs Cross Section Working Group Collaboration. “Handbook of LHC Higgs Cross Sections: 4. Deciphering the Nature of the Higgs Sector”. In: (2016). DOI: [10.23731/CYRM-2017-002](https://doi.org/10.23731/CYRM-2017-002). arXiv: [1610.07922](https://arxiv.org/abs/1610.07922) [[hep-ph](#)] (cit. on p. 11).
- [11] CMS Collaboration. “Observation of a New Boson at a Mass of 125 GeV with the CMS Experiment at the LHC”. In: *Phys Lett B* 716 (CMS-HIG-12-028. CMS-HIG-12-028. CERN-PH-EP-2012-220 July 2012), 30–61. 59 p. DOI: [10.1016/j.physletb.2012.08.021](https://doi.org/10.1016/j.physletb.2012.08.021) (cit. on p. 10).
- [12] CMS Collaboration. “Observation of the Higgs Boson Decay to a Pair of τ Leptons with the CMS Detector”. In: *Phys Lett B* 779 (2018), pp. 283–316. DOI: [10.1016/j.physletb.2018.02.004](https://doi.org/10.1016/j.physletb.2018.02.004). arXiv: [1708.00373](https://arxiv.org/abs/1708.00373) [[hep-ex](#)] (cit. on p. 12).
- [13] CMS Collaboration. *Technical Proposal for the Phase-II Upgrade of the CMS Detector*. CERN-LHCC-2015-010. LHCC-P-008. CMS-TDR-15-02. Geneva, June 2015. URL: <http://cds.cern.ch/record/2020886> (cit. on pp. 13, 14).
- [14] K.A. Olive. “Review of Particle Physics”. In: *Chin. Phys. C* 40.10 (Oct. 2016), p. 1808. ISSN: 1674-1137. DOI: [10.1088/1674-1137/40/10/100001](https://doi.org/10.1088/1674-1137/40/10/100001) (cit. on pp. 15, 16, 19).
- [15] Hermann Kolanoski and Norbert Wermes. *Teilchendetektoren: Grundlagen und Anwendungen*. OCLC: 932681661. Berlin Heidelberg: Springer Spektrum, 2016. 921 pp. ISBN: 978-3-662-45350-6 (cit. on pp. 16, 17, 19, 20, 33, 37, 46, 70).

- [16] Claus Grupen, Boris A. Shwartz, and Helmuth Spieler. *Particle Detectors*. 2nd ed. Cambridge monographs on particle physics, nuclear physics, and cosmology 26. OCLC: ocn168721194. Cambridge, UK ; New York: Cambridge University Press, 2008. 651 pp. ISBN: 978-0-521-84006-4 (cit. on p. 16).
- [17] M. N. Mazziotta. “Electron–hole Pair Creation Energy and Fano Factor Temperature Dependence in Silicon”. In: *Nucl Instrum Meth A* 584.2 (2008), pp. 436–439. ISSN: 0168-9002. DOI: [10.1016/j.nima.2007.10.043](https://doi.org/10.1016/j.nima.2007.10.043) (cit. on p. 16).
- [18] M Berger and M Berger. *Stopping-Power and Range Tables for Electrons, Protons, and Helium Ions: Physical Reference Data*. Gaithersburg, MD: NIST, 1999. URL: <http://cds.cern.ch/record/399381> (cit. on pp. 17, 140).
- [19] H. Bichsel. “Straggling in Thin Silicon Detectors”. In: *Rev Mod Phys* 60 (1988), pp. 663–699. DOI: [10.1103/RevModPhys.60.663](https://doi.org/10.1103/RevModPhys.60.663) (cit. on p. 18).
- [20] M J Berger and J H Hubbel. *XCOM: Photon Cross Sections on a Personal Computer*. NIST X-ray and Gamma-ray Attenuation Coefficients and Cross Sections Database. Gaithersburg, MD: NIST, 1999. URL: <http://physics.nist.gov/xcom> (cit. on p. 21).
- [21] Bahaa E A Saleh and Malvin Carl Teich. *Fundamentals of Photonics*. 2nd. Wiley series in pure and applied optics. New York, NY: Wiley, 2007. URL: <https://cds.cern.ch/record/1084451> (cit. on pp. 21, 24, 25).
- [22] Martin A. Green. “Self-Consistent Optical Parameters of Intrinsic Silicon at 300K Including Temperature Coefficients”. In: *Sol. Energy Mater. Sol. Cells* 92.11 (Nov. 2008), pp. 1305–1310. ISSN: 09270248. DOI: [10.1016/j.solmat.2008.06.009](https://doi.org/10.1016/j.solmat.2008.06.009) (cit. on pp. 23, 27).
- [23] J. Krizmanic et al. “A 1060-Nm Diode Laser System for Dynamically Probing Silicon Detectors”. In: *Nucl. Instrum. Meth.* A374 (1996), pp. 315–319. DOI: [10.1016/0168-9002\(96\)00239-2](https://doi.org/10.1016/0168-9002(96)00239-2) (cit. on p. 23).

- [24] I. Abt et al. “Characterization of Silicon Microstrip Detectors Using an Infrared Laser System”. In: *Nucl. Instrum. Meth.* A423 (1999), pp. 303–319. DOI: [10.1016/S0168-9002\(98\)01337-0](https://doi.org/10.1016/S0168-9002(98)01337-0) (cit. on p. 23).
- [25] Pavel Bazant et al. “Laser Measurement of Absolute Charge Collection Efficiency of a Silicon Detector”. In: *Nucl. Instrum. Meth.* A581 (2007), pp. 306–309. DOI: [10.1016/j.nima.2007.07.128](https://doi.org/10.1016/j.nima.2007.07.128) (cit. on p. 24).
- [26] Z. Dolezal et al. “Laser Tests of Silicon Detectors”. In: *Nucl. Instrum. Meth.* A573 (2007), pp. 12–15. DOI: [10.1016/j.nima.2006.10.319](https://doi.org/10.1016/j.nima.2006.10.319) (cit. on p. 24).
- [27] Ladislav Andricek et al. “Spatial Resolution Analysis of Micron Resolution Silicon Pixel Detectors Based on Beam and Laser Tests”. In: *Nucl. Instrum. Meth.* A604 (2009), pp. 385–389. DOI: [10.1016/j.nima.2009.01.097](https://doi.org/10.1016/j.nima.2009.01.097) (cit. on p. 24).
- [28] Claus F Klingshirn. *Semiconductor Optics; 2nd Ed.* Graduate Texts in Physics. Berlin: Springer, 2005. ISBN: 978-3-540-38347-5 (cit. on p. 24).
- [29] Rüdiger Paschotta. *Encyclopedia of Laser Physics and Technology*. OCLC: ocn229464595. Weinheim: Wiley-VCH, 2008. 2 pp. ISBN: 978-3-527-40828-3 (cit. on p. 24).
- [30] Ekbert Hering and Rolf Martin, eds. *Photonik*. Berlin/Heidelberg: Springer-Verlag, 2006. ISBN: 978-3-540-23438-8 (cit. on p. 24).
- [31] S. M. Sze and Kwok Kwok Ng. *Physics of Semiconductor Devices*. 3rd ed. Hoboken, N.J: Wiley-Interscience, 2007. 815 pp. ISBN: 978-0-471-14323-9 (cit. on pp. 29, 30, 38, 39, 71, 81, 87).
- [32] C. R. Crowell and S. M. Sze. “Temperature Dependence of Avalanche Multiplication in Semiconductors”. In: *Appl. Phys. Lett.* 9.6 (Sept. 15, 1966), pp. 242–244. ISSN: 0003-6951, 1077-3118. DOI: [10.1063/1.1754731](https://doi.org/10.1063/1.1754731) (cit. on pp. 30, 39).
- [33] Gerhard Lutz. *Semiconductor Radiation Detectors*. Berlin, Heidelberg: Springer Berlin Heidelberg, 2007. ISBN: 978-3-540-71679-2. DOI: [10.1007/978-3-540-71679-2](https://doi.org/10.1007/978-3-540-71679-2) (cit. on pp. 33, 44, 46, 47, 72).

- [34] D. M. Caughey and R. E. Thomas. “Carrier Mobilities in Silicon Empirically Related to Doping and Field”. In: *Proc. IEEE* 55.12 (Dec. 1967), pp. 2192–2193. ISSN: 0018-9219. DOI: [10.1109/PROC.1967.6123](https://doi.org/10.1109/PROC.1967.6123) (cit. on p. 33).
- [35] E. Barberis et al. “Capacitances in Silicon Microstrip Detectors”. In: *Nucl. Instrum. Meth.* A342 (1994), pp. 90–95. DOI: [10.1016/0168-9002\(94\)91414-1](https://doi.org/10.1016/0168-9002(94)91414-1) (cit. on pp. 38, 39).
- [36] Simon Ramo. “Currents Induced by Electron Motion”. In: *Proc Ire* 27 (1939), pp. 584–585. DOI: [10.1109/JRPROC.1939.228757](https://doi.org/10.1109/JRPROC.1939.228757) (cit. on p. 41).
- [37] W. Shockley. “Currents to Conductors Induced by a Moving Point Charge”. In: *J. Appl. Phys.* 9.10 (1938), pp. 635–636. DOI: [10.1063/1.1710367](https://doi.org/10.1063/1.1710367) (cit. on p. 41).
- [38] J. Kemmer et al. “Development of 10-Micrometer Resolution Silicon Counters for Charm Signature Observation with the ACCMOR Spectrometer”. In: *Workshop on Silicon Detectors for High-Energy Physics. Batavia, Illinois, October 15-16, 1981*. 1981, pp. 195–217 (cit. on p. 41).
- [39] E. Belau et al. “The Charge Collection in Silicon Strip Detectors”. In: *Nucl Instrum Meth* 214 (1983), p. 253. DOI: [10.1016/0167-5087\(83\)90591-4](https://doi.org/10.1016/0167-5087(83)90591-4) (cit. on p. 41).
- [40] J. Kemmer and G. Lutz. “New Detector Concepts”. In: *Nucl Instrum Meth* A253 (1987), pp. 365–377. DOI: [10.1016/0168-9002\(87\)90518-3](https://doi.org/10.1016/0168-9002(87)90518-3) (cit. on p. 41).
- [41] Georg Auzinger. “Silicon Sensor Development for the CMS Tracker Upgrade”. CERN, Oct. 22, 2013. URL: <https://cds.cern.ch/record/1631093> (cit. on pp. 42, 130).
- [42] Ranjeet Dalal et al. “Development of Radiation Damage Models for Irradiated Silicon Sensors Using TCAD Tools”. In: *PoS TIPP2014* (2014), p. 276 (cit. on p. 42).

- [43] Thomas Eichhorn et al. “Simulations of Inter-Strip Capacitance and Resistance for the Design of the CMS Tracker Upgrade”. In: *PoS TIPP2014* (2014), p. 279 (cit. on p. 42).
- [44] Martin Printz. “Radiation Hard Sensor Materials for the CMS Tracker Phase II Upgrade - Charge Collection of Different Bulk Polarities”. In: *Nucl Instrum Meth A765* (2014). bibtex{booktitle:'Proceedings, 9th International Hiroshima Symposium on Development and Application of Semiconductor Tracking Detectors (HSTD-9): Hiroshima, Japan, September 2-6, 2013'}, pp. 29–34. DOI: [10.1016/j.nima.2014.04.042](https://doi.org/10.1016/j.nima.2014.04.042) (cit. on p. 42).
- [45] CMS Tracker Collaboration. “T-CAD Analysis of Electric Fields in n-in-p Silicon Strip Detectors in Dependence on the p-Stop Pattern and Doping Concentration”. In: *JINST 10.01* (2015), p. C01048. DOI: [10.1088/1748-0221/10/01/C01048](https://doi.org/10.1088/1748-0221/10/01/C01048) (cit. on p. 42).
- [46] CMS Collaboration. “Design Optimization of Pixel Sensors Using Device Simulations for the Phase-II CMS Tracker Upgrade”. In: *Nucl Instrum Meth A824* (2016), pp. 413–416. DOI: [10.1016/j.nima.2015.08.053](https://doi.org/10.1016/j.nima.2015.08.053) (cit. on p. 42).
- [47] CMS Tracker Collaboration. “P-Stop Isolation Study of Irradiated n-in-p Type Silicon Strip Sensors for Harsh Radiation Environments”. In: *Nucl Instrum Meth A831* (2016), pp. 38–43. DOI: [10.1016/j.nima.2016.05.103](https://doi.org/10.1016/j.nima.2016.05.103) (cit. on p. 42).
- [48] Martin Printz. “Analysis of N-in-p Type Silicon Detectors for High Radiation Environment with Fast Analogue and Binary Readout Systems”. Karlsruhe Institut für Technologie (KIT), Diss., 2016. Dr. Karlsruhe Institut für Technologie (KIT), 2016. URL: <https://exp-invenio.physik.uni-karlsruhe.de/record/48797> (cit. on pp. 42, 89, 90).
- [49] G. Lindstrom, M. Moll, and E. Fretwurst. “Radiation Hardness of Silicon Detectors: A Challenge from High-Energy Physics”. In: *Nucl Instrum Meth A426* (1999), pp. 1–15. DOI: [10.1016/S0168-9002\(98\)01462-4](https://doi.org/10.1016/S0168-9002(98)01462-4) (cit. on p. 42).

- [50] E. Fretwurst et al. “Bulk Damage Effects in Standard and Oxygen Enriched Silicon Detectors Induced by Co-60 Gamma Radiation”. In: *Nucl Instrum Meth A*514 (2003), pp. 1–8. DOI: [10.1016/j.nima.2003.08.077](https://doi.org/10.1016/j.nima.2003.08.077) (cit. on p. 42).
- [51] CERN RD50 Collaboration. “Recent Advancements in the Development of Radiation Hard Semiconductor Detectors for S-LHC”. In: *Nucl Instrum Meth A*552 (2005), pp. 7–19. DOI: [10.1016/j.nima.2005.05.039](https://doi.org/10.1016/j.nima.2005.05.039) (cit. on p. 42).
- [52] Frank Hartmann. *Evolution of Silicon Sensor Technology in Particle Physics*. Springer tracts in modern physics 231. OCLC: ocn150344856. Berlin: Springer, 2009. 204 pp. ISBN: 978-3-540-25094-4 (cit. on pp. 42, 43, 45, 71, 76, 90).
- [53] L. Rossi et al. *Pixel Detectors*. Particle Acceleration and Detection. Berlin: Springer-Verlag, 2006. ISBN: 978-3-540-28332-4. URL: <http://www.springer.com/book/3-540-28332-3> (cit. on pp. 46, 47, 55, 56, 61, 76).
- [54] M. Fahrner et al. “Beam-Loss-Induced Electrical Stress Test on CMS Silicon Strip Modules”. In: *Nucl. Instrum. Meth.* A518 (2004), pp. 328–330. DOI: [10.1016/j.nima.2003.11.011](https://doi.org/10.1016/j.nima.2003.11.011) (cit. on p. 46).
- [55] H.F.-W. Sadrozinski et al. “Punch-through Protection of SSDs in Beam Accidents”. In: *Nucl. Instrum. Meth.* A658.1 (Dec. 2011), pp. 46–50. ISSN: 01689002. DOI: [10.1016/j.nima.2011.06.085](https://doi.org/10.1016/j.nima.2011.06.085) (cit. on p. 46).
- [56] Simon Spannagel. “Test Beam Measurements for the Upgrade of the CMS Pixel Detector and Measurement of the Top Quark Mass from Differential Cross Sections”. Universität Hamburg, Diss., 2016. Dr. Hamburg: Universität Hamburg, 2016. URL: <https://bib-pubdb1.desy.de/record/297247> (cit. on p. 47).
- [57] Y. Unno et al. “Development of N-on-p Silicon Sensors for Very High Radiation Environments”. In: *Nucl. Instrum. Meth.* A636 (2011), S24–S30. DOI: [10.1016/j.nima.2010.04.080](https://doi.org/10.1016/j.nima.2010.04.080) (cit. on p. 47).

- [58] Y. Unno et al. “Optimization of Surface Structures in N-in-p Silicon Sensors Using TCAD Simulation”. In: *Nucl. Instrum. Meth.* A636 (2011), S118–S124. DOI: [10.1016/j.nima.2010.04.095](https://doi.org/10.1016/j.nima.2010.04.095) (cit. on p. 47).
- [59] P. Azzi et al. “Radiation Damage Experience at CDF with SVX”. In: *Nucl. Instrum. Meth.* A383 (1996), pp. 155–158. DOI: [10.1016/S0168-9002\(96\)00621-3](https://doi.org/10.1016/S0168-9002(96)00621-3) (cit. on p. 47).
- [60] L. Andricek et al. “Single-Sided P+ n and Double-Sided Silicon Strip Detectors Exposed to Fluences up to $2 \times 10^{14}/\text{Cm}^2$ 24-GeV Protons”. In: *Nucl. Instrum. Meth.* A409 (1998), pp. 184–193. DOI: [10.1016/S0168-9002\(97\)01259-X](https://doi.org/10.1016/S0168-9002(97)01259-X) (cit. on p. 47).
- [61] J. Lohstroh et al. “Punch-through Currents in P+NP+ and N+PN+ Sandwich Structures—I: Introduction and Basic Calculations”. In: *Solid-State Electron.* 24.9 (1981), pp. 805–814. DOI: [10.1016/0038-1101\(81\)90095-2](https://doi.org/10.1016/0038-1101(81)90095-2) (cit. on pp. 47, 48).
- [62] J. Lohstroh et al. “Punch-through Currents in P+NP+ and N+PN+ Sandwich Structures—II: General Low-Injection Theory and Measurements”. In: *Solid-State Electron.* 24.9 (1981), pp. 815–820. ISSN: 0038-1101. DOI: [10.1016/0038-1101\(81\)90096-4](https://doi.org/10.1016/0038-1101(81)90096-4) (cit. on p. 47).
- [63] S.M. Sze, D.J. Coleman, and A. Loya. “Current Transport in Metal-Semiconductor-Metal (MSM) Structures”. In: *Solid-State Electron.* 14.12 (Dec. 1971), pp. 1209–1218. ISSN: 00381101. DOI: [10.1016/0038-1101\(71\)90109-2](https://doi.org/10.1016/0038-1101(71)90109-2) (cit. on p. 49).
- [64] P. Grybos. *Front-End Electronics for Multichannel Semiconductor Detector Systems*. Vol. 08. EuCARD Editorial Series on Accelerator Science. 2010. URL: <http://cds.cern.ch/record/1473436> (cit. on pp. 59–61).
- [65] F. Krummenacher. “Pixel Detectors with Local Intelligence: An IC Designer Point of View”. In: *Nucl. Instrum. Methods Phys. Res. Sect. Accel. Spectrometers Detect. Assoc. Equip.* 305.3 (Aug. 1991), pp. 527–532. ISSN: 01689002. DOI: [10.1016/0168-9002\(91\)90152-G](https://doi.org/10.1016/0168-9002(91)90152-G) (cit. on p. 62).

- [66] Davide Ceresa. “Electronic Systems for Intelligent Particle Tracking in the High Energy Physics Field”. PhD thesis. Politecnico di Torino, 2016. URL: http://porto.polito.it/2642937/1/Thesis_CERESA.pdf (visited on 11/29/2016) (cit. on pp. 62–65, 130).
- [67] CMS Collaboration. “Low-Cost Bump-Bonding Processes for High Energy Physics Pixel Detectors”. In: *JINST* 11.01 (2016), p. C01050. DOI: [10.1088/1748-0221/11/01/C01050](https://doi.org/10.1088/1748-0221/11/01/C01050) (cit. on p. 68).
- [68] P. Vichoudis et al. “The Gigabit Link Interface Board (GLIB), a Flexible System for the Evaluation and Use of GBT-Based Optical Links”. In: *JINST* 5.11 (2010), p. C11007. DOI: [10.1088/1748-0221/5/11/C11007](https://doi.org/10.1088/1748-0221/5/11/C11007) (cit. on p. 68).
- [69] P. Vichoudis et al. “First Results with the Gigabit Link Interface Board (GLIB)”. In: *JINST* 6 (2011), p. C12060. DOI: [10.1088/1748-0221/6/12/C12060](https://doi.org/10.1088/1748-0221/6/12/C12060) (cit. on p. 68).
- [70] M. Barros Marin et al. “A GLIB-Based uTCA Demonstration System for HEP Experiments”. In: *JINST* 8 (2013), p. C12011. DOI: [10.1088/1748-0221/8/12/C12011](https://doi.org/10.1088/1748-0221/8/12/C12011) (cit. on p. 68).
- [71] P. Vichoudis et al. “The Gigabit Link Interface Board (GLIB) Ecosystem”. In: *JINST* 8 (2013), p. C03012. DOI: [10.1088/1748-0221/8/03/C03012](https://doi.org/10.1088/1748-0221/8/03/C03012) (cit. on p. 68).
- [72] Martin Printz. *Radiation Hard Sensor Materials for the CMS Tracker Upgrade-Charge Collection of Different Bulk Polarities*. KIT, 2013 (cit. on p. 70).
- [73] CMS Tracker Collaboration. “P-Stop Isolation Study of Irradiated n-in-p Type Silicon Strip Sensors for Harsh Radiation Environments”. In: *Nucl. Instrum. Meth.* A831 (2016), pp. 38–43. DOI: [10.1016/j.nima.2016.05.103](https://doi.org/10.1016/j.nima.2016.05.103) (cit. on pp. 70, 90).
- [74] CMS Tracker Collaboration. “T-CAD Analysis of Electric Fields in n-in-p Silicon Strip Detectors in Dependence on the p-Stop Pattern and Doping Concentration”. In: *JINST* 10.01 (2015), p. C01048. DOI: [10.1088/1748-0221/10/01/C01048](https://doi.org/10.1088/1748-0221/10/01/C01048) (cit. on pp. 70, 90).

- [75] A Chilingarov. “Temperature Dependence of the Current Generated in Si Bulk”. In: *J. Instrum.* 8.10 (Oct. 3, 2013), P10003–P10003. ISSN: 1748-0221. DOI: [10.1088/1748-0221/8/10/P10003](https://doi.org/10.1088/1748-0221/8/10/P10003) (cit. on pp. 71, 78).
- [76] T. Ohsugi et al. “Microdischarges of AC Coupled Silicon Strip Sensors”. In: *Nucl Instrum Meth A* 342 (1994), pp. 22–26. DOI: [10.1016/0168-9002\(94\)91405-2](https://doi.org/10.1016/0168-9002(94)91405-2) (cit. on p. 74).
- [77] T. Kuwano et al. “Systematic Study of Micro-Discharge Characteristics of ATLAS Barrel Silicon Microstrip Modules”. In: *Nucl Instrum Meth A* 579 (2007), pp. 782–787. DOI: [10.1016/j.nima.2007.05.288](https://doi.org/10.1016/j.nima.2007.05.288) (cit. on p. 74).
- [78] G.-F. Dalla Betta et al. “Investigation of Leakage Current and Breakdown Voltage in Irradiated Double-Sided 3D Silicon Sensors”. In: *J. Instrum.* 11.09 (Sept. 19, 2016), P09006–P09006. ISSN: 1748-0221. DOI: [10.1088/1748-0221/11/09/P09006](https://doi.org/10.1088/1748-0221/11/09/P09006) (cit. on p. 79).
- [79] M. Povoli et al. “Impact of the Layout on the Electrical Characteristics of Double-Sided Silicon 3D Sensors Fabricated at FBK”. In: *Nucl. Instrum. Meth.* A699 (2013), pp. 22–26. DOI: [10.1016/j.nima.2012.04.080](https://doi.org/10.1016/j.nima.2012.04.080) (cit. on p. 79).
- [80] Synopsys, Inc. *Synopsys Sentaurus TCAD Ver. N-2017.09*. Mountain View, CA, USA, 2017. URL: <https://www.synopsys.com/> (cit. on p. 84).
- [81] B.E. Deal. “Standardized Terminology for Oxide Charges Associated with Thermally Oxidized Silicon”. In: *IEEE Trans. Electron Devices* 27.3 (Mar. 1980), pp. 606–608. ISSN: 0018-9383. DOI: [10.1109/T-ED.1980.19908](https://doi.org/10.1109/T-ED.1980.19908) (cit. on p. 85).
- [82] Jiaguo Zhang. “X-Ray Radiation Damage Studies and Design of a Silicon Pixel Sensor for Science at the XFEL”. PhD thesis. Hamburg: Universität Hamburg, 2013. 193 pp. URL: https://www.physnet.uni-hamburg.de/services/biblio/dissertation/dissfbPhysik/___Kurzfassungen/Jiaguo___Zhang.htm (cit. on pp. 85, 100).

- [83] Joern Schwandt. “Design of a Radiation Hard Silicon Pixel Sensor for X-Ray Science”. Dissertation / PhD Thesis Internal Report. University of Hamburg, 2014. URL: <https://bib-pubdb1.desy.de/record/205852> (cit. on pp. 86, 87).
- [84] R. Van Overstraeten and H. De Man. “Measurement of the Ionization Rates in Diffused Silicon P-n Junctions”. In: *Solid-State Electron.* 13.5 (1970), pp. 583–608. ISSN: 0038-1101. DOI: [https://doi.org/10.1016/0038-1101\(70\)90139-5](https://doi.org/10.1016/0038-1101(70)90139-5) (cit. on p. 87).
- [85] Adelmo Ortiz-Conde et al. “Revisiting MOSFET Threshold Voltage Extraction Methods”. In: *Microelectron. Reliab.* 53.1 (Jan. 2013), pp. 90–104. ISSN: 00262714. DOI: [10.1016/j.microrel.2012.09.015](https://doi.org/10.1016/j.microrel.2012.09.015) (cit. on p. 90).
- [86] R. Dalal et al. “Combined Effect of Bulk and Surface Damage on Strip Insulation Properties of Proton Irradiated N+ -p Silicon Strip Sensors”. In: *JINST* 9 (2014), P04007. DOI: [10.1088/1748-0221/9/04/P04007](https://doi.org/10.1088/1748-0221/9/04/P04007) (cit. on p. 90).
- [87] Manfred Valentan. “The Silicon Vertex Detector for B-Tagging at Belle II”. Dissertation. Wien: TU Wien, Sept. 24, 13. 311 pp. (cit. on p. 95).
- [88] Helmuth Spieler. *Semiconductor Detector Systems*. Series on semiconductor science and technology 12. OCLC: ocm61302135. Oxford ; New York: Oxford University Press, 2005. 489 pp. ISBN: 978-0-19-852784-8 (cit. on pp. 98, 115).
- [89] A. E. Siegman. “How to (Maybe) Measure Laser Beam Quality”. In: *DPSS (Diode Pumped Solid State) Lasers: Applications and Issues*. Optical Society of America, 1998, MQ1. DOI: [10.1364/DLAI.1998.MQ1](https://doi.org/10.1364/DLAI.1998.MQ1) (cit. on p. 108).
- [90] Michael Hofer. “Characterization of a Laser System for a Transient Current Technique Setup”. Bachelor thesis. TU Wien, 2016. 36 pp. (cit. on p. 108).

- [91] Andres Huertas and Gerard Medioni. “Detection of Intensity Changes with Subpixel Accuracy Using Laplacian-Gaussian Masks”. In: *IEEE Trans. Pattern Anal. Mach. Intell.* PAMI-8.5 (Sept. 1986), pp. 651–664. ISSN: 0162-8828, 2160-9292. DOI: [10.1109/TPAMI.1986.4767838](https://doi.org/10.1109/TPAMI.1986.4767838) (cit. on p. 111).
- [92] Oleksiy Sokolov. “Prototyping of Silicon Strip Detectors for the Inner Tracker of the ALICE Experiment”. PhD thesis. Universiteit Utrecht, 2006. URL: <http://cds.cern.ch/record/1065732> (cit. on p. 113).
- [93] E. Belau et al. “The Charge Collection in Silicon Strip Detectors”. In: *Nucl Instrum Meth* 214 (1983), p. 253. DOI: [10.1016/0167-5087\(83\)90591-4](https://doi.org/10.1016/0167-5087(83)90591-4) (cit. on p. 116).
- [94] DESY. *Image*. URL: http://particle-physics.desy.de/test_beams_at_desy/beam_generation/index_ger.html (cit. on p. 122).
- [95] Hendrik Jansen et al. “Performance of the EUDET-Type Beam Telescopes”. In: *EPJ Tech Instrum* 3.1 (2016), p. 7. DOI: [10.1140/epjti/s40485-016-0033-2](https://doi.org/10.1140/epjti/s40485-016-0033-2). arXiv: [1603.09669](https://arxiv.org/abs/1603.09669) (cit. on pp. 123, 126, 134, 135, 139).
- [96] Hendrik Jansen. “Resolution Studies with the DATURA Beam Telescope”. In: *JINST* 11.12 (2016), p. C12031. DOI: [10.1088/1748-0221/11/12/C12031](https://doi.org/10.1088/1748-0221/11/12/C12031). arXiv: [1610.02505](https://arxiv.org/abs/1610.02505) [[physics.ins-det](https://arxiv.org/archive/physics)] (cit. on p. 123).
- [97] D Cussans. “A Trigger/Timing Logic Unit for ILC Test-Beams”. In: (2007) (cit. on p. 124).
- [98] C. Hu-Guo et al. “First Reticule Size MAPS with Digital Output and Integrated Zero Suppression for the EUDET-JRA1 Beam Telescope”. In: *Nucl Instrum Meth* A623 (2010), pp. 480–482. DOI: [10.1016/j.nima.2010.03.043](https://doi.org/10.1016/j.nima.2010.03.043) (cit. on p. 126).
- [99] Davide Ceresa, Jan Kaplon, and Alessandro Marchioro. *MPA-Light User Manual*. 2015. URL: https://indico.cern.ch/event/395778/session/1/contribution/8/attachments/793090/1087089/MPA-LightManual_150316.pdf (visited on 01/01/2018) (cit. on p. 128).

- [100] Igor Rubinskiy. *EU Telescope - Offline Track Reconstruction and DUT Analysis Software*. Jan. 10, 2010. URL: <http://www.eudet.org/e26/e28/e86887/e107460/EUDET-Memo-2010-12.pdf> (cit. on p. 129).
- [101] R. Turchetta. “Spatial Resolution of Silicon Microstrip Detectors”. In: *Nucl Instrum Meth* A335 (1993), pp. 44–58. DOI: [10.1016/0168-9002\(93\)90255-G](https://doi.org/10.1016/0168-9002(93)90255-G) (cit. on p. 129).
- [102] Kesheng Wu, Ekow Otoo, and Kenji Suzuki. “Optimizing Two-Pass Connected-Component Labeling Algorithms”. In: *Pattern Anal. Appl.* 12.2 (June 2009), pp. 117–135. ISSN: 1433-7541, 1433-755X. DOI: [10.1007/s10044-008-0109-y](https://doi.org/10.1007/s10044-008-0109-y) (cit. on p. 129).
- [103] V. Blobel. “A New Fast Track-Fit Algorithm Based on Broken Lines”. In: *Nucl Instrum Meth* A566 (2006), pp. 14–17. DOI: [10.1016/j.nima.2006.05.156](https://doi.org/10.1016/j.nima.2006.05.156) (cit. on p. 134).
- [104] Claus Kleinwort. “General Broken Lines as Advanced Track Fitting Method”. In: *Nucl Instrum Meth* A673 (2012), pp. 107–110. DOI: [10.1016/j.nima.2012.01.024](https://doi.org/10.1016/j.nima.2012.01.024) (cit. on p. 134).
- [105] Virgil L. Highland. “Some Practical Remarks on Multiple Scattering”. In: *Nucl Instrum Meth* 129 (1975), p. 497. DOI: [10.1016/0029-554X\(75\)90743-0](https://doi.org/10.1016/0029-554X(75)90743-0) (cit. on p. 134).
- [106] John Alison. *The Road to Discovery: Detector Alignment, Electron Identification, Particle Misidentification, WW Physics, and the Discovery of the Higgs Boson: Doctoral Thesis Accepted by the University Of Pennsylvania, USA*. Springer theses : recognizing outstanding PH.D. research. Cham Heidelberg New York: Springer, 2015. 302 pp. ISBN: 978-3-319-10344-0 (cit. on pp. 136, 137).
- [107] V. Blobel. “Software Alignment for Tracking Detectors”. In: *Nucl Instrum Meth* A566 (2006), pp. 5–13. DOI: [10.1016/j.nima.2006.05.157](https://doi.org/10.1016/j.nima.2006.05.157) (cit. on p. 136).

Acronyms

- 2S Module** 2-Strip Module. 53
- Al-CF** Aluminum-Carbon Fiber. 54
- APD** Avalanche Photo Diode. 5
- APS** Acoustic Phonon Scattering. 34
- ATLAS** A Toroidal LHC ApparatuS. 1, 7, 9, 153
- CALDAC** Calibration DAC. 66
- CCE** charge collection efficiency. 12
- CERN** Conseil Européen pour la Recherche Nucléaire. 6
- CFRP** Carbon Fiber Reinforced Polymer. 54, 56
- CIC** Concentrator Integrated Circuit. 54, 62, 156
- CKM-Matrix** Cabibbo-Kobayashi-Maskawa Matrix. 1
- CML** Current Mode Logic. 59, 67
- CMS** Compact Muon Solenoid. 1, 2, 3, 4, 6, 7, 9, 11, 42, 153
- CMS Tracker Detector** CMS Tracker. 7, 146, 153
- CSA** Charge Sensitive Amplifier. 43, 55, 59, 60, 62
- DAC** Digital To Analog Converter. 61
- DAQ** Data Acquisition. 68, 130

-
- DM** Dark Matter. 9
- DUT** Device Under Test. 122, 123, 124, 125, 126, 132, 136, 138, 139, 141, 161
- ECAL** Electromagnetic Calorimeter. 5, 6
- EHP** Electron-Hole Pair. 15, 27, 35, 39, 41, 70, 73, 74, 108, 140, 154
- ENC** Equivalent Noise Charge. 59, 60, 61, 106, 147
- FE hybrid** Front-End hybrid. 55, 57, 55, 57, 156
- FPGA** Field Programmable Gate Array. 68, 125
- GBL** General Broken Lines. 127, 134, 135, 136, 138, 139, 151, 152
- GLIB** Gigabit Link Interface Board. 68, 116, 117, 125
- HCAL** Hadronic Calorimeter. 6
- HL-LHC** High-Luminosity LHC. 1, 2, 3, 5, 7, 8, 7, 9, 41, 42, 146, 150, 153
- HLT** High-Level Trigger. 6
- IIS** Ionized Impurity Scattering. 34
- Inverted MaPSA** Inverted MaPSA. 57, 122, 123, 161
- IT** Inner Tracker. 51
- L1** Level-1 Trigger. 6, 13, 51, 52, 62, 65, 67, 110, 156
- Laser** Light Amplification By Stimulated Emission Of Radiation. 23, 24
- LHC** Large Hadron Collider. 3, 6, 7, 10, 130, 146, 153
- LoG** Laplacian of Gaussian. 111, 160
- LS3** Long Shutdown 3. 7, 146, 153
- LSB** Least Significant Bit. 66, 111, 112, 118
- MAD** Median Absolute Deviation. 96, 151

-
- MaPSA** Macro-Pixel-Sub-Assembly Block. 54, 55, 67, 108, 121, 127, 130, 131, 132, 136, 139, 140, 139, 151, 156, 162
- MaPSA-Light** Macro-Pixel-Sub-Assembly block (light). 104, 106, 108, 110, 123, 128, 130, 136, 160, 161
- MCS** Multiple Coulomb Scattering. 4, 20, 57, 134, 139
- MIMOSA** Minimum Ionizing MOS Active pixel sensor. 122, 123, 124, 126, 161
- MIP** Minimum Ionizing Particle. 15, 16, 58, 108, 153
- MO** Metal Overhang. 84
- MOS** Metal Oxide Semiconductor. 81
- MPA** Macro Pixel ASIC. 54, 55, 56, 57, 55, 58, 61, 62, 63, 65, 66, 67, 68, 120, 125, 130, 141, 146, 155, 156, 161
- MPA-light** MPA-light. 65, 66, 67, 106, 119, 124, 125, 128, 129, 134, 138, 140
- MPV** Most Probable Value. 18, 153
- OT** Outer Tracker. 5, 13, 51, 53
- PDF** Probability Density Function. 18
- PS** Pixel Strip. 54, 55, 56, 63, 121, 146, 147, 155
- PS-s** PS strip. 53, 54, 57, 61, 147
- PS-p** PS pixel. 53, 54, 55, 56, 57, 61, 65, 94, 146, 147
- PS Module** Pixel-Strip Module. 53, 54, 61, 62, 155, 156
- PS-p light** PS-p light. 43, 65, 69, 140, 150, 154
- PTP** Punch-Through Protection. 43, 46, 47, 65, 72, 73, 74, 75, 76, 83, 84, 85, 86, 87, 88, 89, 90, 91, 93, 94, 95, 97, 98, 99, 100, 102, 113, 146, 154, 157, 158, 159

-
- RMS** Root Mean Square. 59, 126, 139, 152
- SM** standard model. 1, 9
- SMU** Source Measure Unit. 83, 99, 126
- SRAM** Static Random-Access Memory. 65, 110
- SRH** Shockley-Read-Hall. 22, 71, 78
- SSA** Short Strip ASIC. 54, 61, 62, 64
- SUSY** Supersymmetry. 9
- TCAD** Technology Computer Aided Design. 2, 84
- THDAC** Threshold DAC. 62, 66, 105, 106, 109, 111, 117, 118, 130, 139, 141, 140, 162
- TLU** Trigger/Timing Logic Unit. 124, 125, 162
- TRIMDAC** Trimming DAC. 62, 66, 105, 106, 112, 160
- VPT** Vacuum Photo Triodes. 5